2009

Multi-functional composite materials for catalysis and chemical mechanical planarization

Cecil A. Coutinho
University of South Florida

Multi-Functional Composite Materials for Catalysis and Chemical Mechanical Planarization

by

Cecil A. Coutinho

A dissertation submitted in partial fulfillment
of the requirements for the degree of
Doctor of Philosophy
Department of Chemical and Biomedical Engineering
College of Engineering
University of South Florida

Major Professor: Vinay Gupta, Ph.D.
Norma Alcantar, Ph.D.
John Wolan, Ph.D.
Maya Trotz, Ph.D.
Hariharan Srikanth, Ph.D.

Date of Approval:
February 23, 2009

Keywords: Titania, composites, ceria, PNIPAM, chemical mechanical polishing, remediation, microgels, planarization, slurry, methyl orange, photocatalytic degradation, sedimentation, turbidometry, CMP, Degussa P25, free radical polymerization

DEDICATION

This dissertation is dedicated to my family, especially…

My parents, Agnel and Irene Coutinho, for infusing in me the importance of hard work

My sister, Savia Coutinho, for always being my role model and confidant

It is through your words of encouragement and push for tenacity that I have completed this work. Thank you for all of your love, support and sacrifice throughout my life.

This dissertation is dedicated to you. I could have not done it without you.

With Love,

Cecil

ACKNOWLEDGEMENTS

I would like to thank my research advisor Professor Gupta, for his guidance and creative insights during the course of this work. My learning experience with him has been very prolific and enabled me to grow as an engineer and as a researcher. I will always appreciate the time he took to train me and to enhance my knowledge on a wide array of topics vital to the success of my graduate studies. I need to extend a heartfelt thanks to my family and friends for their tremendous support throughout the years. Their unwavering love and confidence in me, have helped me through every hardship. This dissertation would not be possible without the intellectual support of my committee members: Dr. John Wolan, Dr. Norma Alcantar, Dr. Maya Trotz and Dr. Hariharan Srikanth. I am also grateful for the useful insights that came through discussions with classmates Raghu Mudhivarthi, David Walker, Bijith Mankidy, Jonathan Mbah, Chhavi Manocha, Dayling Chapparo and Mark Sugimoto all of whom I now consider close friends. A special thanks to the members of the Interfacial Phenomena and Polymeric Materials labgroup (Dr. Shim, Kristina Tran, Alicia Peterson, Adrian Defante, Justine Molas, Fedena Fanord, Claire Osborn, Violetta Yevstigneyeva) all of whom have become a second family. Finally, I would like to thank Betty Loraamm for TEM training and endless assistance with microscopy during the course of these projects. This research was conducted with the financial support of the National Science Foundation and the Department of Chemical & Biomedical Engineering at the University of South Florida.

TABLE OF CONTENTS

LIST OF TABLES

LIST OF FIGURES

Multi-Functional Composite Materials for Catalysis and Chemical Mechanical Planarization

Cecil A. Coutinho

ABSTRACT

Composite materials formed from two or more functionally different materials offer a versatile avenue to create a tailored material with well defined traits. Within this dissertation research, multi-functional composites were synthesized based on organic and inorganic materials. The functionally of these composites was experimentally tested and a semi-empirical model describing the sedimentation behavior of these particles was developed.

This first objective involved the fabrication of microcomposites consisting of titanium dioxide (TiO_2) nanoparticles confined within porous, microgels of a thermo-responsive polymer for use in the photocatalytic treatment of wastewater. TiO_2 has been shown to be an excellent photocatalyst with potential applications in advanced oxidative processes such as wastewater remediation. Upon UV irradiation, short-lived electron-hole pairs are generated, which produce oxidative species that degrade simple organic

contaminants. The rapid sedimentation of these microcomposites provided an easy gravimetric separation after remediation. Methyl orange was used as a model organic contaminant to investigate the kinetics of photodegradation under a range of concentrations and pH conditions. Although after prolonged periods of UV irradiation (~8-13 hrs), the titania-microgels also degrade, regeneration of the microcomposites was straightforward via the addition of polymer microgels with no loss in photocatalytic activity of the reformed microcomposites.

The second objective within this dissertation involved the systematic development of abrasive microcomposite particles containing well dispersed nanoparticles of ceria in an organic/inorganic hybrid polymeric particle for use in chemical mechanical polishing/planarization (CMP). A challenge in IC fabrication involves the defect-free planarization of silicon oxide films for successful multi-layer deposition. Planarization studies conducted with the microcomposites prepared in this research, yield very smooth, planar surfaces with removal rates that rival those of inorganic oxides slurries typically used in industry. The density and size of these ceria-microgel particles could be controlled by varying the temperature or composition during synthesis, leading to softer or harder polishing when desired.

CHAPTER 1: INTRODUCTION

1.1. Introduction to Composite Materials

Composite materials (or composites for short) are broadly classified as those materials that consist of two or more constituent materials with different physical and chemical characteristics[1]. Generally, these characteristics remain separate and distinct within the resulting composite while yielding enhanced properties when compared with the individual components. Composites can be synthetic or natural. For example wood is a well known (natural) composite of cellulose fibers that are bound together by lignin[2]. Concrete is another well known (synthetic) composite material. It consists of aggregates (limestone or gravel) that are bound together via a cement matrix that forms chemical bonds with itself and the aggregates upon hydration[3]. In fact, the most primitive composite materials were bricks used for building construction that were comprised of straw and mud[4].

Typically, composite materials consist of two categories of constituent materials: a matrix and reinforcement. The primary function of the matrix is to encompass and support the reinforcement materials. The reinforcement materials in turn impart superior mechanical and physical properties to the entire composite material[3]. Hence by careful selection of the matrix, the reinforcement materials and their respective ratios within the final structure, composite materials can be easily engineered to possess certain desirable

properties. Nowadays, many commercially produced composite materials contain a polymer matrix that is frequently known as a resin solution. Polymers are widely used as they are inexpensive, easily available and a wide variety of structurally different resins are available. Typical resins include polyesters, epoxies, and polyamides, amongst others. The reinforcement materials are often fibers but also many mineral oxides are frequently used. The strength of the product is greatly dependent on the resin to reinforcement material ratio[3]. Over recent decades many new composites have been developed, some with very valuable properties. By carefully choosing the reinforcement material, matrix, and the manufacturing process that brings both of them together, composite materials can be easily tailored to meet specific requirements.

1.2. Motivation of Research Projects

In this research, the synthesis of composite materials was pursued with the broad aim of combining the physical and chemical properties of inorganic oxides and organic materials within a final structure. Furthermore, when the composite brings together constituent materials at different length-scales (nanometer and micrometer), the ability to tailor the functional properties of materials becomes even more powerful. The study of these new materials has generated intense interdisciplinary efforts in engineering and the physical sciences because applications of these composite materials range from sensing[5] and drug delivery[6] to wastewater remediation[7].

A variety of novel systems will be explored within this dissertation, and all entail the coupling of two or more functionally different materials to yield a new composite that has different physical attributes from the individual components. Cross-linked,

microspherical particles or “microgels” of stimuli responsive polymers are of particular interest. When coupled with co-polymers containing inorganic segments, or loaded with nanoparticles of inorganic oxides, interesting new materials arise. In this dissertation, a hybrid particle is defined as a microgel consisting of an organic polymeric network chemically bonded to an inorganic or a metallic component. Similarly, a microcomposite particle is a microgel (hybrid or nonhybrid) that contains nanoparticles of an inorganic oxide embedded within the polymer matrix via a physical entrapment and electrostatic interactions, not a covalent bond.

Figure 1.1A illustrates a titania-microgel microcomposite, where titanium dioxide nanoparticles are confined within a responsive microgel network of a polymer for photocatalytic applications in wastewater remediation. Figure 1.1B shows a schematic of a hybrid particle, where condensed silica (originating from a siloxane co-polymer) co-exist with the organic polymeric microgel, to create a micron-sized hybrid particle used in chemical mechanical polishing (CMP). Lastly, figure 1.1C shows a microcomposite particle of a hybrid microgel with nanoparticles of ceria embedded within the matrix of a hybrid microgel. This permits the tailoring of the hardness and softness of the microcomposite particle (termed siloxane-ceria-microgel) for CMP processes.

The main goal of this research project is, therefore, to establish the principles for the design of novel microcomposites by combination of different materials that possess unique optical, electronic, and mechanical attributes and to demonstrate the use of these new materials in technological applications.

1.2.1. Microcomposite Particles Used for Photocatalysis

Titanium dioxide is a common and widely studied photocatalyst due to its appealing attributes such as non-toxicity, chemical inertness and high photocatalytic activity[8-10]. Since the first report[11] of photocatalytic purification of water using titania in 1977, use of TiO_2 has been widely investigated in literature[12-14]. The large band gap of TiO_2 (~3.2eV) permits it to absorb photons in the UV region, which results in the production of electron-hole pairs that migrate to the catalyst surface and participate in redox reactions with organic species[15] as shown in figure 1.2. Upon doping with nitrogen or metal ions, TiO_2 shows photocatalytic activity under visible radiation, which can potentially increase its commercial viability enormously[16, 17].

In recent years, there has been increased interest in the use of nanosized titania powders due to enhancements in photocatalytic activity. This enhancement results from changes in properties such as crystallinity, surface area for reaction, and density of surface groups like OH that accompany the fine size[18-20]. Because separation of suspended fine particles from water has been a major obstacle, use of nanoparticles of titania in applications such as wastewater treatment has been limited. Strategies that have been investigated to address this obstacle include immobilization of titania particles onto planar substrates or reactor walls[18-20]. However, the reduction in available surface area of the catalyst and the transport limitations to the surface can lead to diminished photocatalytic activity, thereby limiting the usefulness of these strategies.

Much attention has been given to the fabrication of polymer-inorganic microcomposites as a means of overcoming the ensuing aggregation and separation difficulties that have been frequently encountered. Towards this end, a few researchers

have explored using supercritical fluids as a means to incorporate insoluble inorganic nanoparticles into the organic network[21, 22]. One drawback of this approach is that the nanoparticles often aggregate within the polymer thereby reducing the effective surface area[23]. Other approaches have involved using polymer synthesized by emulsion polymerization to encapsulate inorganic or metallic nanoparticles[23]. However the organic-aqueous interface required for polymerization frequently requires toxic organic solvents, surfactants, and stabilizers that can be difficult to remove and can create environmental problems. Therefore, approaches that do not require organic solvents or stabilizers and that are easy to load with nanoparticles in polymers to create microcomposites can be quite useful.

Our goal is to explore an alternative approach that involves using responsive polymer microgels to entrap the TiO_2 nanoparticles. In recent years the fabrication of stimuli responsive polymeric microgels has generated much interest due to its ease of synthesis in aqueous media and their technological application. Stimuli responsive microgels can respond in shape and size to external stimuli like temperature, pH, ionic strength etc. The porosity of the gel facilitates the loading of the polymer network with titania while still exploiting the large available surface area of the TiO_2 nanoparticles and maintaining the transparency of the solution for photocatalysis. The microcomposite has a sufficiently high density that it can be separated from solutions by a simple gravity settling technique.

In this doctoral research, commercially available Degussa^{TM} P25 TiO_2 nanoparticles entrapped within the polymer microgels were used for photocatalytic experiments for reasons such as easy availability, known remediation properties, and

known crystalline structure[24, 25]. The synthesis, characterization, and photocatalytic performance of these microcomposites has been investigated. The results reported here are critical and necessary inputs in the development of processes that can use the novel titania-microgel microcomposites in photodegradation of chemical contaminants in aqueous streams.

1.2.2. Microcomposite and Hybrid Particles Used for CMP

A fundamental process during integrated circuit manufacturing is the planarization of the wafer before any patterning or deposition on that wafer surface. To produce multilevel metal interconnects the wafer surface needs to be optically smooth, devoid of pits, scratches or organic depositions. However, as device dimensions approach micrometer and ultimately nanometer sizes, the challenge arises to conduct photolithography and successfully manufacture multilevel metal interconnects. To produce a working device nowadays, the topmost layer of the previous metallization level has to be microscopically smooth with minimal surface roughness. Any residual roughness that exists at the previous layer will eventually get compounded as the layers increase. First developed by IBM in 1983, chemical mechanical polishing/planarization has emerged as the method of choice amongst planarization techniques. This is due to its ability to achieve excellent local and global planarization across the wafer surface in relatively short time-scales coupled with the relatively low cost of the CMP process. It has been shown that it is not possible to proceed with further processing steps until a smooth wafer surface is first achieved. Uneven wafer surfaces will often lead to errors during photolithography and several other processing challenges such as voids within

interconnects and compounded roughness tends to arise. Thus, CMP becomes a crucial processing step in device fabrication[26]. To achieve a planar wafer, two types of CMP processes can be conducted: (i) conventional CMP that consists of abrasive particles dispersed in aqueous slurry and (ii) fixed abrasive CMP where the abrasive particles are firmly lodged in a polymer polishing pad against which the wafer rubs in a process likened to sandblasting a rough surface. The work presented here has focused upon conventional CMP for reasons explained in chapter 6 of the text.

Within a CMP process, the chemical and mechanical interactions act in synergy between the wafer material, slurry particles and polishing pad to planarize the wafer surface[27]. Abrasive particles in the slurry achieve the mechanical action needed for polishing but the performance of these abrasive particles depends on variables such as particle type, size and concentration[27, 28]. Colloidal nanoparticles of SiO_2, CeO_2 or Al_2O_3 are typically the abrasive particles used to polish silicon oxide wafers industrially. The slurry achieves chemical isotropic etching of the silicon oxide surface by typically using hydroxides of alkali metals. The high pH chemical etching is necessary to enhance the mechanical abrasion of the slurry. The mechanical polishing preferentially grinds the material at high points on the surface thereby producing a planar wafer as can be seen in figure 1.4. Thus, both chemical and mechanical actions are needed for the global planarization of the wafer surface. However, the abrasive particles produce defects such as scratching, irregular polishing and particle deposition on the wafer surface[29]. All these defects produce local roughness that blocks lithography and the subsequent addition of metal layers for integrated circuit manufacturing.

To remedy some of these drawbacks, the synthesis of slurries comprising of abrasive particles containing either hybrid microgels or (siloxane-ceria-microgel) microcomposites were pursued in this doctoral research. The synthesis, characterization and performance of a variety of abrasive particles used for planarization studies will be detailed within this dissertation. Some of these particles include: (A) hybrid microgel (B) hybrid nanogel (C) a core-shell abrasive particle of micron dimensions with a silica core and a shell consisting of a responsive polymer, and lastly (D) a (siloxane-ceria-microgel) microcomposite that contains ceria nanoparticles embedded within a hybrid microgel. Ultimately, the goal is to tailor the abrasive action of the particles to influence the etch rate of the oxide surface and reduce the local roughness thereby creating a smoother wafer.

1.3. Dissertation Description

This dissertation outlines the synthesis, characterization and technological applications that are represented by novel microcomposites of inorganic oxide nanoparticles encased within polymer microgels. Successful accomplishment of two main goals is detailed: (A) fabrication of photocatalytic microcomposite particles for wastewater remediation, and (B) development of abrasive particles on micron/nanometer length-scales for the chemical mechanical planarization of silicon oxide wafers for IC manufacturing.

This dissertation is organized as follows. Chapter 2 will discuss the various synthesis strategies that were employed for the polymerization of PNIPAM microgels/nanogels as well as microgels/nanogels based on copolymers and

interpenetrating networks. All of the polymerization was done in aqueous media using free radical polymerization techniques. Here, the hydrophilic-hydrophobic interactions responsible for phase transition behavior of the polymer particles are also discussed. Several underlying themes that interconnect the above stated objectives of this dissertation will become evident as many of the formulations used in this research were similar, where slight modifications resulted in functionally and structurally different particles.

In chapter 3, the extensively characterization techniques that have been employed in this work will be presented. This includes but is not limited to spectroscopic characterization such as Fourier transform infrared spectroscopy (FTIR) that was used to ascertain the increase in siloxane in the polymer hybrid microgels. Also ultraviolet-visible light (UV-Vis) spectroscopy was used extensively in photocatalytic studies and to determine the amount of titania within the microcomposites. Multi-angle monochromatic ellipsometry was used to determine the thickness of oxide films before and after planarization. Microscopy was employed extensively in this research via atomic force microscopy (AFM) to examine the planarity of oxide wafer surfaces after polishing and transmission electron microscopy (TEM) to visualize the extent of inorganic oxide dispersion within the polymer microspheres. Light scattering techniques such as dynamic light scattering (DLS) were also utilized to describe the responsive nature of the polymer microgels in solution. Additionally, sedimentation studies of the microcomposite particles were conducted via turbidity measurements. Other characterization techniques such as thermal gravimetric analysis (TGA) and total nitrogen/total organic carbon (TN/TOC) analysis will be presented in this chapter.

The settling behavior of titania-microgel microcomposite particles is presented in chapter 4. The microcomposites showed rapid sedimentation (~minutes) that was ~100 times faster than the titania nanoparticles alone. This sedimentation behavior was captured by monitoring the decline in the turbidity of the solution. The settling microcomposite particles traveled through a pre-determined scattering zone from which the mean count rate of the scattered light was translated into a normalized turbidity signal. A semi-empirical model was developed and used to characterize the loading of the titania within the microcomposite particle. It was shown that as the content of TiO_2 increased within the particles from 10% to 75%, a large enhancement in the settling velocities of the microcomposites was observed experimentally.

In chapter 5, the titania-microgel microcomposites were employed to examine the photodegradation of an organic dye. Degradation kinetics of the rapidly sedimenting microcomposites were compared against freely suspended titania nanoparticles at a variety of photocatalyst concentrations and solution pH conditions. Both were shown to follow pseudo first order reaction kinetics, although the rate constants of the microcomposite particles can be easily tuned. The eventual degradation of the microcomposite particles under UV-illumination will be presented, in addition to other techniques used to monitor the degradation of the titania-microgel microcomposite particles with time.

Chapter 6 presents the development of slurries containing novel hybrid microgel particles and siloxane-ceria-microgel microcomposites that are less abrasive as compared to conventional ceramic particles used in silicon oxide CMP. The goal here was to obtain improved surface finish on the wafer surface without compromising oxide removal rates.

This is of significance to the current stringent polishing requirements required during IC fabrication. In this context, hybrid and microcomposite particles based on polymer-inorganic oxide materials have shown to be promising for next generation slurries. A number of slurries will be briefly discussed, but this dissertation will focus on two slurries in particular due to their ease of synthesis and superior performance during planarization. The first slurry consisted of hybrid microgels particles that resulted in very planar surfaces but minimal oxide removal. The second slurry comprised of siloxane-ceria-microgels for improved oxide removal and smooth wafer surfaces. Extensive microscopy characterization depicts the smoothness of these surfaces, while spectroscopic measurements confirm similar removal rates of the microcomposite slurries versus slurries comprising of only inorganic oxide nanoparticles.

Chapter 7 will provide an overall summary of the research performed in this dissertation and outline future steps that can build upon the new materials synthesized to make them more robust and versatile.

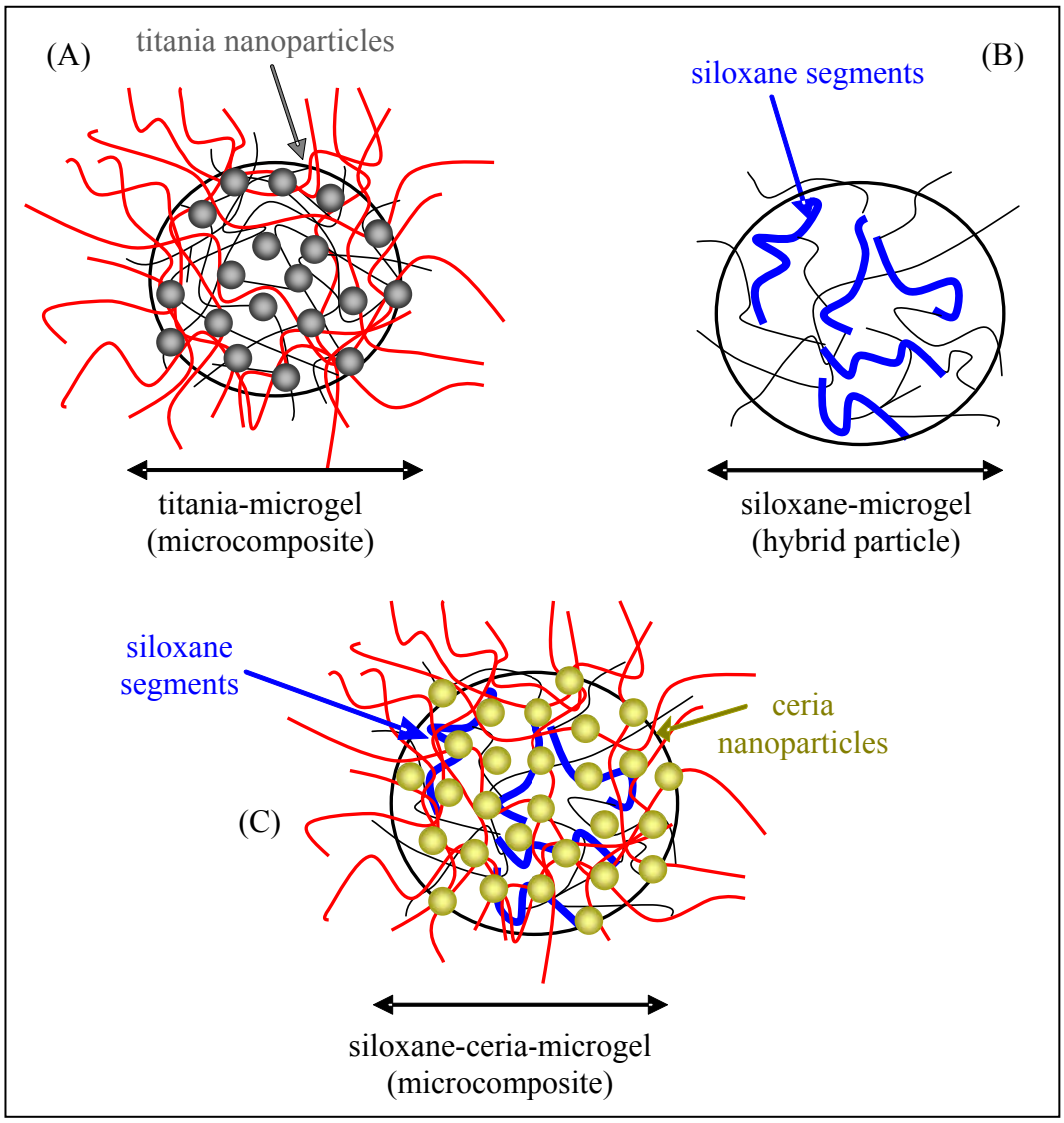

Figure 1.1: Schematic of the proposed microcomposite and hybrid materials.

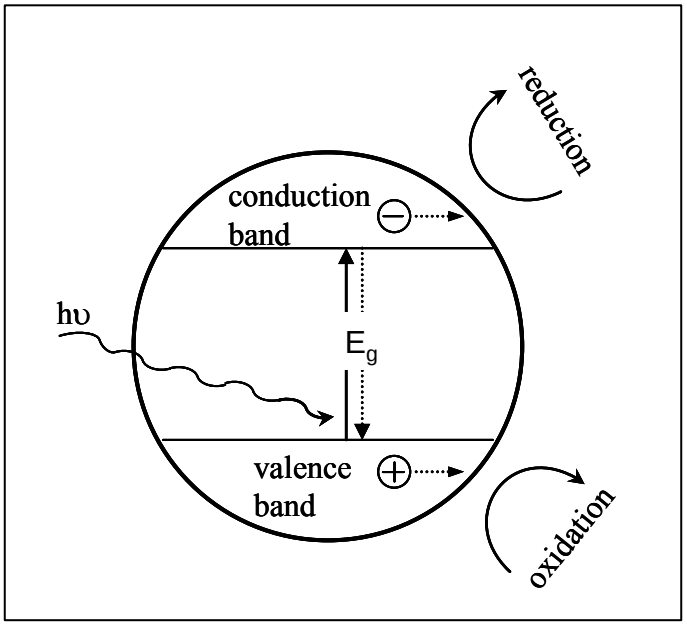

Figure 1.2: UV illumination resulting in electron-hole pairs at the TiO_2 surface causing redox reactions.

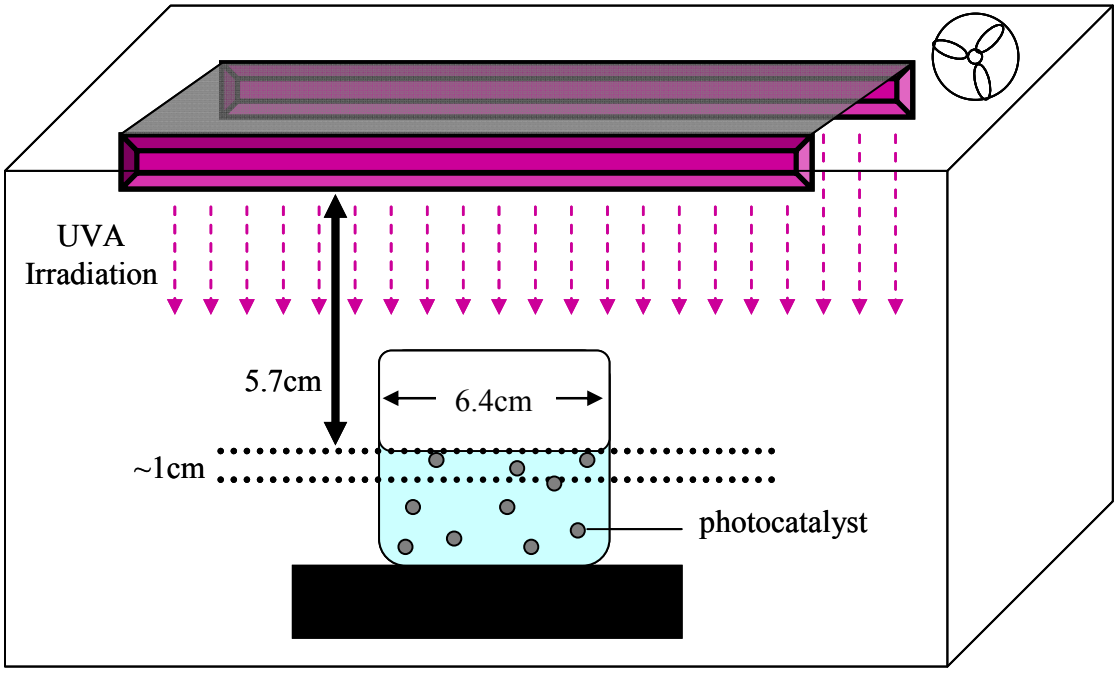

Figure 1.3: Schematic of setup for photocatalytic study.

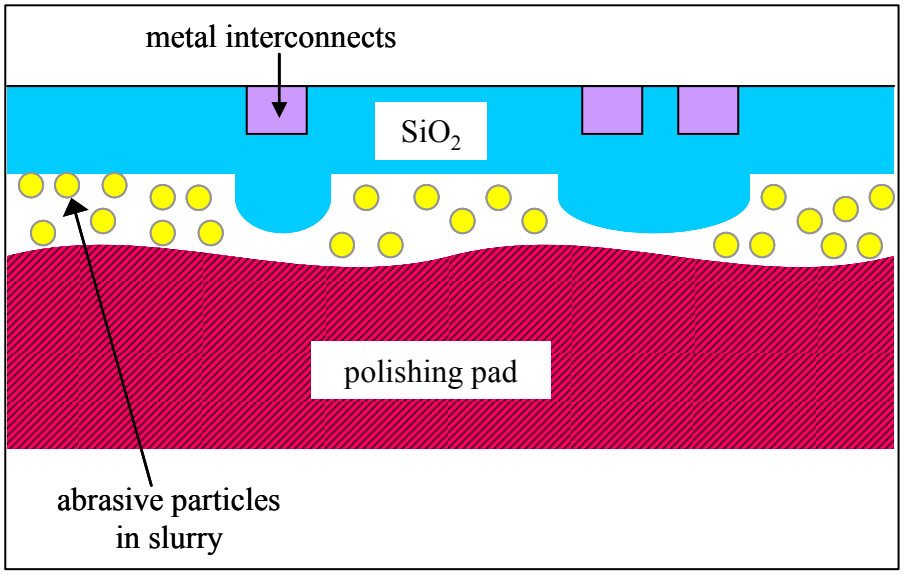

Figure 1.4: Pad-wafer interface, showing high points on silica wafer being reduced during the CMP process.

CHAPTER 2: SYNTHESIS OF NOVEL POLYMER BASED PARTICLES

2.1. Thermally Responsive Polymers and Their Networks

Stimuli sensitive polymers are known to respond to changes in the external environment such as temperature, ionic strength, solvent concentration and pH. These polymers have been extensively studied for the past two decades[30-33] and have found many interesting technological applications[34-38]. Modifying the properties of these 'smart' materials, has led to enhancements in a number of areas such as drug delivery[39] and sensors[33]. One of the current challenges lies in understanding the mechanisms that govern this stimuli responsive transition behavior and fabricate new novel materials that can exploit the "smart" feature of these materials.

Since the first synthesis in 1986[40] by Pelton, microgels of poly(N-isopropylacrylamide) (PNIPAM) have become the most widely studied temperature sensitive responsive polymer particles[32, 40]. PNIPAM is a nonionic polymer that is usually prepared by free radical precipitation polymerization in aqueous media[41-43]. Linear chains of PNIPAM have been shown to displays a reversible and continuous volume phase transition behavior at 32°C. Below this critical temperature PNIPAM is hydrophilic and exists as a coiled polymer chain. Above this critical temperature it becomes hydrophobic and transitions to form a denser globular structure. It has been hypothesized that the polymer chain folds in on itself and releases hydrogen bonded water molecules[44] with the

exact mechanism of this collapse still under investigation[45]. The lower critical solution temperature (LCST) exits due to a balance between the hydrophobic carbon backbone and isopropyl side chain, with the hydrophilic amide side chain. Increasing the temperature past the LCST has an interesting effect. It disrupts the hydrogen bonding between the amide side chains and the water molecules. As a result, this causes a decrease in the entropy of the system due to the reduction in the degrees of freedom of the swollen polymer chains. Dissolution of the polymer chains is now thermodynamically unfavorable due to the increase of the Gibbs free energy of the system[44].

Microgels of PNIPAM are typically synthesized using a divinyl cross-linker and a free radical initiator to co-polymerize the polymer chains into a polymer chain network. Figure 2.1 displays a schematic of these spherical microgels that have a hydrodynamic radius around ~0.8μm when swollen and ~0.4μm when shrunk (sizes determined by DLS and TEM imaging). These microgels can be easily dispersed in aqueous environments to form transparent solutions when the solution temperature is below the LCST and turbid solutions when the solution temperature is above the LCST. The time taken for these microgels to collapse or swell with changes in temperature is in the order of a few minutes. Tanaka and co-workers have shown that the time taken for the gels to shrink/swell is directly proportional to the square of the radius of gyration of the microgel[46]. Hence gels on micron length-scales have very quick responses and this quick, thermal responsive capability of microgels of PNIPAM makes it suitable for a variety of applications ranging from drug delivery to catalysis.

2.2. Experimental Details and Material Synthesis

All chemicals were purchased from Sigma-Aldrich and used without further purification, unless otherwise noted. The monomer NIPAM (TCI, Japan) was recrystallized from hexane once before use. Water utilized in all microcomposite synthesis was purified using an EasyPure UV system (Barnstead, IA). A 0.2μm filter in this system was used to remove particulate matter.

2.2.1. Synthesis of Polymer Particles

- *PNIPAM microgel synthesis*. A typical schematic of the reaction procedure is shown in figure 2.2A. As a first step, NIPAM (~1.0g) was recrystallized from hexane and dried under vacuum prior to use to remove impurities and inhibitors. The PNIPAM microgels were synthesized via surfactant free precipitation polymerization[41, 42, 47]. Polymerization was carried out in a sealed round-bottom flask equipped with a magnetic stirrer and an oil bath to control the reaction temperature. Free radical polymerization of NIPAM using N,N'-methylenebisacrylamide (MBAA) (~0.04g) as a cross-linker was initiated using potassium persulfate (KPS) (~0.02g) in an aqueous medium at 75°C. The solution was purged with nitrogen gas for ~45min before polymerization. After polymerization for 5hr, the final product was centrifuged at 7500rpm. The supernatant (that contained some unused reagents and oligomers) was removed and replaced with fresh deionized water. The microgels were then re-dispersed via sonication and vortex mixing and later re-centrifuged. This washing procedure was repeated three times to try and ensure as pure a product of PNIPAM microgels as possible for subsequent characterization.

- *PNIPAM nanogel synthesis*. NIPAM (~1.0g) and MBAA (~0.04g) were dissolved in aqueous solution containing Sodium dodecylsulfate (SDS) (Merck; ~0.13g) using a recipe established by Andersson and co-workers[48] (figure 2.2B) . The solution (70mL) was purged with nitrogen and stirred at room temperature for 45min. The nitrogen inlet and outlet were removed and the flask was placed into a preheated oil bath at 75°C. Polymerization was initiated by injecting KPS (~0.02g) to the reaction mixture (dissolved in 2mL of water). The reaction was allowed to proceed for 5hr under vigorous agitation using a magnetic stirrer. The polymerization was stopped by the addition of 20mL of room temperature deionized water (to introduce dissolved oxygen that acts as a free radical scavenger) and cooling the product to room temperature. Snakeskin® pleated dialysis tubing with nominal molecular weight cut off 10000g/mol were used as membranes in nanogel purification. All polymer nanogels synthesized were purified by dialysis for 7days against distilled water that was refreshed daily (twice daily during the first 3days).

- *Peripheral penetrating (PP) microgel synthesis*. The PNIPAM microgels (~1.0g) formed above were mixed with Acrylic Acid (~1.0g) and dispersed in deionized water at 0ºC as shown in figure 2.3A. The incorporation of the peripheral penetrating chains of acrylic acid in the microgels was performed by adapting a procedure previously reported by Xia and Hu[49]. The solution was bubbled with (industrial grade) nitrogen gas for ~45min, to displace dissolved oxygen[50]. The initiator potassium persulfate (0.04g) and the accelerator N,N,N′,N′-tetramethylethylenediamine (TEMED) (0.1mL) was added and the reaction allowed to proceed for 5hr in an ice bath. The product was centrifuged

(7500rpm), the supernatant decanted and the PP-microgels (figure 2.3A) re-dispersed in fresh DI water followed by sonication and vortex mixing for ~1h each. This washing procedure was repeated three times to ensure a homogeneous pure product that was later characterized.

- *Interpenetrating (IP) microgel synthesis*. Interpenetrating microgels were formed by the surfactant free precipitation polymerization of NIPAM (~1.0g) in an aqueous solution (~200mL) containing polyacrylic acid sodium salt[35] (~1.5g, M_W 15000g/mol) as shown in figure 2.3B. The PNIPAM microgel was cross-linked using MBAA (~0.04g) while KPS (~0.02g) served as the ionic free radical initiator. The solution was purged with nitrogen gas for 45min before polymerization, the reaction mixture placed in an oil bath at 75°C and the initiator added. After polymerization for 5hr, the final product was centrifuged at 7500rpm, re-dispersed, and sonicated for 1hr. This washing process was also repeated three times.

2.2.2. Hybrid Particle Synthesis

- *Siloxane-microgel hybrid particle*. Recrystallized NIPAM (~5.0g) was dissolved in 800mL of deionized water and MBAA (~0.2g) was added (figure 2.4A). The solution was bubbled with nitrogen gas for 45min at room temperature, the reaction flask heated to 75°C and ~0.1g of KPS was added to initiate the reaction. Two hours later 1.0mL of MPS was added and polymerization was allowed to continue for another 1hr 45min. The product was centrifuged at 7500rpm and washed with deionized water three times in a similar cleaning procedure outlined above.

Core(silica)-shell(polymer) particles were prepared using a similar procedure. When the reaction was allowed to continue for 12hr (rather than 1hr 45min) after the addition of MPS, then the particle morphology changed from a hybrid particle to a core-shell particle (figure 2.4B). This product was cleaned in a similar fashion to the siloxane-microgel hybrid particles.

- *Siloxane-nanogel hybrid particle*. Recrystallized NIPAM (~5.0g) was dissolved in 340mL of deionized water to which ~0.3g of MBAA and ~0.64g of SDS was added. The typical reagents and resulting particle morphology are shown in figure 2.4C. The solution was slowly bubbled with N_2 gas for 45min at room temperature. The reaction flask was heated to 75°C and 0.2g of KPS (dissolved in deionized water) was added to initiate the reaction. Two hours later 1.0mL of MPS was added and polymerization was allowed to continue for another 1hr 45min, after which ~50mL of deionized water at room temperature was added to stop the polymerization. The product was cooled to room temperature and used without any purification for planarization studies.

- *Siloxane-microgel IP-hybrid particle*. Microgels were formed by the surfactant free precipitation polymerization of NIPAM (~5.0g) in aqueous media (800mL) using MBAA (0.2g)[36, 51, 52]. Interpenetrating chains of poly(acrylic acid) (PAAc) were introduced to form IP-hybrid microgels by adding the sodium salt of PAAc (~10g, M_W ~15000g/mol) in the initial reaction mixture (figure 2.5). Following purging with N_2 for 45min, the reaction mixture was heated in an oil bath to 75°C and KPS (0.1g) added to initiate polymerization. MPS was added as the co-monomer to the reaction mixture 2hr past

initiation to introduce siloxane functional groups and the polymerization was continued for another 1hr 45min. The particles were purified by centrifugation (7500rpm, 30min) and re-dispersed (via sonication and vortex mixing) in fresh deionized water. The washing procedure was conducted three times.

2.2.3. Microcomposite Particle Synthesis

- *Titania-PP-microgel microcomposite synthesis*. Nanoparticles of TiO_2 powder (Degussa^{TM} P25 grade or synthesized nanoparticles of TiO_2) were suspended in deionized water and the suspension adjusted to pH 2 using HCl. The TiO_2 solution was centrifuged (8500rpm, 30min) to remove aggregates and the resulting monodisperse suspension was used for microcomposite formation. The PP-microgel solution was mixed with the TiO_2 suspension and stirred for 1 hr. The resulting microcomposite that formed (a fluffy white solid) was collected by centrifugation (8500 rpm, 30min). These microcomposites were subsequently re-dispersed in fresh DI water and the pH of the solution adjusted to neutral conditions. Ultrafine TiO_2 was synthesized using a sol-gel technique where titanium tetraisopropoxide (3mL) together with 37% v/v HCL(0.5mL) were added to 200mL of absolute ethanol at 0°C[22]. The resulting suspension was peptized by stirring for an additional 4 hr. The solvent was removed with a rotary evaporator and the resulting nanoparticles of TiO_2 were re-suspended in deionized water.

- *Titania-microgel microcomposite synthesis*. A diagrammatic representation of the titania-microgel microcomposite synthesis is shown in figure 2.6A. A monodisperse suspension of TiO_2 (Degussa^{TM} P25 grade or synthesized nanoparticles of TiO_2) was

mixed with the IP-microgels under vigorous stirring at a pH~2. Titania-microgel composite particles formed instantaneously and using sodium hydroxide, the pH of the resulting mixture was raised to ~6. These microcomposite particles were optimum for photocatalysis (see chapter 3) and will be referred to as titania-microgel microcomposites (rather than titania-IP-microgel microcomposites). After formation of the microcomposites and pH adjustment, the composite particles were allowed to sediment and the supernatant was removed. This washing process was repeated three times.

- *Siloxane-ceria-microgel microcomposite*. Nanoparticles of CeO_2 were suspended in deionized water and sonicated for 2 hr to obtain a homogeneous suspension. This CeO_2 solution was then mixed with the siloxane-microgel hybrid particles in a desired loading ratio at a pH ~2. The resulting microcomposite settled to the bottom and the supernatant removed. The microcomposite solution was washed three times with deionized water and the pH adjusted to a value of 5 for subsequent polishing studies.

2.3. Summary

In summary, several polymer, hybrid and organic-inorganic microcomposite particles were prepared. These include PNIPAM microgels/nanogels (polymer-only particles), siloxane-microgel/nanogel (hybrid particles), core-shell (hybrid particles) and inorganic-organic microcomposite particles containing either titania or ceria dispersed within the polymer matrix. Microgels of PNIPAM containing interpenetrating or peripherally penetrating linear chains of PAAc were also prepared that were used for microcomposite fabrication. The PAAc helped to stabilize CeO_2/TiO_2 nanoparticles

within the microgels. The approach of making microcomposites using interpenetrating PAAc described here is simple and the loading of CeO_2/TiO_2 within the colloidal particles was easily manipulated by controlling the mixing ratios of the polymer and inorganic oxide solutions.

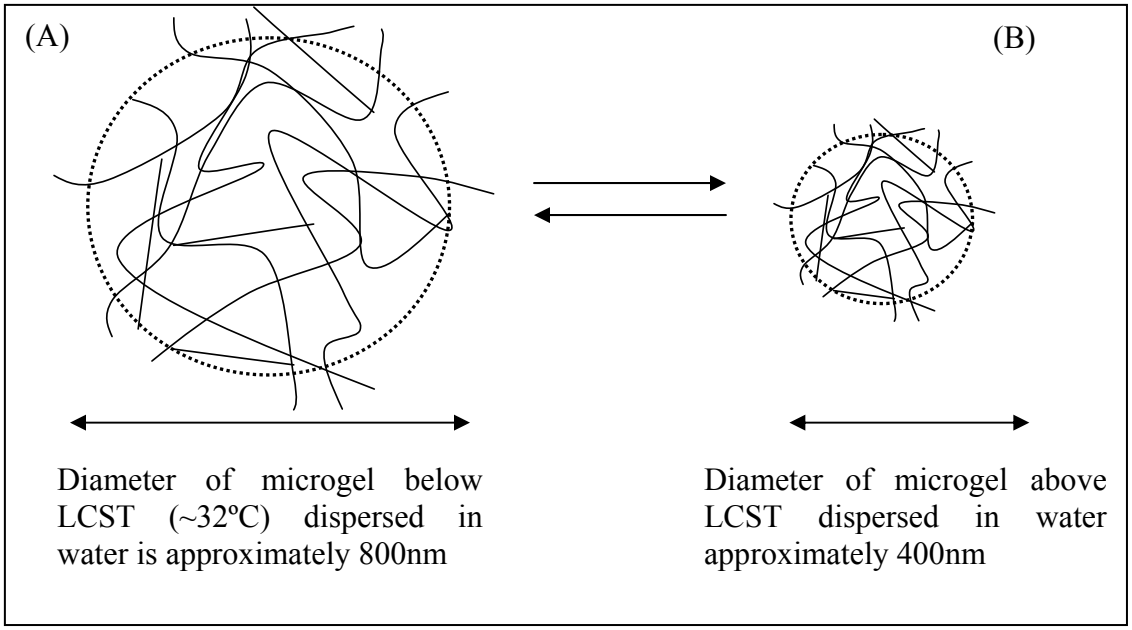

Figure 2.1: Schematic of (A) swollen PNIPAM microgel particle at below LCST and (B) collapsed microgel particles above the LCST dispersed in water.

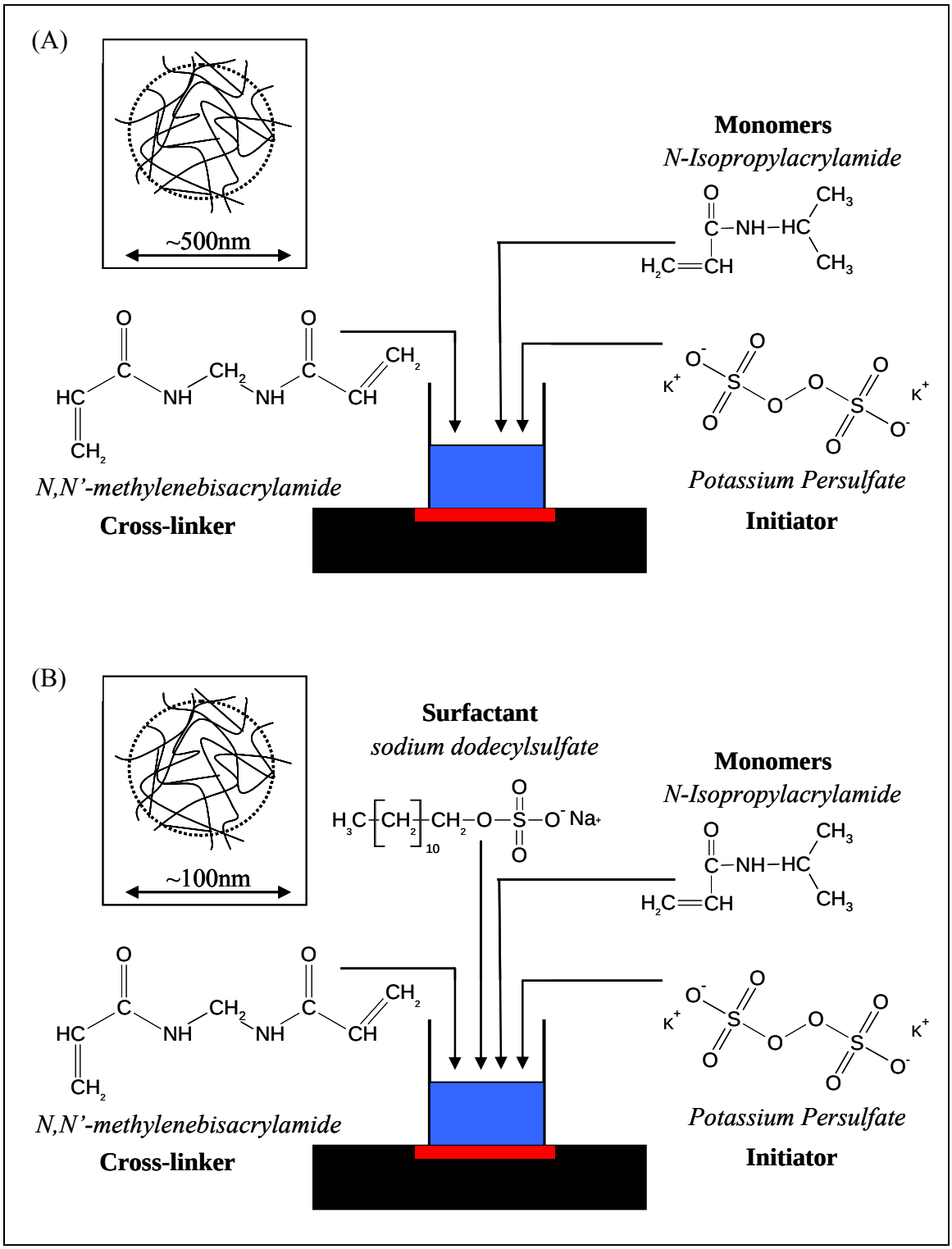

Figure 2.2: Synthesis setup for (A) PNIPAM microgels and (B) PNIPAM nanogels. In both images, the insets show a sketch of a representative particle.

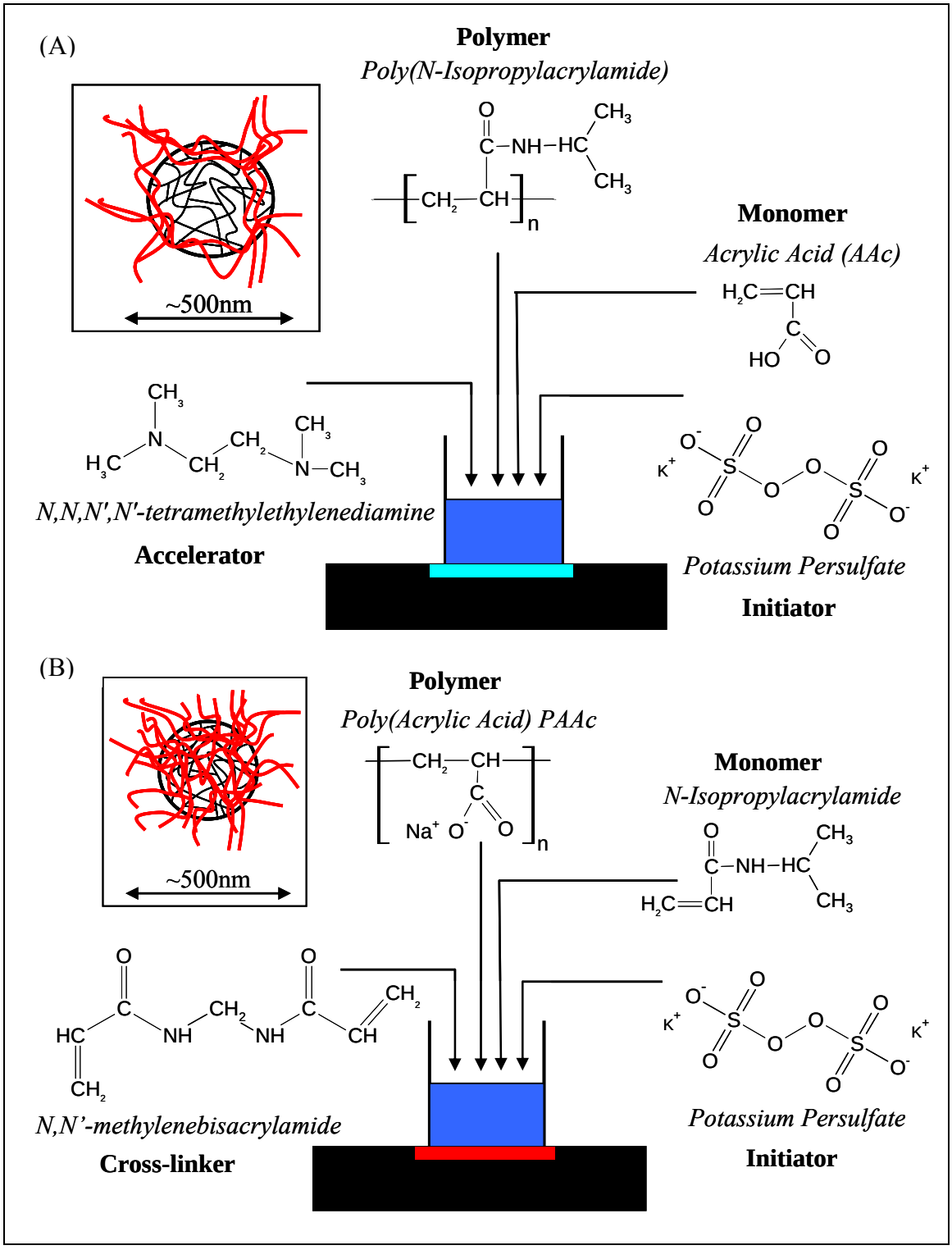

Figure 2.3: Synthesis setup for (A) peripheral penetrating microgel and (B) interpenetrating microgel where the insets show a schematic of a typical particle.

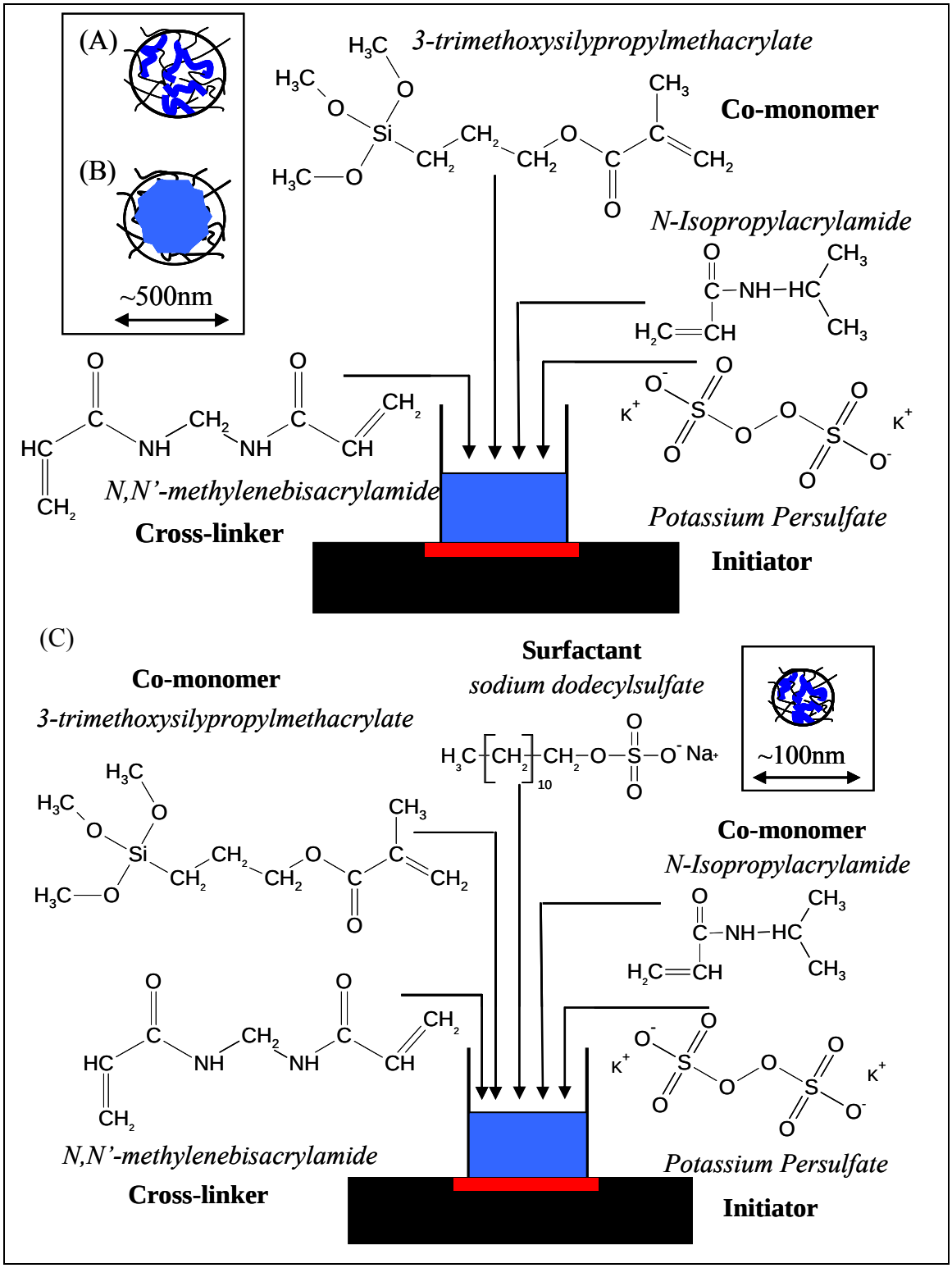

Figure 2.4: Synthesis setup for (A) siloxane-microgel hybrid, (B) siloxane-microgel core-shell, (C) siloxane-nanogel hybrid and inset shows a sketch of particle morphology.

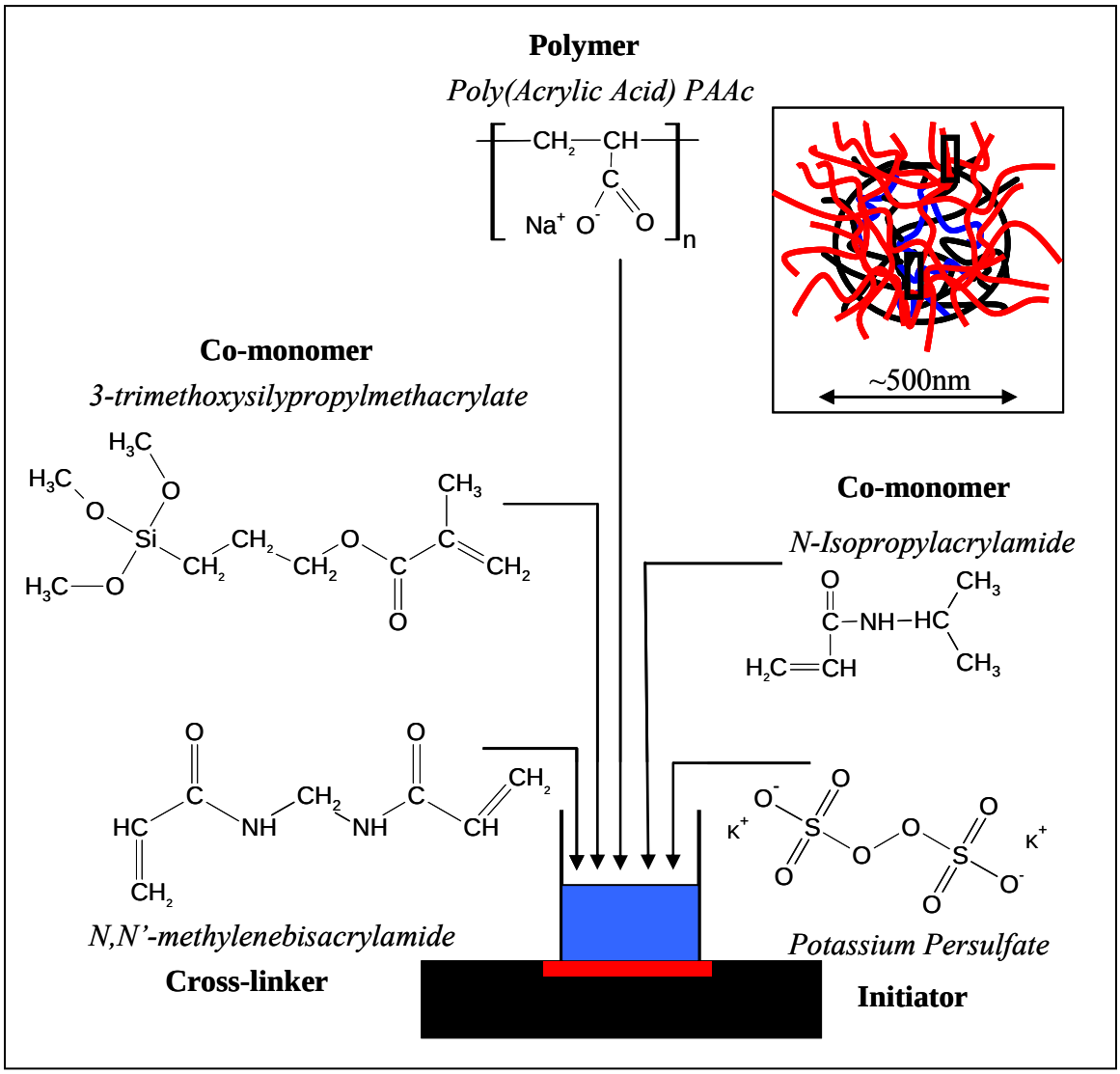

Figure 2.5: Synthesis setup for siloxane-microgel IP-hybrid, where the inset shows the particle morphology, such that PAAc (red), PNIPAM (black) and MPS (blue) co-exist.

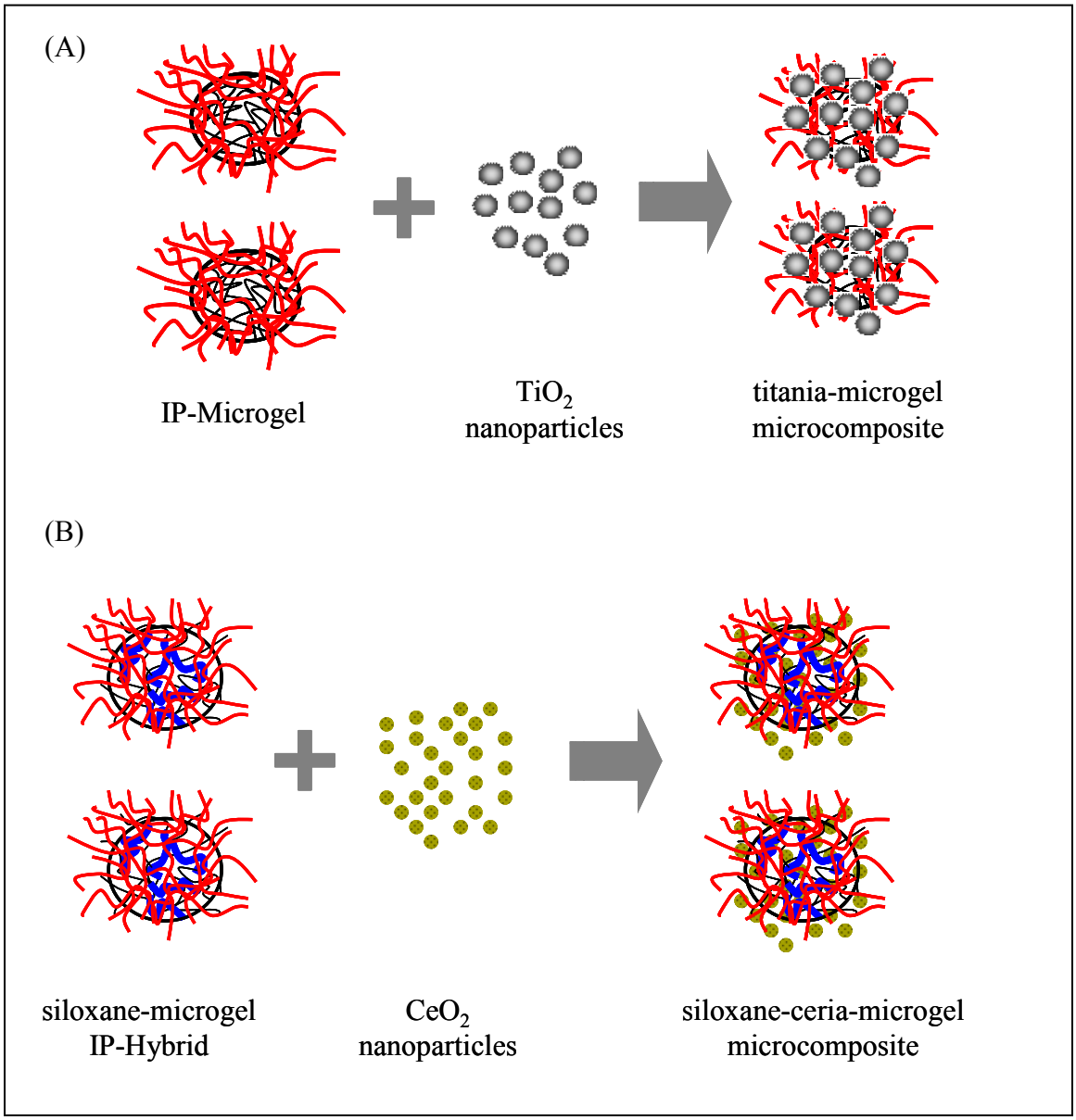

Figure 2.6: Schematic representing the preparation of (A) titania-microgel particles and (B) the ceria-siloxane-microgel particles.

CHAPTER 3: PHYSICAL CHARACTERIZATION OF MICROGELS AND THEIR COMPOSITES WITH TITANIA OR CERIA NANOPARTICLES

3.1. Introduction

To completely understand the morphology, chemical composition and bonding that existed within the synthesized polymer microgels and microcomposites, a host of characterization tools were utilized. These included microscopy, spectroscopy, thermal gravimetric analysis, total nitrogen (TN) analysis and light scattering. Extensive characterization was conducted of the microgels, hybrid microgels, and the microcomposites of ceria and titania. A simple and quick procedure was developed to analyze the titania content within the titania-microgel composite particles. In this chapter, the methods of characterization used during the doctoral research are listed. In addition the basic characterization of materials that have been synthesized in chapter 2 is discussed.

3.2. Material Characterization

- *Transmission Electron Microscopy (TEM)*: TEM was used extensively within this research to achieve a number of objectives. Dispersion of the inorganic oxides (TiO_2/CeO_2) within the microgels was qualitatively examined using TEM, as was the structural differences in the hybrid particles used for planarization studies. The sample preparation was typically achieved by placing a drop of the solution on a Formvar-coated

Cu TEM grid that was dried under a lamp in ambient conditions. The grid was then placed within the TEM (model FEI Morgagni 268D) vacuum chamber and examined.

- *Atomic Force Microscopy (AFM) and Optical Microscopy (AFM)*: Polished and unpolished silicon oxide surfaces used for CMP were imaged using a Digital Instruments Dimension 3100 Atomic Force Microscope that provided an overview of the pits, scratches and waviness of polished wafer surface. Surface roughness analysis of the wafer surface was also conducted using the images obtained from the AFM analysis. Optical microscopy of the wafer surfaces was conducted using a Leitz Ergolux Optical Microscope. This was done to confirm/refute the presence of surface defects on the polished wafer surface. Both, AFM and OM images were obtained in collaboration with Subrahmanya Mudhivarti (Research Group of Dr. Ashok Kumar, Department of Mechanical Engineering, USF).

- *Fourier Transform Infrared (FTIR) Spectroscopy*: FTIR was used to identify bonding peaks within the synthesized microgels/nanogels. This was conducted by pelletizing a small amount of dried gel with KBr, and analyzing the pellet with the spectrometer. Typically, the chamber was purged with dry N_2 gas, and then the spectrum obtained using 256 scans at a resolution of $2cm^{-1}$. In addition, FTIR was also used to characterize the silicon oxide coated wafer surface before and after CMP to determine organic particle residue from the microgels or degrading polymer polishing pad onto the wafer surface. The chamber was purged with N_2 gas, and the spectrum was obtained using 64 scans at a resolution of $2cm^{-1}$. The FTIR spectrum obtained above was used to qualitatively

characterize the oxide thickness by analyzing the peak corresponding to silica absorbance and will be described in more detail in chapter 6 that focuses on the CMP polishing using microcomposite and hybrid particles. In all infrared spectroscopy tests, a Nicolet Magna-IR 860 spectrometer was utilized.

- *UV-Vis Spectroscopy*: The concentration of titania (either in solution or within the polymer microgels) was determined quantitatively by measuring the UV-Vis absorbance of the titanyl ion. This peak absorbance was analyzed using a V-530 UV-Vis spectrophotometer (Jasco, MD). UV-Vis spectroscopy was also used extensively for the photocatalytic degradation studies. The degradation of the methyl orange contaminant was monitored by recording the peak absorbance decline at regular time intervals. These results will be further discussed in chapter 5 within the context of the photocatalytic studies.

- *Multi-angle Ellipsometry*: Removal rates of the oxide film were measured by characterizing the thickness of unpolished and polished wafers using a home-built ellipsometer. Light of wavelength of 633 nm from a helium-neon laser (05LHP073, Melles Griot, CA) was polarized by a Glan-Thompson polarizer (03PTH109/A, Melles Griot). The polarization of the light was subsequently modulated using a liquid-crystal (LC) variable phase retarder (LRC200, Meadowlark Optics, CO) and directed onto the silicon dioxide film of the wafer surface. The laser spot measured approximately 1mm - 2mm at the surface. Reflected light was analyzed using a second Glan-Thompson polarizer, and the intensity was measured using a Si photodiode (DET100, Thor Labs,

NJ). Control of the variable LC retarder and the data acquisition from the detector was performed using a program written in HP-VEE (version 4.0). Thickness measurements were made at a minimum of four different spots on each substrate at an incident angles of 75°, 70°, 65° and 60°. Typically, the average value of the removal rate with its standard deviation obtained from two different samples was used.

- *Thermal Gravimetric Analysis (TGA)*: To determine the inorganic-organic composition of the composite microparticles, a TA SDT Q600 thermal gravimetric analyzer (TGA) was used. Samples were heated in air at a rate of 2°C/min from room temperature to 500°C. TGA experimentation was conducted with the help of Gregory McManus (Dr. Michael Zaworotko Group, Department of Chemistry, USF).

- *Dynamic Light Scattering (DLS)*: The sizes and polydispersities of all microgels, nanogels, titania and ceria were determined via dynamic light scattering (DLS) using a Malvern Nano-S Zetasizer. Samples were sonicated prior to analysis. The sample solution was placed into a polystyrene cuvette and allowed to thermally equilibrate to a pre-determined temperature for 10 min before each set of measurements. Data fitting was done using a multi-modal algorithm supplied by Malvern with the instrument. The collected correlelograms were fit to diffusion co-efficients and converted to a hydrodynamic diameter by the instrument software.

- *Turbidometry*: In turbidometric studies, a HF scientific, model DRT 1000 was utilized, where the light scattered at 90° to the incident beam was measured as a voltage

signal from the photodetector. Typically, 1000 points were acquired at an A/D sampling frequency of 1 kHz and the mean was recorded as a function of time with a 30s time delay between readings. Turbidometry served two purposes within this dissertation work. Firstly, turbidometry was used to determine the rate at which the titania nanoparticles and titania-microgels settled. These sedimentation results are described in greater detail in chapter 4. Secondly, turbidometry was used to analyze the rate of degradation of the titania-microgels under UV-illumination. These results are part of chapter 5.

- *Total Organic Carbon/Total Nitrogen (TOC/TN) Analysis*: The ratio of the polyacrylic acid to PNIPAM within the IP-microgels was determined using a Shimadzu TOC-VCSH with TNM-1 TN unit total nitrogen analyzer. Here the total mass of nitrogen detected was attributed to the PNIPAM of the PNIPAM/PAAc microgels. 25ml of the IP-microgel solution (at a pre-determined concentration) was injected into the TOC/TN analyzer, which was burnt at ~600°C from which the mass of nitrogen was detected. TOC/TN experimentation was conducted with the help of Ana Prieto (Dr. Daniel Yeh Group, Department of Civil & Environmental Engineering, USF).

3.3. Results and Discussion

3.3.1. DLS, TEM and TN Analysis of Polymer Microgels

When microgels polymerized with only NIPAM were used to incorporate TiO_2 nanoparticles, the photocatalyst rinsed out immediately during the washing of the microcomposites. This indicated that the porous framework of the microgel did not retain the nanoparticles in the absence of any specific interaction with the polymeric matrix. To

remedy this, the incorporation of acrylic acid groups within the microgel to enhance the retention of TiO_2 within the polymeric matrix was pursued. Prior studies have shown that deprotonated sulfonic and carboxylic acid groups can functionalize inorganic oxide surfaces[18, 53]. However, it is also well known that the incorporation of acrylic acid as a co-monomer with NIPAM to form random P(NIPAM-AAc) copolymers disrupts the hydrophilic/hydrophobic balance with the solvent[39, 54]. As a result, this not only results in a shifting of the volume phase transition of the microgel but more importantly, the amount of AAc in these random copolymer systems has to be limited. Large amounts of AAc present as co-polymers do not yield microgels by free radical polymerization, but rather leads to the formation of macroscopic gels. To circumvent these problems, microgels with interpenetrating linear chains of PAAc were prepared to maintain the temperature responsive behavior and phase transition nature of PNIPAM microgels. Additionally, it serves to introduce significant proportions of carboxylic acid moieties that are known to interact with the oxide surface of inorganic nanoparticles.

Figure 3.1 shows transmission electron microscopy (TEM) images of both the IP-microgels and PP-microgels. To clearly visualize the interpenetrating chains of PAAc, the sample was stained using uranyl acetate that has been shown to selectively stain the polyacrylic acid within the PNIPAM-PAAc paritcle[557]. Both images strongly suggest that PAAc constitutes a significant fraction of the polymeric particle. However, the dark spots on the periphery of the PP-microgels indicate a significant localization of the PAAc within this region. Figure 3.1 also shows that the IP-microgels were synthesized with the NIPAM polymerizing around the deprotonated PAAc chains. These IP-microgels have a more even distribution of the PAAc across the entire microgel. This difference in

structure arises due to the gradient in cross-linking density that exists within the PNIPAM microgel. It has been well established that the interior of the PNIPAM microgel is densely cross-linked and the outer regions are sparsely cross-linked[31]. It is for this reason that the polymerization of the AAc monomer in a dispersion of the PNIPAM microgels (PP-microgel) leads to greater incorporation of PAAc towards the exterior of the microgel.

The DLS data shown in figure 3.2 clearly shows that there is no change in the hydrodynamic diameter of the PP-microgels when compared with the original PNIPAM microgel. The average collapsed size of the PP-microgel is approximately 280 (±38) nm while that of the PNIPAM microgel is 270 (±38) nm. However, the IP-microgel displays a significant increase in size as shown in figure 3.2 with the collapsed diameter measuring roughly 330 (±18) nm. This increase has been attributed to the polymerization of the NIPAM monomer around deprotonated chains of PAAc. The resulting electrostatic repulsion from the carboxylic acid moieties creates a slighter larger microgel during the synthesis. The size of the PP-microgels was first established during the initial polymerization of PNIPAM with no AAc present. No appreciable increase in size occurred during the second polymerization during which the polymerization of AAc was conducted in solution and within the swollen PNIPAM microgels. While hydrogen bonding interactions are possible between protonated PAAc chains and the PNIPAM amide side chains, literature has shown that such interactions are negligible[56].

The two synthesis routes used for the preparation of the IP and PP microgels and the measurements by TEM and DLS show important differences from recent reports by Xia[49] and Das[35]. Xia and coworkers performed the polymerization of AAc monomer in a

dispersion of PNIPAM microgels to get interpenetrating networks of PAAc, rather than interpenetrating linear chains of PAAC within the PNIPAM matrix (that has been described in this dissertation). Although a few similarities exist between their procedure and the techniques used to produce the PP-microgels here, two important differences exist. First, Xia and co-workers used much smaller PNIPAM microgels (~120nm) compared to the experiments described here (~700nm). Secondly, the temperature at which the polymerization of AAc was performed was 21°C as compared to 0°C in this study (that was chosen to allow maximum swelling of the PNIPAM for maximum PAAc integration within the porous PNIPAM microgel). The study performed by the Xia group resulted in a substantial (~75%) increase in size after the PAAc formation. This led them to infer that the particles had a core-shell structure with a core of PNIPAM and a shell of PAAc. This morphology had significant impact on the aggregation state of the particles while also leading to a much smaller ratio between the swollen and the shrunken state because the PAAc in the shell regions does not respond to temperature. In contrast to the studies by Xia and co-workers, the TEM results detailed in this study (figure 3.1) suggest that there is some tendency for localization of the PAAc at the periphery in the case of the PP-microgels but it is not as extreme as a core-shell structure. This occurs because the starting point for the synthesis of the PP-microgels is a larger PNIPAM microgel that is more swollen with sparsely cross-linked outer regions. As a result, there is no appreciable increase in size after the PAAc polymerization (figure 3.2) and the swelling ratio remains practically the same as that observed for the PNIPAM microgels before the PAAc incorporation.

Das and coworkers[35] have prepared interpenetrating networks of PAAc with microgels formed from copolymers of NIPAM and *N*-isopropylmethacrylamide (NIPMAM). Their procedure was similar to the steps used in this dissertation research for preparation of IP-microgels. In both instances, the microgels were formed in a solution containing PAAc. Das et al. reported a decrease in microgel size due to the presence of interpenetrating chains of PAAc. They speculated that this could be due to hydrophobic interactions between short PAAc chains and the methacrylamide segments. However, in figure 3.2 the IP-microgels that have been prepared here show an increase in size. Additionally, Das and coworkers also report a significant decrease in the swelling ratio of the interpenetrating network compared to the non-IPN case whereas figure 3.2 clearly shows that the IP-microgels have similar swelling ratio to the PNIPAM microgels. However, even though Das and coworkers used a copolymer system of NIPAM with NIPMAM (while only NIPAM was used in this study), the differences between the results reported here and the past study can be attributed to the other variations in experimental details. In experiments reported in this dissertation, a high molecular weight of PAAc (M_w~15000) was used and a larger portion of PAAc (f~50%) was incorporated into the PNIPAM microgel as compared to that by Das et al. (M_w~2000; f~2%). The longer, hydrophilic PAAc chains and the higher fraction can likely, lead to increased electrostatic repulsion and retention of water. This would account for the slight increase in size as well as the preservation of the swelling ratio.

To incorporate TiO_2 within the microgels, this doctoral study has primarily focused on using IP-microgels for the fabrication of the titania-microgel particles. This was due to the ease of synthesis (one step polymerization) and even distribution of PAAc

within the microgel. As shown in figure 3.3, it was ascertained that the IP-microgels contained ~48% by mass of Poly(Acrylic Acid) using the TN analysis. Even though IP-microgels contained a significant fraction of the very hydrophilic polyacrylic acid, the distinct and spherical nature of the original PNIPAM microgel was maintained. Additionally, figure 3.4 shows the appearance of turbidity due to phase separation of the IP-microgels when the sample was heated above the transition region. At room temperature the dispersion of the IP-microgel is transparent, similar to that of the PNIPAM microgels.

It is known that P(NIPAM-AAc) co-polymer with large amounts of AAc as a co-monomer will not yield microspherical gels. Additionally, microgels of P(NIPAM-AAc) that contain significant amounts of AAc undergo a large charge repulsion between carboxylic acid segments. This charge repulsion can become sufficiently high that the microgels no longer exhibit thermally responsive behavior or shrinking at high temperatures[31, 56-58]. Figure 3.2 clearly indicates that by using interpenetrating chains of PAAc, the temperature responsiveness and phase transition behavior of the PNIPAM microgels was successfully maintained, while introducing significant (~48%) proportions of carboxylic acid moieties to interact with TiO_2 nanoparticles. Also, the presence of the PAAc does not significantly affect the LCST behavior of PNIPAM, as all three polymeric systems shown in figure 3.2 phase transition at approximately 32°C. The change in size of the PNIPAM and IP-microgels with temperature is reversible with temperature and the microgels can be cycled between swollen and collapsed states as shown in figure 3.5. The hydrodynamic diameter of both microgels was analyzed by increasing the temperature from 25°C to 40°C and then cooling this microgel solution down from 40°C to 25°C. The

scatter from the data is not significant, indicating that both the PNIPAM and IP-microgels are quite monodisperse. Also, it should be noted that the IP-microgels are substantially larger than the PNIPAM microgels in both temperature cycles.

3.3.2. TEM, UV-Vis and TGA Study of Titania-Microgel Particles

The broad infrared absorbance of titania from 400-1000cm^{-1} is shown in figure 3.6. This absorbance peak is also seen in the titania-microgel composite but absent in the spectra of the IP or PNIPAM microgels, thereby confirming the presence of titania within the microcomposite. Absorption peaks at 1650cm^{-1} and 1550cm^{-1} due to bending vibrations are indicative of the amide I and II absorption bands that originate from the PNIPAM polymer. Also the twin peaks at 1385cm^{-1} and 1365cm^{-1} both confirm the presence of the isopropyl side chain within the final structure of the PNIPAM microgels, IP-microgels and titania-microgels.

The loading of the TiO_2 within the microcomposite material was be easily tailored by careful selection of the mixing ratios of the TiO_2 and IP-microgel stock solutions. Table 3.1 shows the different mass ratios for IP-microgel and TiO_2 that was used in this work. Sample 'C10S' refers to the microcomposite containing sol-gel synthesized ultrafine TiO_2 whereas the rest of the titania-microgel samples were synthesized using the commercial available, well-studied Degussa™ P25. For a quantitative determination of TiO_2 loaded in the microgels, the microcomposite was first dried under vacuum and then treated with boiling concentrated sulfuric acid and ammonium sulfate in a 4:1 mass ratio. A few drops of 30 wt% H_2O_2 were then added to the cooled solution to oxidize the degraded polymer and then the solution was reheated. An additional amount of H_2O_2 was

added to develop the colorless titanyl ion into the intensely yellow-red colored peroxotitanyl ion TiO_2^{2+}. The peroxotitanyl ion formed shows an absorbance at 405nm that was measured using UV-Vis spectroscopy. A linear calibration curve that was previously developed in our lab that related the mass of TiO_2 and spectral absorbance, was used to assay the TiO_2 content in the microcomposite[18]. Figure 3.7 shows the UV-Vis results that provide a simple colorimetric quantification of the TiO_2 content in microcomposites. A strong characteristic absorbance at 405nm is observed due to the complex between the titanyl ion (TiO_2^+) and hydrogen peroxide as shown in figure 3.7 where Mie scattering of the solution is at a minimum. The intensity of the absorbance increases with TiO_2 content.

Table 3.1: Comparison of TiO_2 loading in the microcomposites.

Sample ID	% (mass) of TiO_2 mixed	% (mass) of TiO_2 measured by UV-Vis analysis
C10	11.3	10.3
C25	27.2	24.8
C75	80.1	74.6
C10S	9.6	9.2

When the IP-microgel and TiO_2 stock solutions were mixed, the high proportion of poly(acrylic acid) within the IP-microgel resulted in a large transfer of TiO_2 from the surrounding solution into the IP-microgels. This is evident from table 3.1 where a good agreement exists between the mixing ratios and the TiO_2 content assayed from the UV-Vis absorbance approach. Only at the highest loading, a discrepancy (~5%) occurs since not all of the TiO_2 can be loaded within the microgels. We believe that 75% loading of titania appears to be an upper bound for the microcomposite synthesis. In perspective,

this is a very high mass loading of titania and can be likened to a large, yet very porous titania particle of approximately half a micron in diameter. This fractal aggregate allows easy entrainment of fluid within itself, creating an optimum photocatalytic system for wastewater remediation. Sample C10S was also analyzed by TGA as shown in figure 3.8 to confirm the accuracy of the simple colorimetric quantification from the UV-Vis technique. TGA showed that the microcomposite C10S had 9.5 wt% TiO_2 which agrees well with result from the UV-VIS assay. The UV-Vis analysis is particularly useful since it quick, but more importantly specific to titania. Thus, it can be extended to other inorganic-organic microcomposites that contain a mixture of oxides with TiO_2 as one of the constituents.

TEM characterization further reveals the unaggregated and dispersed state of the titania nanoparticles within the polymer matrix. TEM images in figures 3.9A-D show the microcomposites made from IP-microgels and TiO_2 with different loading of the TiO_2 from different mixing ratios. It is clearly shown that the nanoparticles of TiO_2 are quite well-dispersed and largely unaggregated within the microgels. From the figures 3.9A-C, it is observed that the Degussa^{TM} P25 is ~70nm while the ultrafine synthesized TiO_2 in figure 3.4D is ~10nm. These results are also confirmed using DLS wherein the Degussa sample's size distribution showed a major peak at 71 (±17) nm and a minor peak at 310 (±62) nm while the synthesized TiO_2 sample showed a size distribution centered at 4 (±1) nm.

Neither the IP-microgel nor the TiO_2 settle when present as separate entities. However, the resulting microcomposite settles readily due to the significant increase in the density of the titania-microgels and significant porosity that exists within the particles

and the fractal aggregates overall. Sedimentation studies were conducted by studying the decrease in turbidity from a solution of the microcomposites as a function of time measured using a turbidometer. This will be discussed in further detail in chapter 4.

3.3.3. Investigation of Hybrid Microgels Using FTIR, TEM and DLS

The incorporation of functional groups into polymer networks to form new hybrid materials represents an emerging discipline for the synthesis of novel materials that comprise of diverse architectures[51, 52, 59-63]. One area of application is the preparation of abrasive particles with controllable texture and surface hardness that can significantly improve the surface finish in the CMP process. Towards this end, this study has focused on using hybrid microgels of soft polymeric networks based on PNIPAM with hard inorganic components. This was achieved by preparing hybrid microgels that contained siloxane functional groups incorporated into the polymeric network by co-polymerizing NIPAM with MPS. The starting mass ratio MPS/NIPAM was varied during synthesis (up to 40%) and the bulk FTIR spectra of the hybrid microgel particles that were produced are shown in figure 3.10. For comparison, spectra are shown for microgels containing only PNIPAM (blue). The shoulder peak at 1727cm^{-1} corresponds to the carbonyl stretching from the methacrylate functionality in MPS. Increasing the MPS to NIPAM ratio in the polymerization mixture, results in an increase in the intensity of the peak at 1727cm^{-1} that indicates greater incorporation of the co-monomer in the hybrid microgel. The black spectrum corresponding to 40%-MPS-NIPAM hybrid microgel has the most pronounced peak due to the carbonyl of the methacrylate group and the green spectrum for the 10%-MPS-NIPAM hybrid microgel has the weakest peak at 1727cm^{-1}.

PNIPAM-based materials have been of tremendous interest because they are thermally responsive due to a delicate hydrophilic–hydrophobic balance that exists between the amide and isopropyl side chains[35, 44, 54]. Figure 3.11 shows the change in hydrodynamic diameter of the hybrid microgels with temperature as characterized by DLS. The decrease in the microgel size with increasing temperature is due to the well known volume phase transition[40]. As shown in figure 3.11, microgels prepared using a high MPS to NIPAM ratio of 40% are not temperature responsive. This occurs due to the formation of a thin silica shell encapsulating the polymeric core of the hybrid particle. TEM images in figure 3.12A confirm this hypothesis, where the roundness of the particle can be attributed to the silica shell, while the transparency occurs due to the thinness of the shell that allows for penetration of the electrons through the interior of the particle that contains mostly polymer. It should be noted that a polymerization mixture with a MPS to NIPAM ratio of 10% results in particles that are thermally responsive and the swelling ratio is same as the microgels that contain no MPS. The material remains temperature responsive when the MPS to NIPAM ratio is 25% in the reaction mixture but the swelling ratio decreases. Figure 3.12B shows TEM images of hybrid particles that contain only 25% MPS, and the segments of silica as opposed to a complete shell are clearly seen.

Various other abrasive particles were pursued for the polishing of oxide wafers. Core-shell particles that were synthesized contained a core of silica and a shell of PNIPAM. Since PNIPAM is thermally responsive, the thickness of the shell could be manipulated by changing the temperature of the slurry solution. Below the LCST (~32ºC), these particles possessed thick, expanded shells, while above the LCST, the

polymer shell collapses onto the silica core. TEM images confirm the core-shell morphology of these particles as shown in figure 3.13A. Siloxane-nanogel hybrid particles were also synthesized for polishing applications. These particles tend to possess a higher surface area to volume ratio that would be favorable for increased wafer-particle contact, thereby leading to increased abrasion. TEM images of these hybrid nanogels are shown in figure 3.13B. Due to increased magnification, the resolution of the image tends to be not as sharp as the previous images of siloxane-microgel hybrid particles, making it slightly more difficult to view the silica fragments from the PNIPAM. The synthesis techniques of both the hybrid nanogels and the core-shell particles are available in chapter 2 of this dissertation. FTIR spectra shown in figure 3.14 were used to further characterize the presence of siloxane within the hybrid nanogels/microgels and core-shell particles. The shoulder peak due to the carbonyl of the methacrylate group (of MPS) at $1727cm^{-1}$ is clearly seen and absent in both the IP and PNIPAM microgels. Since the size of the shoulder peak is similar in the core-shell particles, siloxane-nanogels, and siloxane-microgels, it can be speculated that all particles have fairly similar amounts of silica fragments incorporated within the final structure. The temperature responsive behavior of these particles is shown in figure 3.15 and it reveals some interesting behavior. As expected, the hybrid nanogels are the most responsive particles with the core-shell particles being the least responsive. With the silica core firmly established, the PNIPAM shell can only extend beyond the unresponsive core, rather than the entire particle being responsive as is the case with the hybrid nanogels/microgels. Plausible arguments for the greater responsive behavior of the hybrid nanogels compared to the hybrid microgel is that the nanogel is not as cross-linked as the microgel, and the presence of the SDS

surfactant may hinder the complete incorporation of the MPS within the nanogel structure. Due to the poor CMP results that resulted with these hybrid particles, further characterization was not pursued.

3.3.4. Examination of Ceria-Microgel Particles Using TEM and TGA

To promote the incorporation of ceria nanoparticles into the hybrid microgels, a similar strategy of the synthesis of the titania-microgels was pursued[36, 60]. Interpenetrating chains of PAAc within the hybrid microgel led to significant fractions of carboxylic acid moieties in the hybrid microgel, which facilitated the incorporation of ceria nanoparticles within the microgels. By simply controlling the mixing ratios of the IP-hybrid microgel and ceria nanoparticles solution, the mass fraction of ceria within the siloxane-ceria-microgel particles was easily tailored. Figure 3.16 shows two types of ceria-microgels, one containing approximately 10wt% ceria and the other 50wt% ceria. In both TEM images, the dark spots correspond to the ceria nanoparticles (~20nm). It is evident that the ceria is well-dispersed and largely unaggregated within the microgel in both images. In the present study for CMP applications, the ceria-microgel suspension with approximately 50 wt% ceria was used so as to maximize oxide removal rates as detailed extensively in chapter 6 of this dissertation. Figure 3.17 shows the TGA characterization of the IP-hybrid microgels and the ceria-microgel composite particles. From the TGA analysis, it was determined that the inorganic fraction (silica) is approximately 5 wt% in the IP-hybrid microgel while the ceria-microgels contained ~50wt% inorganic.

3.4. Summary

In summary, several organic-inorganic microcomposites and hybrid particles were prepared and extensively characterized. Microgels of PNIPAM with interpenetrating linear chains of PAAc were prepared that had an AAc content of nearly 50% by weight but showed a volume phase transition at a temperature similar to that of the original PNIPAM microgels. The PAAc helped to stabilize CeO_2/TiO_2 nanoparticles within the microgels and the loading of CeO_2/TiO_2 within the colloidal particles was easily manipulated from a low value of 10% (weight) to a value as high as 75% for titania and 50wt% for ceria. In all cases, the inorganic nanoparticles were observed to be in a dispersed state within the microgels and the supernatant was devoid of inorganic nanoparticles, as shown by TEM imaging. Other particles including siloxane-nanogels and core-shell particles were characterized for subsequent use in CMP.

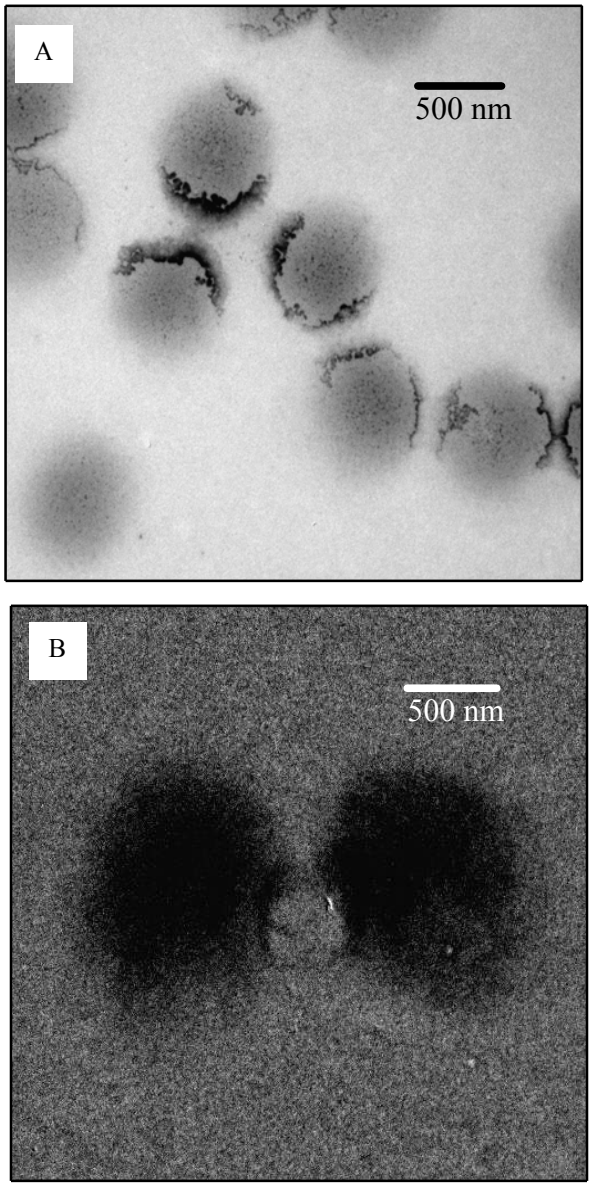

Figure 3.1: TEM images of (A) PP-microgel that has been stained with uranyl acetate (B) IP-microgel that has been stained with uranyl acetate.

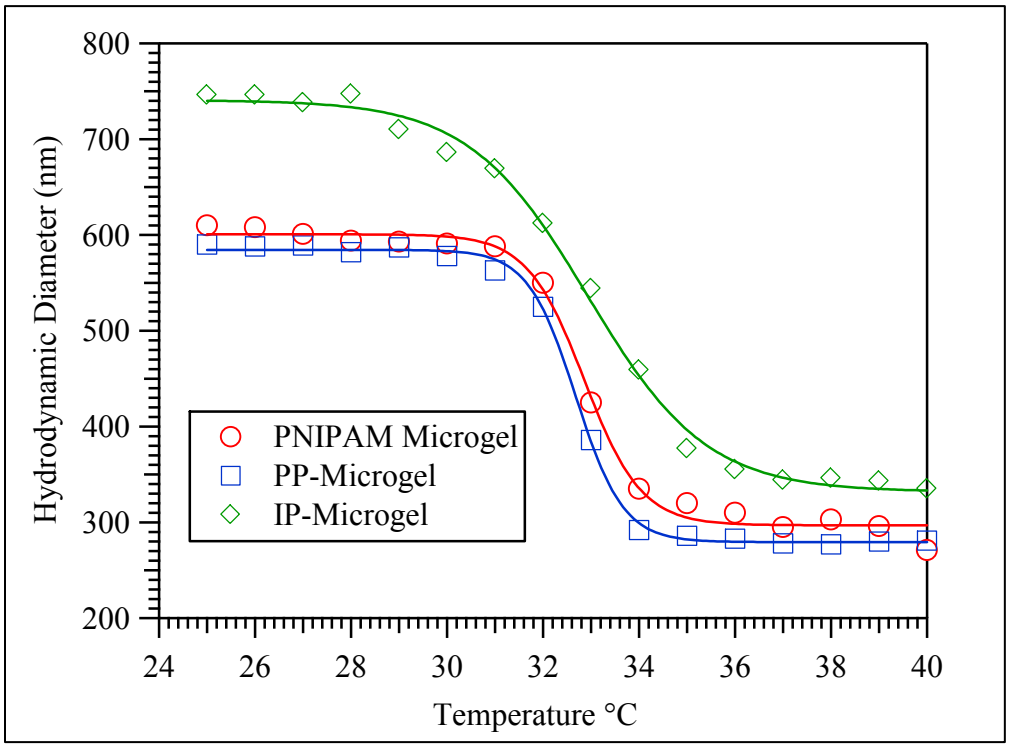

Figure 3.2: Variation in size of PNIPAM, interpenetrating (IP), and peripherally penetrating (PP) microgels from 40 to 25°C measured using DLS where the dashed lines are drawn only as a guide to the eye.

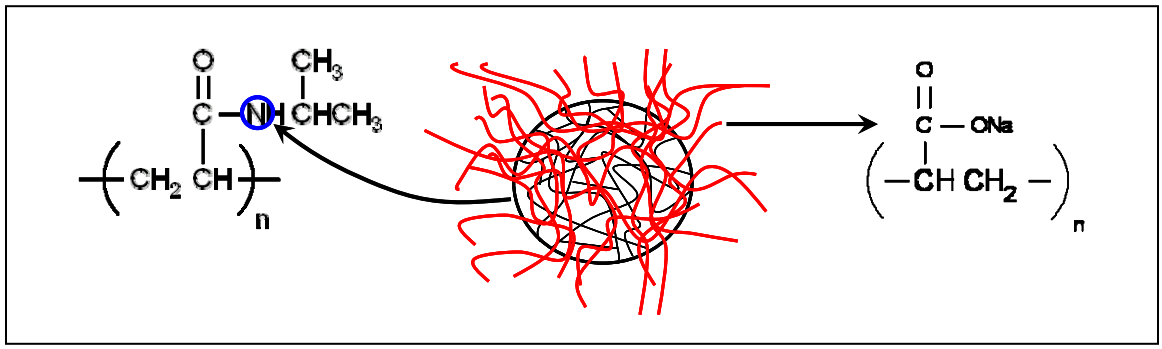

Figure 3.3: Total nitrogen analysis of IP-microgel.

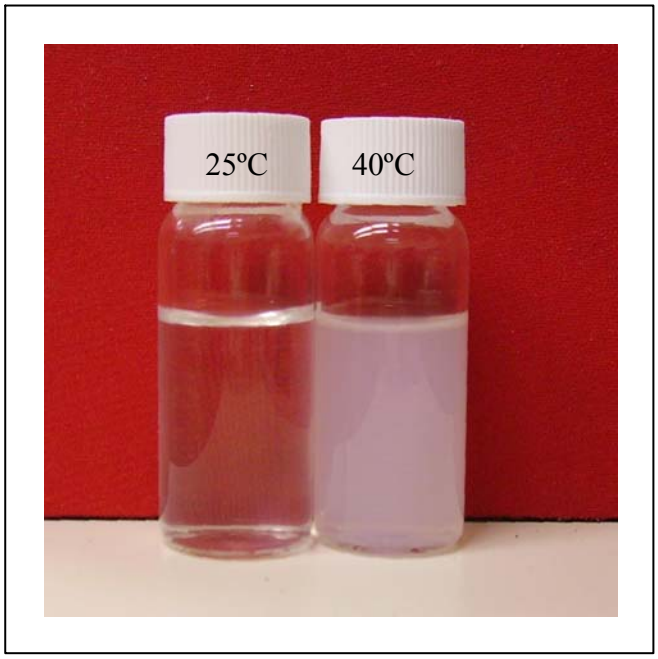

Figure 3.4: The digital image shows IP-microgels dispersed in DI water at 25°C (left) and 40°C (right).

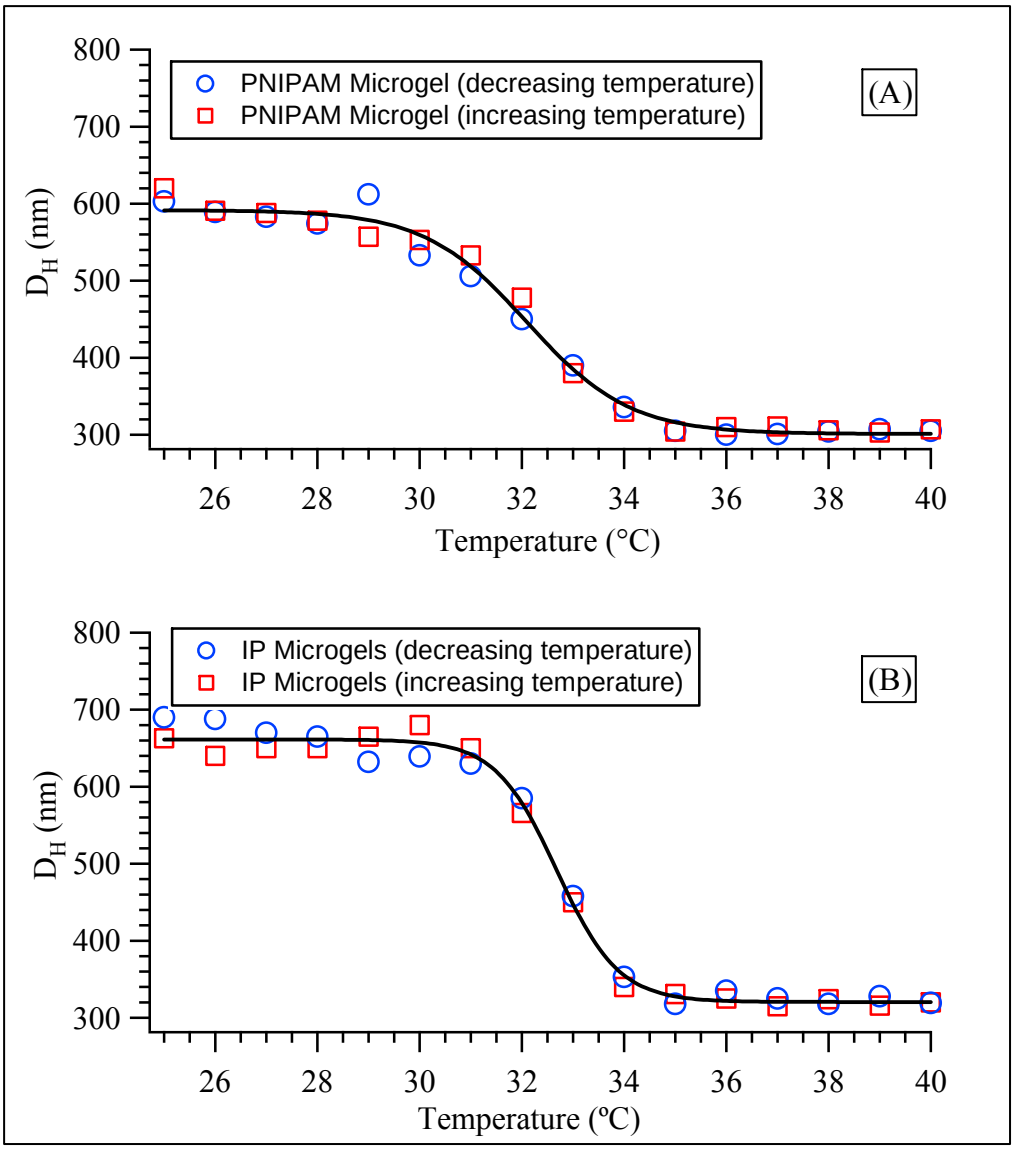

Figure 3.5: DLS measurements of (A) PNIPAM microgels cycled increasing and then decreasing in temperature and (B) IP-microgels cycled increasing and then decreasing in temperature.

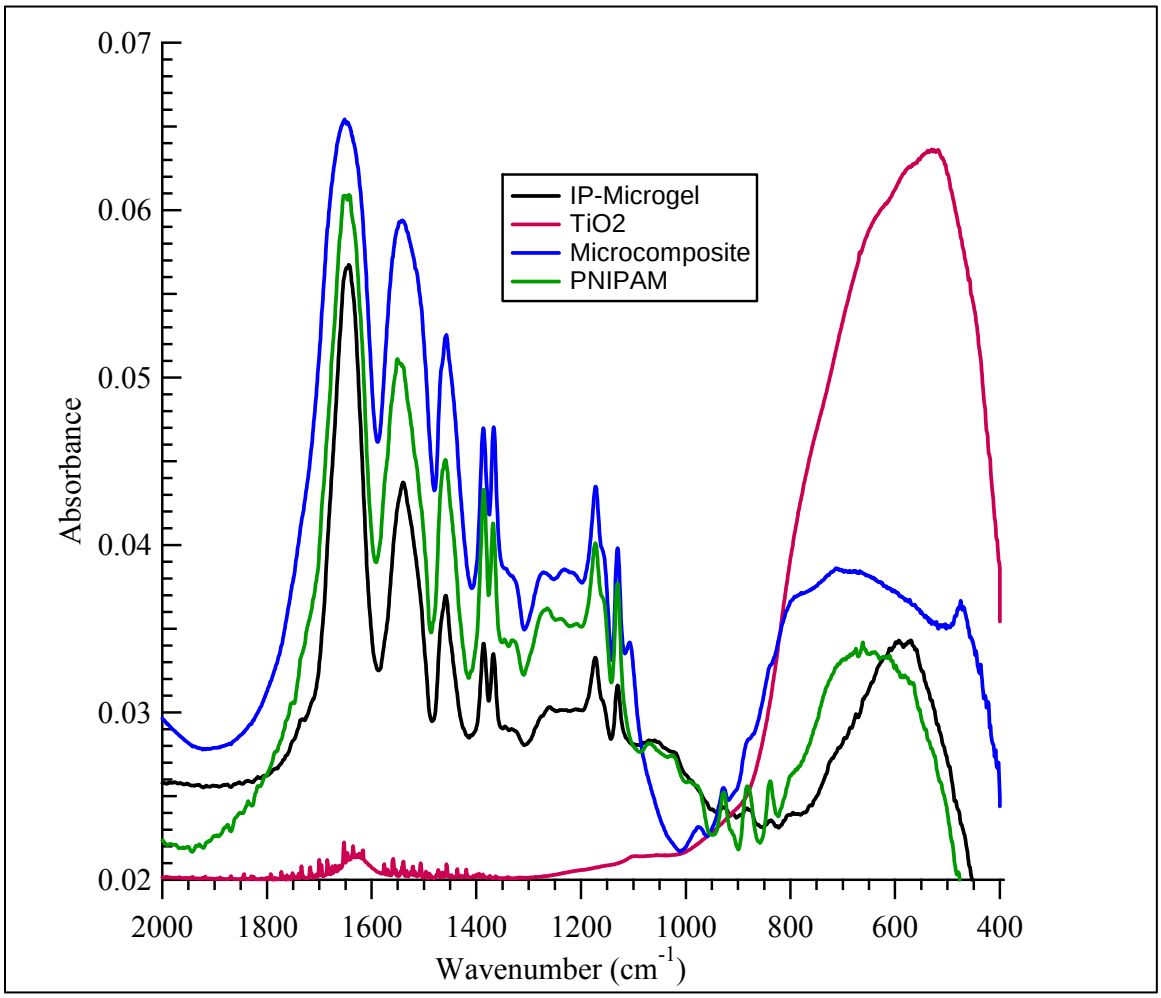

Figure 3.6: FTIR spectra of PNIPAM microgels (green), IP-microgels (black), TiO_2 (red) and titania-microgel microcomposites (blue).

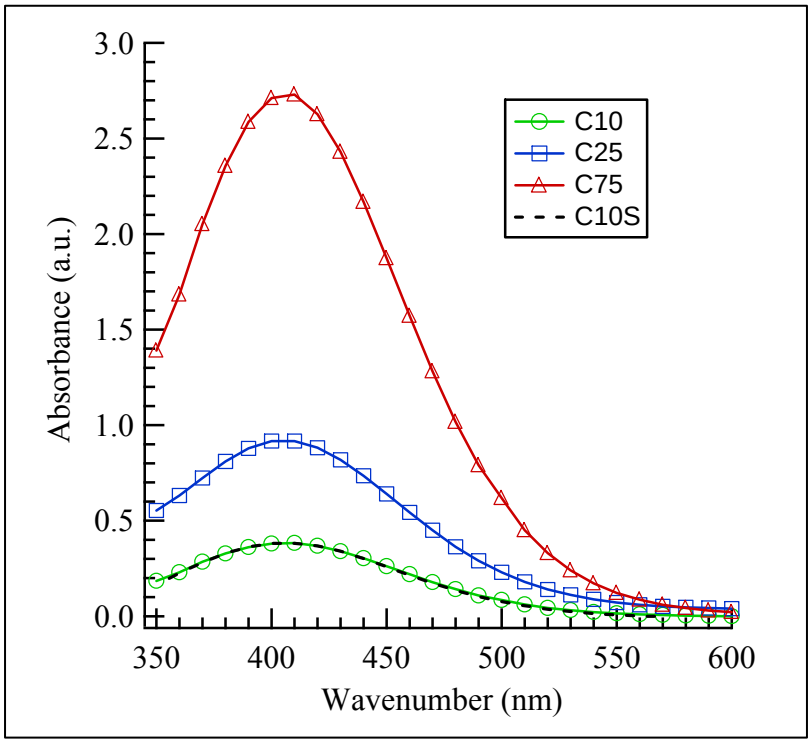

Figure 3.7: Absorbance spectra of titania-microgels with various loadings of TiO_2.

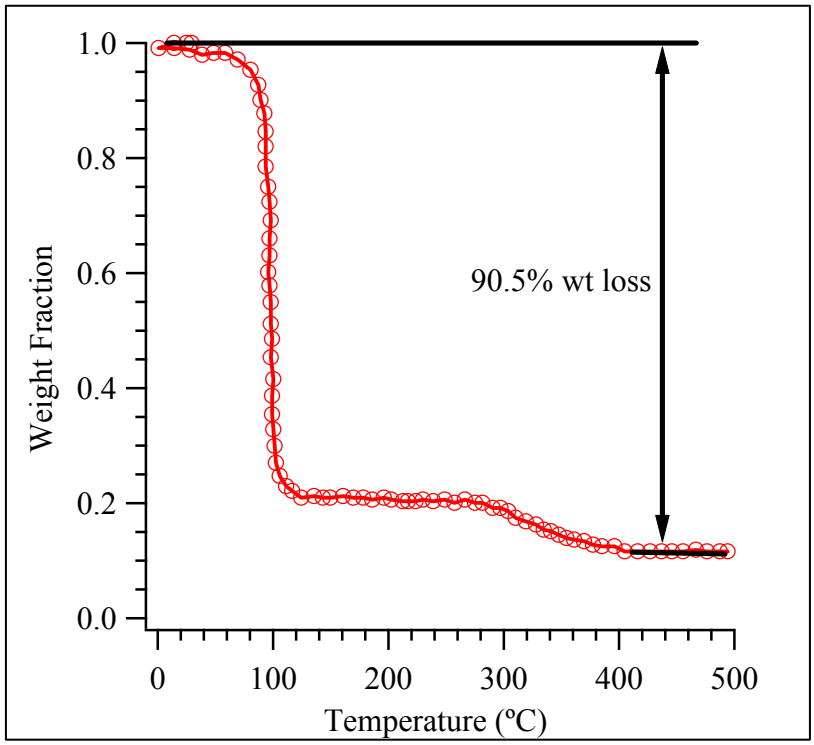

Figure 3.8: TGA analysis of sample C10S.

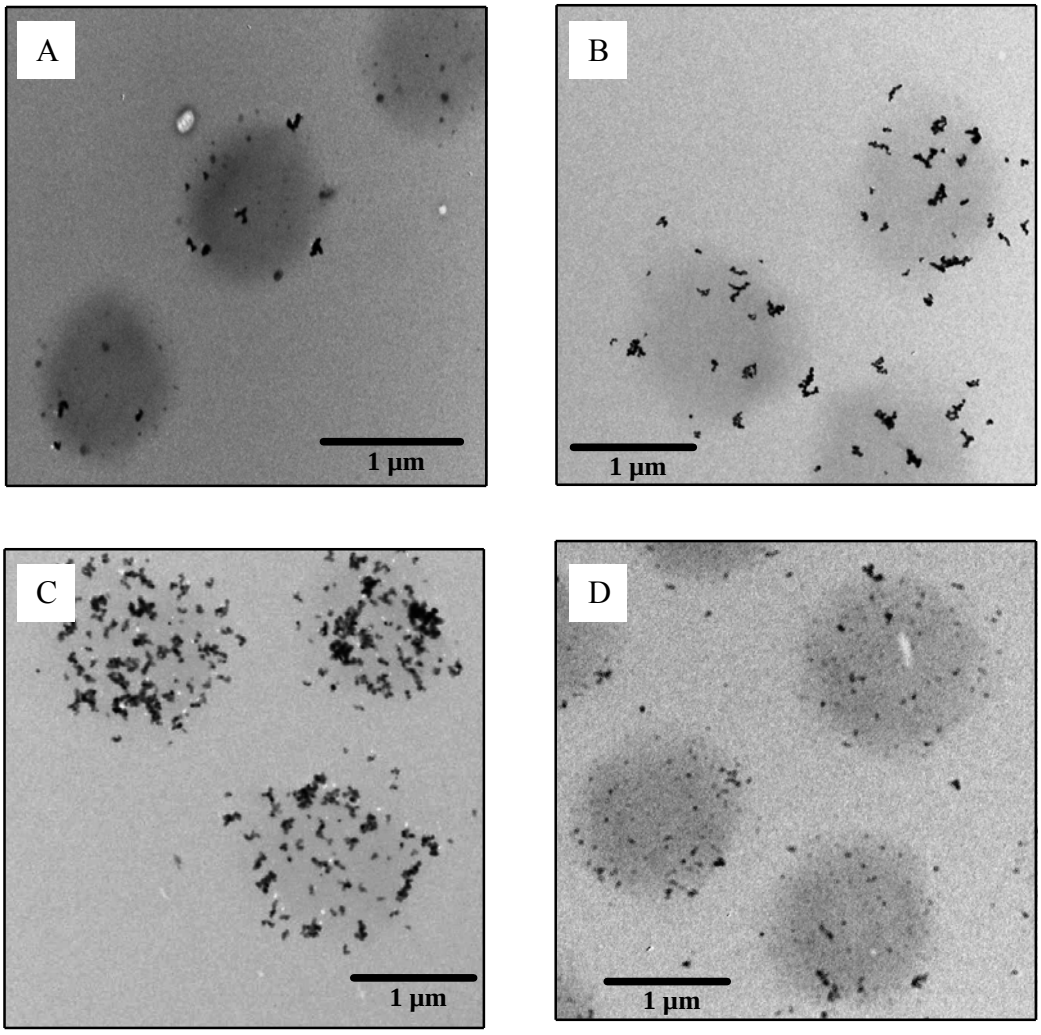

Figure 3.9: TEM images of microcomposites made using IP-microgel and titania (A) C10: 10wt% Degussa^{TM} P25 TiO_2, (B) C25: 25wt% Degussa^{TM} P25 TiO_2, (C) C75: 75wt% Degussa^{TM} P25 TiO_2, (D) C10S: 10wt% sol-gel synthesized TiO_2 nanoparticles.

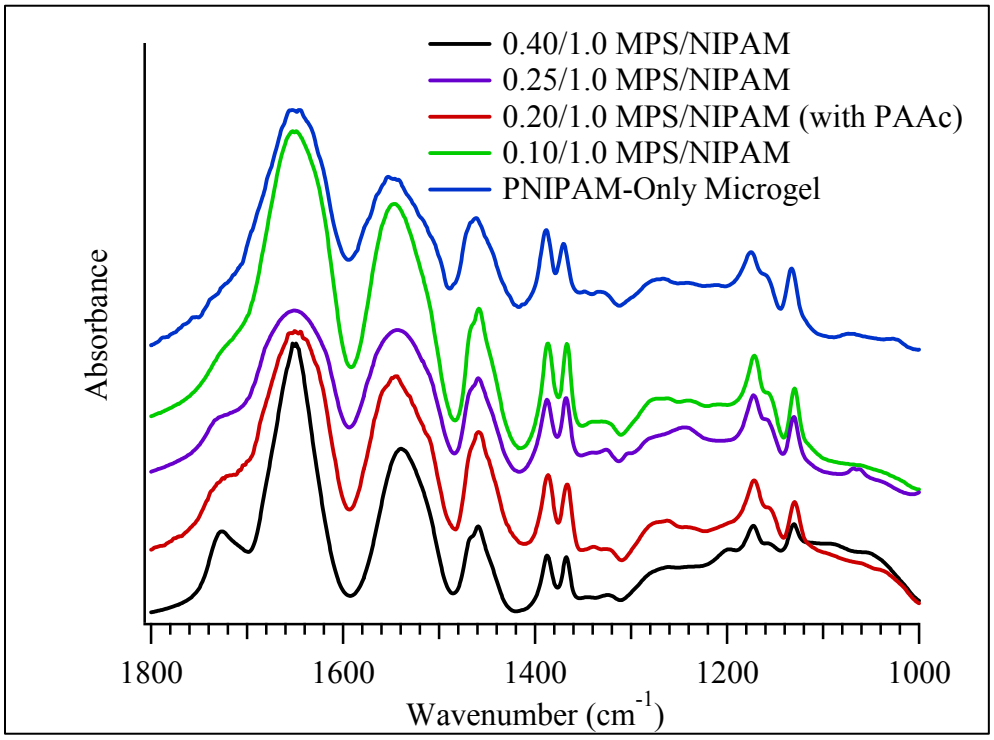

Figure 3.10: FTIR spectra of the siloxane-microgel hybrid particles made by varying the MPS ratio from 0 to 40wt%.

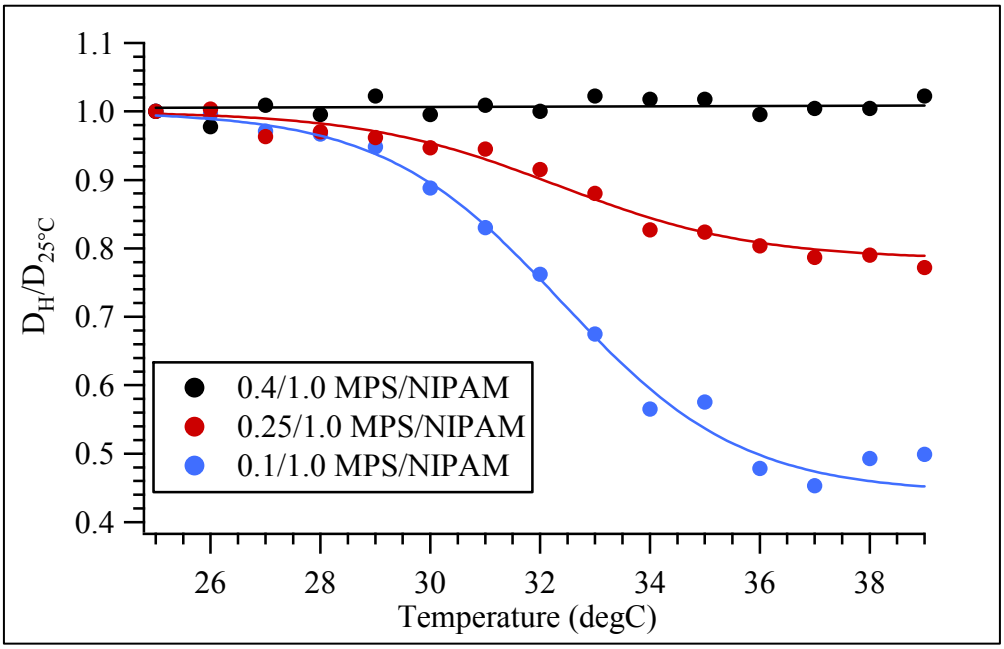

Figure 3.11: DLS of the siloxane-microgel hybrid particles made by varying the MPS ratio from 0 to 40wt%.

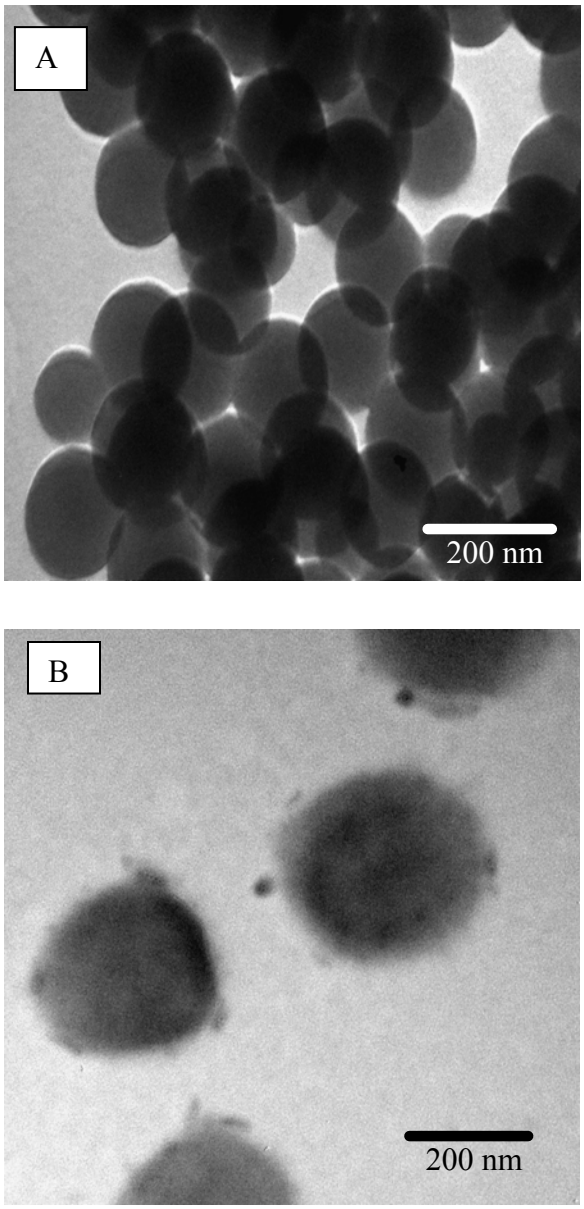

Figure 3.12: TEM images of (A) hybrid particle with an MPS/NIPAM synthesis ratio of 0.4/1.0 (B) hybrid particle with an MPS/NIPAM synthesis ratio of 0.25/1.0.

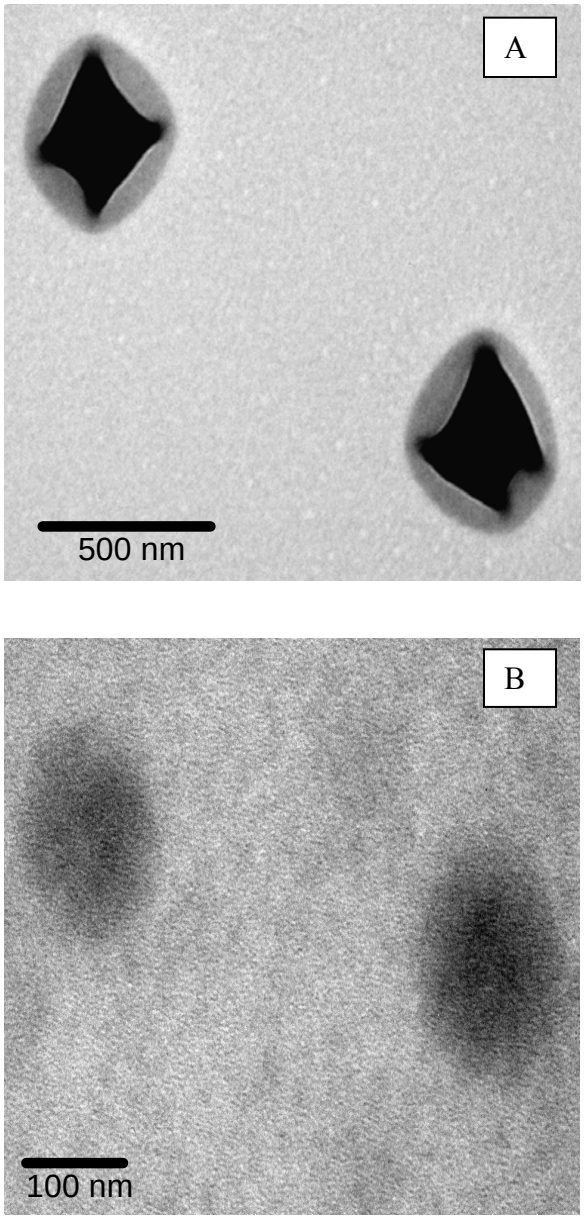

Figure 3.13: TEM images of (A) siloxane-microgel core-shell particle (B) siloxane-nanogel hybrid particle.

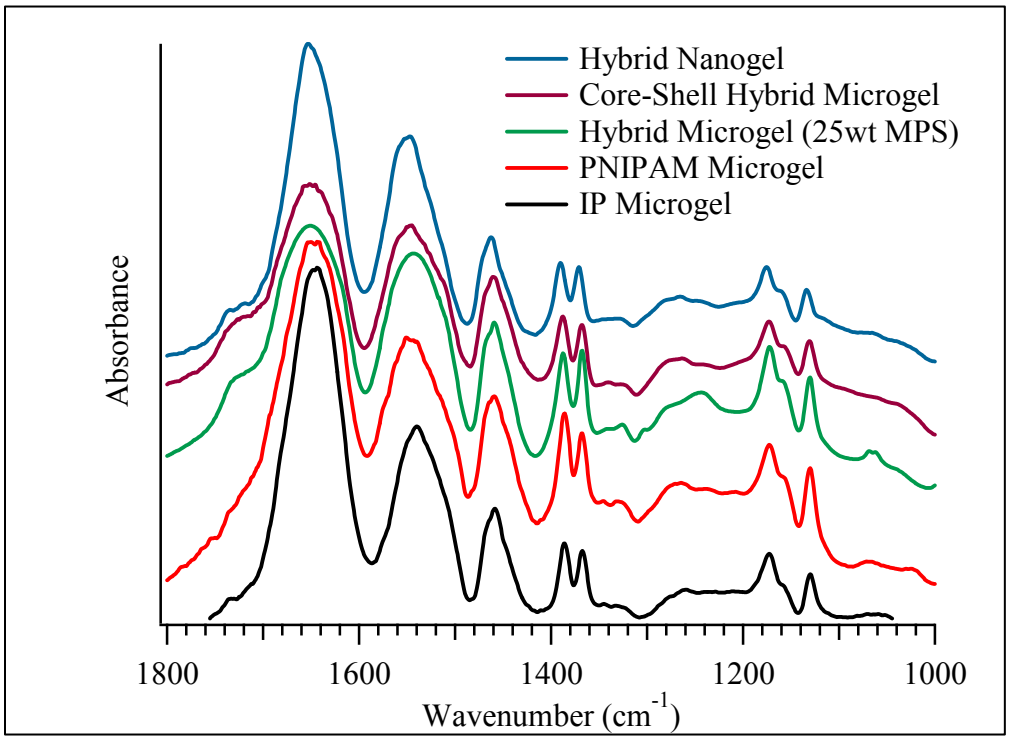

Figure 3.14: FTIR of hybrid microgels/nanogels and core-shell particles synthesized for CMP applications.

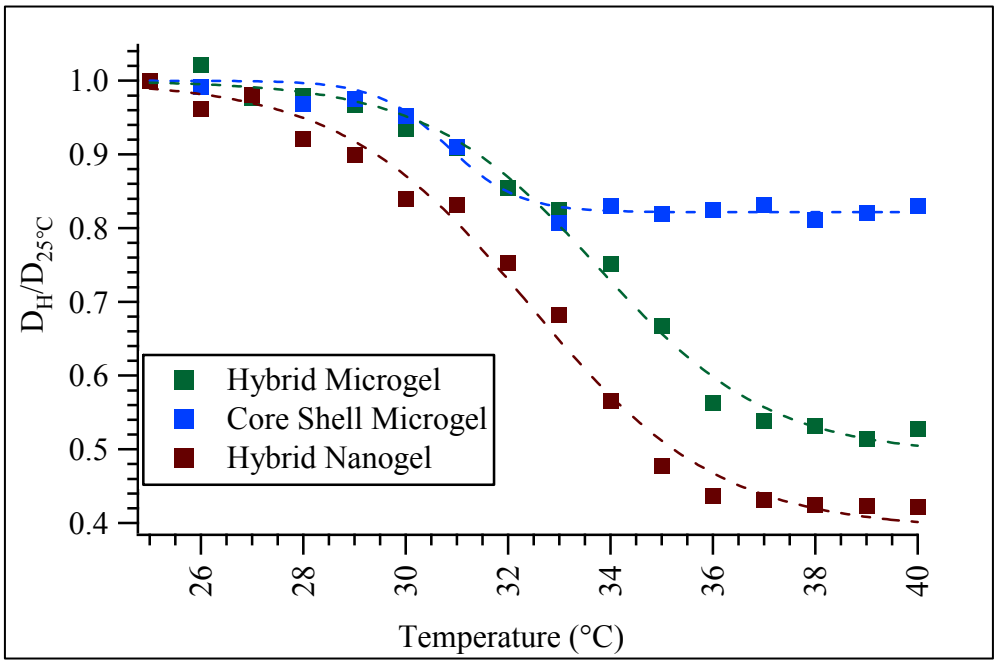

Figure 3.15: DLS of siloxane nanogels, microgels and core-shell particles.

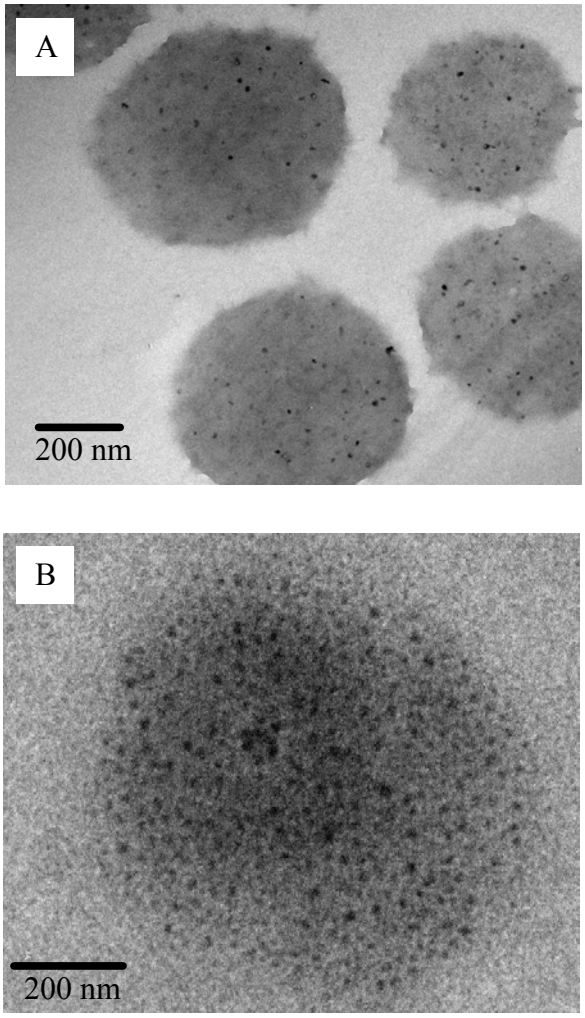

Figure 3.16: TEM images of siloxane-microgel IP-hybrid with (A) 10wt% ceria (B) 50wt% ceria.

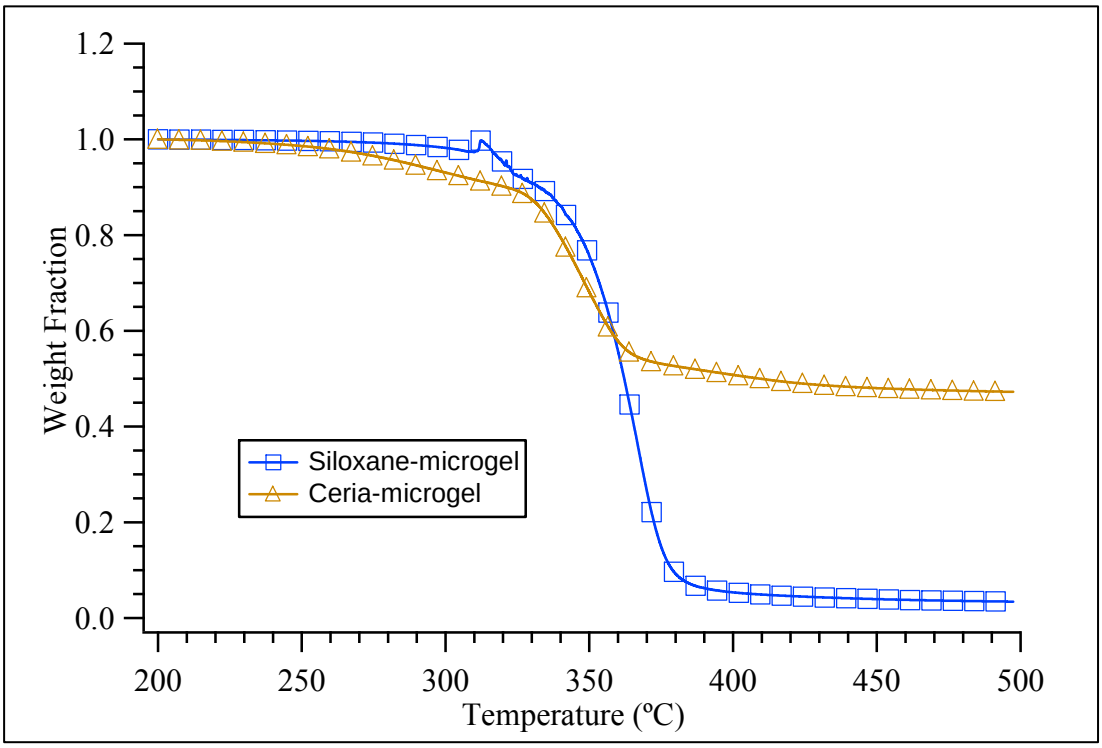

Figure 3.17: TGA analysis of IP-hybrid microgels (blue) and the ceria (IP) microgel microcomposites (orange).

CHAPTER 4: SEDIMENTATION BEHAVIOR OF TITANIA-MICROGEL COMPOSITE PARTICLES

4.1. Background: Sedimenting Systems

Monitoring sedimentation of suspensions and measuring fall velocities of particles is of practical significance in areas such as marine geology, coastal and ocean science, hydraulic engineering and solid–liquid separation technology[64-68]. Also, the hydrodynamics of particle settling is a subject of considerable scientific interest as is evident from the range of literature that stretches from the pioneering studies of Stokes to more sophisticated theories and simulations that have emerged in recent years[69-74]. However, many aspects of settling behavior remain to be completely understood. This is especially evident in complex systems such as highly concentrated suspensions, solutions of polydisperse materials, aggregating and flocculating dispersions, and natural sediments under turbulent flow conditions.

In applications involving microcomposites, the phenomenon of sedimentation is significant in the manufacturing process, product homogeneity, and material application. Within the past two decades there has been an increasing focus on microcomposites containing polymeric and inorganic units for use in medicine, paint, and specialty chemical industries[37, 75, 76]. For instance, zinc oxide particles coated with fluoropolymers are an important constituent of cosmetic foundation creams[37]. In these applications,

sedimentation of the particles can lead to undesirable results. For example, non-uniform formulations in the case of cosmetics are costly errors that occur due to the sedimentation of particles. In the specific case of titania-microgel particles that have been investigated in this dissertation for applications such as photocatalytic remediation of wastewater streams, sedimentation is beneficial as it has the potential for facilitating the recovery of the clean water and nanometer sized TiO_2.

Optical turbidity is used to monitor particle concentration at a fixed height in a settling column during the sedimentation and a simple analytical model can be used to describe the sedimentation behavior in terms of the distribution of settling velocities. Figure 4.1 shows (titania-microgel) microcomposites that were used for the sedimentation studies. The loading of the titania within the microgel can be easily manipulated as shown in figure 4.1. However, first both the technique and the model needed to be validated by using solid, impermeable silica spheres whose sedimentation behavior follows the well established Stokes law. Additionally, the settling behavior of the silica spheres provides a comparison to the sedimentation behavior of the highly porous, titania-microgel particles. Both, the settling of the titania-microgels and the silica spheres are measured under dilute conditions (particle volume fraction < 0.01) to ensure that hindered settling does not play a large role. Samples with different TiO_2 loading are examined to demonstrate the increase in settling velocity as the effective density of the particle increases. Additionally, the sedimentation of both the titania-microgels and freely suspended titania were studied at two different pH values. Since the microgel, and thereby the microcomposites, are thermally responsive materials, the influence of temperature on the sedimentation rate was also examined. The results presented here

demonstrate that in addition to the general usefulness of the sedimentation of titania-microgel particles for remediation purposes, these particles can provide a suitable experimental system to gain insights into sedimentation behavior of complex systems such as permeable particles and flocs of fine particles held by organic matter.

4.2. Description of Experimental Apparatus

The titania-microgel samples discussed here are designated C10, C25, C50, and C75 to indicate titania mass fraction of 10%, 25%, 50%, and 75%, respectively. The settling features of the microcomposites were obtained using a turbidometer (model DRT 1000, HF instruments). The intensity of light scattered at 90º to the incident beam was recorded as a voltage signal as a function of time. Figure 4.2 shows a schematic of the arrangement where the top edge of the aperture was at 3.9cm (h_1) from the sample meniscus and the bottom edge at 5.0cm (h_2). This was the area from which the scattered light intensity was measured. The sampling cylindrical tubes were 12mm×75mm and closed at the top to prevent water loss from evaporation. Suspensions of the titania-microgels were prepared by diluting a concentrated stock solution with DI water to total volume of 5cm^3 and mass concentration such that, C_s =0.5 mg/cm^3. The temperature of the sample was maintained by circulating water through the apparatus using a water bath. A typical experiment consisted of first equilibrating the metallic sample holder at a given temperature for ~30min. The sample tube containing the suspension was placed in the holder for 10–15min, which was determined to be an adequate amount of time for the sample to reach the required temperature. At this point a sedimentation run was conducted by taking the cylindrical glass sample tube out, inverting it a few times to

create a uniform suspension and then placing it quickly back in the holder for data acquisition. Using an acquisition program written in HP-VEE®, 1000 points were acquired at an A/D sampling frequency of 1 kHz and the mean was recorded as a function of time. For the rapid settling (heavily loaded) titania-microgels, each data point was recorded every 5s. To improve the signal-noise ratio for each sample, typically five runs were performed and the measurements at corresponding times were averaged. For the titania-microgels that settled in less than a few hundred seconds, the initial measurements contain some degree of settling during the 2–3s taken for placing the sample tube back in the holder and the decay of any bulk convection effects from the shaking. In the measurements done at 15ºC, the outside of the tube formed a thin condensate layer that had to be wiped prior to each run to minimize multiple scattering effects.

For comparison and calibration purposes, sedimentation was also performed at 25°C with two types of silica spheres. One type was purchased from Bangs Laboratories (Indiana) with an average diameter of 3.21μm. The manufacturer specified a standard deviation in size of 0.35μm. A second, finer silica particle was synthesized (courtesy: Dr. J-Y Shim) via the sol–gel hydrolysis of tetraethylorthosilicate that produced silica particles with a nominal diameter of 0.45μm and a standard deviation of ±0.03μm determined by TEM imaging.

4.3. Analytical Model for Sedimentation Using Turbidometry

Optical techniques that are derived from the scattering of light by particulate matter in suspensions have formed the basis of simple yet useful measurements. Turbidity has been used to examine phenomena such as the flocculation of yeast and

other microorganisms, sedimentation of fine particles (sand grains, powders), and settling of sludges[77-79]. Using well-established theory of photo-sedimentation, the attenuation (I_t/I_o) in the intensity of light following the transmission through a suspension of monodisperse, spherical particles can be shown to be:

$$\frac{I_t}{I_o} = \exp\left(-\frac{\pi}{4} LK(D_P) N_P D_P^{\,2}\right) \qquad \text{Equation 4.1}$$

where D_p is the particle diameter, $K(D_p)$ is the extinction co-efficient for the sphere, L being the optical path length, and N_p represents the number of particles per unit volume. It has been shown that $K(D_p)$ reaches a limiting value of 2 for large particles (>2.5 μm) but is a strong function of particle diameter for finer material. For non-absorbing particles that do not vary in size, a simple turbidity parameter (τ) can be used and related to the number concentration as shown below:

$$\tau = \frac{1}{L} \ln\left(\frac{I_o}{I_t}\right) \propto N_P \qquad \text{Equation 4.2}$$

Equation 4.2 indicates that using a normalized turbidity signal can directly provide information on the evolution of particle concentration due to sedimentation. For a uniform, dilute suspension of monodisperse spherical particles that settle with a single settling V_s, it can be expected that the turbidity signal measured through an optical aperture of height $H(=h_2 - h_1)$ should remain constant until the particles reach the aperture

and then decrease linearly until all particles have traversed the aperture. This scenario is graphically described in figure 4.3 with the analytical representation shown below in equation 4.3:

$$\frac{N_P(t,V_s)}{N_o}=\begin{cases}1 & \text{for} \quad t\le\dfrac{h_1}{V_s}\\ 1-\dfrac{V_s}{H}(t-h_1/V_s) & \text{for} \quad \dfrac{h_1}{V_s}<t<\dfrac{h_2}{V_s}\\ 0 & \text{for} \quad t\ge\dfrac{h_2}{V_s}\end{cases} \qquad \text{Equation 4.3}$$

However, in the case of a suspension of the titania-microgels, several classes of particles that have different settling velocities with the same sample are possible. For the titania-microgels and dilute suspensions, equations 4.2 and 4.3 can be extended to analyze the turbidity signal normalized by its value at initial time to obtain:

$$\frac{\tau(t)}{\tau_0}=\sum\left(\frac{N_{pi}(t,V_{si})}{N_{oi}(V_{si})}\right)Y(V_{si}) \qquad \text{Equation 4.4}$$

where $N_{pi}(0, V_{si})$ represents the number of particles in class "i" at initial time that have a settling velocity of V_{si}, $N_{pi}(t, V_{si})$ represents the number of particles in class "i" with a settling velocity of V_{si} at time t, and $Y(V_{si})$ represents the fraction of total particles that are in class "i". Following a common practice in the analysis of light-extinction data, a log-normal distribution of the settling velocities that was fit using the software IGOR

PRO®, from which one can determine the fraction $Y(V_{si})$ at the various setting velocities. The experimental evolution of the turbidity signal in time can be fitted to equation 4.4 with mean and standard deviation of the log-normal distribution as the only adjustable parameters of the fit.

4.4. Results and Discussions

4.4.1. Settling Using Turbidity Measurements: Validation with Silica Spheres

Figure 4.4A shows the turbidity data measured for a suspension of silica spheres. Since the large silica spheres are expected to follow Stokes law, one can calculate the theoretical fall velocity in water (ρ_w, μ_w) using the Stokes equation shown below:

$$V_s = \frac{(\rho_{sp} - \rho_w)g}{18\mu_w} D_P{}^2 \qquad \text{Equation 4.5}$$

where ρ_{sp} is the density of the settling particle. Figure 4.4A shows that the fitting procedure outlined above matches the experimental data. Table 4.1, shows the comparison between the settling velocities of the silica particles (ρ_{sp} = 1.96 g/cm^3), first when calculated by Stokes law, and then when measured using turbidity. The narrow width of the distribution as seen in figure 4.4B indicates that the silica spheres do not have significant polydispersity.

Table 4.1: Comparison of settling velocities.

	Average settling velocity of silica spheres (cm/s)	
	0.45 ± 0.03 μm	3.21 ± 0.35 μm
Stokes Law	1.1×10^{-5}	5.4×10^{-4}
Turbidity	1.3×10^{-5}	5.4×10^{-4}

For the finer silica particles (D_p ~450nm), Stokes law predicts a settling velocity of approximately 1.1×10^{-5}cm/s. This indicates that the change in the turbidity signal should occur extremely slowly. As shown in figure 4.4 this is indeed the case and the settling occurs over a period of days with the normalized signal going to zero in approximately 5days. In this case, due to the extended period of measurements, an automated timer was used to turn the turbidometer on and off at pre-determined intervals. This automation made the measurements more susceptible to drifts in the voltage signal. However, the fit to the data is acceptable and the velocity distribution shown in figure 4.4B is centered at 1.3×10^{-5}cm/s, which is in reasonable agreement with the Stokes law prediction. Using the results with solid silica spheres, it can be safely concluded that the experimental procedure and the analysis of the data constitute a valid approach to study the titania-microgels and other dilute settling particles.

4.4.2. Settling Measurements for Titania-Microgel Composite Particles

Even though the polymeric IP-microgels do not settle in solution, this is not the case for the titania-microgel composites. Figure 4.5A shows the characteristic changes in normalized turbidity with time for a sample C65 (~65wt% titania) at pH 2 indicating that

the microcomposites settle within a few hundred seconds. Figure 4.5A also shows that the freely suspended titania does not sediment at pH 2 but remains well-dispersed as indicated by the constant turbidity signal over several hours. This dispersion of the freely suspended titania can be attributed to the strong electrostatic repulsion that exists between the positively charged titania nanoparticles in acidic solutions. Rapid sedimentation of the titania-microgels produces a favorable gravimetric separation that has significant potential for use in wastewater remediation as it can facilitate the recovery of the titania nanoparticles.

For the C65 sample, the decline in the measured turbidity signal shown in figure 4.5A can transformed to yield a distribution of settling velocities using equation 4.4. This is shown in figure 4.5B, where the microcomposites show a settling velocity distribution centered at ~0.1cm/s for a pH of 2. At this acidic pH, no settling velocity of the freely suspended titania, can be detected over a period of a few days. An increase in pH to 6.5 results in reduced electrostatic repulsion of the free titania nanoparticles that in turns cause the titania to sediment with an average settling velocity centered at 0.001cm/s. The microcomposite particles still show a velocity distribution centered at ~0.1cm/s. Thus, the microcomposite particles settle nearly a hundred times faster than the free titania particles at near neutral solution conditions, which clearly demonstrates the enhancement in the separation and recovery of photocatalyst using these novel titania-microgel particles. The bottom panel in figure 4.5B shows that when the pH of the solution is strongly basic (~10.5), the settling velocity obtained from a solution of microcomposite particles is almost identical to that of the freely suspended titania. The turbidity signal is indicative of the release of titania nanoparticles from the IP-microgels at basic conditions, which

was readily observable. The release of TiO_2 nanoparticles at a pH of 10.5 can be attributed to the electrostatic repulsion originating from the negatively charged titania and deprotonated carboxylic acid groups of PAAc.

Even though the IP-microgel and the TiO_2 nanoparticles (under acidic conditions) do not settle when present as separate entities, the turbidity from a solution of the titania-microgel particles at 25ºC decreases with time, which is clear evidence of the rapid settling of these microcomposites. This can be attributed to the change in effective density of the titania-microgels and the highly porous nature of the fractal microcomposites. The density of the microcomposite particle (ρ_p) in the dry state can be calculated as:

$$\rho_p(f) = \frac{\rho_{pol}\rho_{TiO2}}{(1-f)(\rho_{TiO2}) + (f)(\rho_{TiO2})} \qquad \text{Equation 4.6}$$

where ρ_{TiO2} is the density of titania (~4.16 g/cm^3), f is the mass fraction of the titania per particle, and ρ_{pol} is the density of the dried polymer (~1.07 g/mL[80]). Equation 4.6 suggests that as the fraction of titania changes from 0.1 (sample C10) to 0.75 (sample C75), the density of a dry microcomposite particle will more than double from 1.16 g/cm^3 to 2.42 g/cm^3.

The rate of settling of the titania-microgels increases with the loading of TiO_2 within the polymer as shown in figure 4.6A. The higher the TiO_2 content, the faster the microcomposite particles settle. The normalized turbidity value drops by approximately 95% within a period of 100 s for the sample C75 and within 2200 s for sample C10. The

settling curves in figure 4.6A can be fit to the log-normal distribution described above to provide a distribution of settling velocities for the four different microcomposite samples. These are shown in figure 4.6B. Sample C10 is found to have slightly higher distribution in velocities than the samples with a higher mass fraction of titania. This is consistent with the TEM images in previous study[81] that clearly show less uniform loading of TiO_2 for sample C10.

The turbidity results shown in figure 4.5 and 4.6 correspond to dilute solution conditions, which minimizes hindered settling. The number concentration (N_p) of the titania-microgel particles in solution can be estimated using the balance:

$$N_p = \frac{N_{Avo} C_S}{M_{pol}/(1-f)} \qquad \text{Equation 4.7}$$

where M_{pol} is the molar mass of the microgel in g/mol and N_{Avo} is Avogadro number. In a recent study[82] on the structure of PNIPAM microgels, Saunders used small angle neutron scattering (SANS) to estimate the molar mass of a microgel particle to be 6×10^9g/mol. The volume fraction of the titania-microgel particles in solution can now be described as:

$$\phi = N_P \frac{\pi}{6} D_P{}^3(T) = \frac{N_{Avo} C_S (1-f)}{M_{pol}} \frac{\pi}{6} D_P{}^3(T) \qquad \text{Equation 4.8}$$

where the diameter of the particle $D_p(T)$ is a function of the temperature. Equation 4.8 can be used to estimate the upper bound of the volume fraction (ϕ) using $D_p(T)$ to equal

the swollen particle size of 0.75 μm, f as 10%, and C_s =0.5 mg/cm^3. This yields an upper bound volume fraction of the particles in the settling experiments to be approximately 0.01. In comparison, the theoretical limit for the volume fraction in the dilute region has been estimated as 0.03 by Batchelor and Wen[83] while Davis and Birdsell[78] have shown experimentally that ϕ~0.08 is acceptable for dilute regime behavior. Hence, the dilute condition requirement of the experiments has been met. Thus, the settling velocity is negligibly hindered by water-currents caused from displacement of the fluid by other settling particles. It should also be noted that the small refractive index contrast of the porous microcomposites relative to water, reduces the likelihood that the optical signals are affected by multiple scattering.

4.4.3. Semi-Empirical Model Describing Sedimentation of the Microcomposites

The most significant observation from figure 4.6 is that the time it takes for all the particles to settle is significantly faster than the solid, impenetrable silica spheres and this time decreases with an increase in titania loading. From the experimental data in figure 4.6, it can be quickly concluded that Stokes law is not suitable for predicting the settling behavior of these titania-microgel particles. As an alternative to Stokes law, one can draw on literature studies on settling of porous spheres and flocs since the structure of the microcomposites is somewhat analogous to other fractal systems found in nature[84-89].

This rather large literature database, which dates back over a century, includes both empirical and theoretical relationships, but no single equation or analysis exists that is universally accepted. All these studies agree that the drag co-efficient of a porous sphere should be smaller than the drag co-efficient of a solid sphere. Thus, this leads to

the conclusion that a permeable particle settles faster. This inference is qualitatively consistent with the results in figure 4.6.

For the settling behavior of titania-microgel particles, two factors appear to play an important role. First, each microcomposite particle is a permeable particle with a typical size that corresponds to that of the cross-linked IP-microgel. This is clearly shown in the TEM images in chapter 3 for the C10, C25, and C75 samples. The second factor that influences the settling behavior arises from aggregation of the porous microcomposite particles into larger-size flocs. These flocs are quite delicate with a tendency to break apart easily under agitation. In order to visualize the structure of the flocs using TEM, the sample was prepared by dipping the carbon coated TEM grid in a dilute solution of the microcomposites followed by drying. Based on the TEM results in figure 4.7, it is shown that the characteristic size (L_f) of the flocs should be 10–100μm. Additionally, since each titania-microgel particle is highly porous, the flocs of the titania-microgel particles tend to be very permeable.

The images in figure 4.7 show that the interpretation of the settling experiments within the context of a purely theoretical model is difficult due to the effect of permeability of each microcomposite particle and their aggregates that has to be accounted for in the hydrodynamic drag resistance during settling. Moreover, any fractal-like aggregation of the microcomposite particles introduces additional complexity. Significant departures between theoretical models and settling of fractal aggregates have been found in past studies[90]. It has been speculated that the discrepancies arise from factors such as improper accounting of non-homogeneous distribution of permeability, an underestimation of the permeability of aggregates, and effects such as particle clusters

sheltering each other from the fluid flow. Hence, the goal in the following discussion is to simply assess if the experiments are qualitatively consistent with the theoretical framework available in literature and develop a semi-empirical model to describe the settling microcomposite particles. Past hydrodynamic theories have attempted to account for the decreased drag resistance of permeable spheres by using a correction factor Ω. This correction factor is the ratio of drag resistance for a permeable sphere to the drag resistance for solid sphere of same radius and bulk density[69, 71-74, 85, 86, 88]. Thus, the drag force on a settling porous particle can be written as:

$$F_p = \frac{1}{2}\Omega C_D \rho_w V_s^{\,2} A_f \qquad \text{Equation 4.9}$$

where C_D is the drag co-efficient of an impermeable particle and A_f represents the projected area experiencing the drag force. Under creeping flow conditions, the Reynolds's number is very small ($N_{Re}<<<1$) such that C_D can be written as $24/N_{Re}$. Recently, Wu and Lee[91, 92] have used numerical modeling of flow through porous particles and have demonstrated that for a highly porous, spherical or non-spherical particle, a Stokes-law like correlation can be used for C_D beyond the creeping flow region. They have expressed the drag force as follows:

$$F_p = \frac{1}{2}\frac{\lambda}{N_{Re}} \rho_w V_s^{\,2} A_f \qquad \text{Equation 4.10}$$

where λ is a parameter that depends on only the characteristic size and permeability of the particle. Wu and Lee show that equation 4.10 is applicable to highly porous particles for $N_{Re}<40$ and that this accounts for the successful use of $C_D = \lambda/N_{Re}$ by several different experimental studies in interpreting results on settling of porous particles and flocs. Using a conventional force balance for the microcomposite particles as follows:

$$\frac{1}{2}\frac{\lambda}{N_{Re}}\rho_w V_s^{\,2} A_f = N_{pf} V_{sp} (\rho_{sp} - \rho_w) g \qquad \text{Equation 4.11}$$

where ρ_{sp} is the density of one porous microcomposite particle with its included water, V_{sp} represents the volume of each microcomposite particle, and N_{pf} is the number of particles in the floc. Many different approaches exist for relating N_{pf} and A_f in aggregated systems using concepts such as fractal dimension, shape factor, and particle interactions. One of these approaches yields:

$$A_f = \frac{\pi}{4} L_f^{\,2} \qquad \text{Equation 4.12}$$

$$V_{sp} = \frac{\pi}{6} D_p^{\,3} \qquad \text{Equation 4.13}$$

$$N_{pf} = \left(\frac{L_f}{D_p}\right)^{\alpha} \qquad \text{Equation 4.14}$$

where α is defined as the fractal dimension of the flocs. Using a volume and mass balance, the density difference of single microcomposite particle can be related in terms of its porosity, ε, such that:

$$(\rho_{sp} - \rho_w) = (1-\varepsilon)\{\rho_p(f) - \rho_w\} \qquad \text{Equation 4.15}$$

where $\rho_p(f)$ is given by equation 4.6. Combining equations 4.11–4.14 gives:

$$V_s = \frac{(1-\varepsilon)}{\lambda}\left(\frac{L_f}{D_p}\right)^{\alpha} \frac{{D_p}^3}{L_f}\frac{4g}{3\mu_w}\left(\rho_p(f) - \rho_w\right) \qquad \text{Equation 4.16}$$

In equation 4.16, the first ratio indicates that even though the porous particle experiences an increase in settling velocity from reduction in drag resistance, this increase is moderated by an increase in porosity. It should be noted that equation 4.16 reduces to the Stokes relation (equation 4.5) for the case of a single, solid particle (ε=0, $L_f = D_p$, λ = 24, and $\rho_p(f) = \rho_{sp}$). Now, for a microgel particle alone, the porosity can be related to the particle diameter by the relation:

$$1-\varepsilon = \left(\frac{6}{\pi {D_P}^3(T)}\right)\left(\frac{M_{pol}}{\rho_{pol} N_{Avo}}\right) \qquad \text{Equation 4.17}$$

Applying equation 4.17 to the microgel in a collapsed state and setting D_p equal to D_{mc} (0.33μm) allows us to estimate the minimum porosity as 0.51. This is consistent with the

SANS and DLS data from the study by Saunders[82] that reveals a significant amount of water is retained by the outer regions of a microgel particle even above the volume phase transition temperature. However, when the microgel is swollen at 20–25ºC, the value of D_p is approximately 0.75μm and this results in a maximum porosity close to 0.96. The high porosity indicates that the microgel particles have a high void fraction as expected. For a microgel-titania particle, the volume fraction of solids in a particle needs to account for both the polymer and the titania nanoparticles. In this case, equation 4.17 can be modified to yield:

$$1-\varepsilon = \left(\frac{6}{\pi D_p{}^3(T)}\right)\left(\frac{M_{pol}}{\rho_{pol} N_{Avo}}\right)\left(1+\frac{f}{1-f}\left(\frac{\rho_{pol}}{\rho_{TiO2}}\right)\right) \qquad \text{Equation 4.18}$$

where the latter term corrects for the volume of titania nanoparticles. Application of equation 4.16 at 25ºC shows that the value of ε ranges from 0.925 for C75, 0.947 for C50, 0.954 for C25, and 0.957 for C10. Comparing this with the porosity of 0.96 for the microgel with no titania, clearly indicates that the titania nanoparticles contribute only slightly to solids volume fraction and their principal impact is on the effective density of the microcomposite particle. Combining equations 4.16 and 4.18 yields the final semi-empirical relation for the functional dependence of the settling velocity on the mass fraction of titania:

$$V_S(f) = K\left(1+\frac{f}{1-f}\left(\frac{\rho_{pol}}{\rho_{TiO2}}\right)\right)\left(\frac{\rho_{TiO2}\rho_{pol}}{(1-f)\rho_{TiO2}+(f)(\rho_{pol})}-\rho_w\right) = K\,\Psi(f) \qquad \text{Equation 4.19}$$

where

$$K = \frac{1}{\lambda}\left(\frac{L_f}{D_p}\right)^{\alpha} \frac{1}{L_f}\frac{8g}{\pi\mu_w}\left(\frac{M_{pol}}{\rho_{pol}N_{Avo}}\right) \qquad \text{Equation 4.20}$$

Using known values for densities of the polymer, titania, and water, one can fit the mean settling velocities from the distributions shown in figure 4.6B using equation 4.19. Figure 4.8A shows that equation 4.19 captures the trend in mean settling velocity of the different titania-microgel particles with a value of K= 0.034 $cm^4g^{-1}s^{-1}$. The value of K obtained from the fit to experimental data can be compared to the prediction of equation 4.20. However, a pre-requisite for this prediction relies on an accurate estimation of the internal permeability, κ. Several theoretical relations have been attempted to estimate the permeability κ of a single porous sphere and/or their aggregates. These include early models such as the Carmen–Kozeny permeability model, Darcy's law and Brinkman's extension of Darcy's law, and as well as more recent approaches that focus on detailed consideration of internal structure of porous aggregates[69-71, 73, 74, 85, 86, 88, 93]. Happel's model[70] has proven to be extremely useful in that it takes into account the internal flows for aggregates of fine particles. Mathematically, this can be represented as:

$$\kappa = \left(\frac{a^2}{(1-\varepsilon)}\right)\left(3 - \frac{9}{2}(1-\varepsilon)^{1/3} + \frac{9}{2}(1-\varepsilon)^{5/3} - 3(1-\varepsilon)^2\right)\left(\frac{1}{\left(3+2(1-\varepsilon)^{5/3}\right)}\right) \qquad \text{Equation 4.21}$$

Using porosity of ε=0.96 and with 'a' being the size of the titania clusters (~100 nm), the predicted permeability for a microcomposite particle is $\kappa \sim 10^{-9}$ cm^2. The κ value can now be used to estimate the Brinkman[69] parameter such that ($\beta = D_p/2\nu\kappa$; β~1.2). This is in good agreement with other experimental studies. Assuming this for β and using the correlation by developed by Wu and Lee for flow through porous particles:

$$\lambda(\beta) = 6\beta - 2 \qquad (0.5 \le \beta \le 1.58) \qquad \text{Equation 4.22}$$

Now, K can be estimated by equation 4.20. Figure 4.8B shows the predicted value of K for three values of α between 2.5 and 3 and floc sizes from 10μm to 100μm. The predicted values lie in the neighborhood of K calculated by fitting the experimentally determined settling. This analysis also suggests that when the fractal dimension is less than 3 the value of K is relatively insensitive to the floc size and that the titania loading will play a large role in the variation of settling velocity.

One of the interesting aspects of the titania-microgels is that these particles are temperature responsive. Qualitatively, as temperature is increased from 15ºC towards 35ºC the settling of the particles becomes faster. Changes in the sedimentation behavior of the microcomposite particles with temperature can be attributed to the temperature responsive nature of the microgels and changes in the fluid viscosity with temperature. Further details of this behavior can be found in the master thesis (USF) of Reshma Harrinauth[94].

4.5. Summary

The results presented here demonstrate the general usefulness of settling as a simple characterization of organic–inorganic microcomposites and other sedimenting systems of an intricate nature. The sedimentation behavior of titania-microgels and freely suspended titania were studied at a range of pH values and titania loadings. The titania-microgels showed rapid sedimentation in aqueous dispersions, nearly 100 times faster than the freely suspended titania. It was found that the settling time decreased as the content TiO_2 increased within the particles. A semi-empirical model was developed that related the settling behavior in terms of the changes in the effective density. The settling behavior of these microcomposites provides not only a simple probe of particles characteristics but also insight into fundamental issues regarding settling of porous spheres, flocs of inorganic particles within organic material, and sedimentation phenomena in marine environments. Lastly, the microcomposites characterized in this dissertation are promising candidates for applications such as wastewater remediation where uses of nanoparticles of TiO_2 are advantageous for photocatalysis but separation is relatively difficult. In this context, the gravity settling behavior of the microcomposites can be a promising characteristic in wastewater remediation as it allows for an easy recovery mechanism.

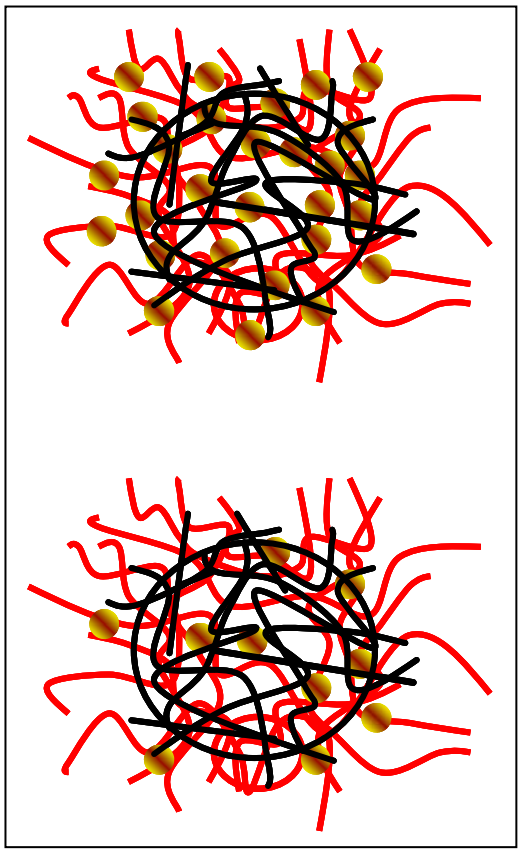

Figure 4.1: Depiction representing the titania-microgels that were used for the sedimentation studies where: (top) microcomposite particle heavily loaded with titania and (bottom) microcomposite particle sparsely loaded with titania.

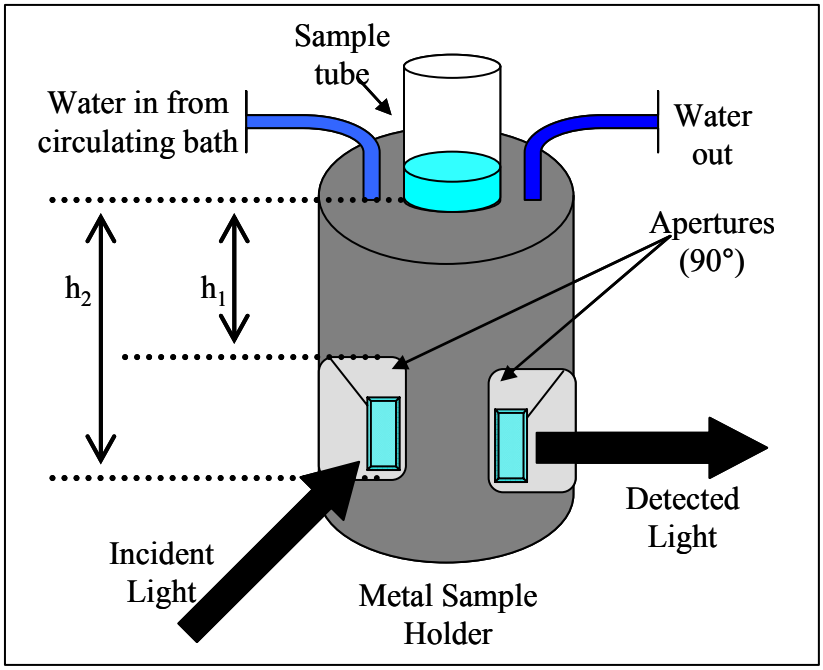

Figure 4.2: Schematic of the arrangement for optical measurement of settling behavior.

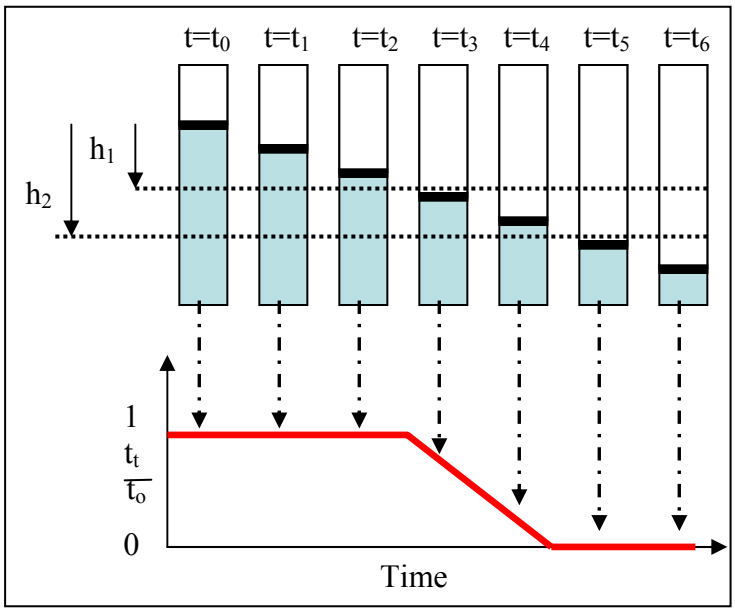

Figure 4.3: Schematic of the idealized settling of a uniform, monodisperse suspension and the normalized turbidity signal that will be expected as a function of time. The measurement window is indicated between the two horizontal dashed lines.

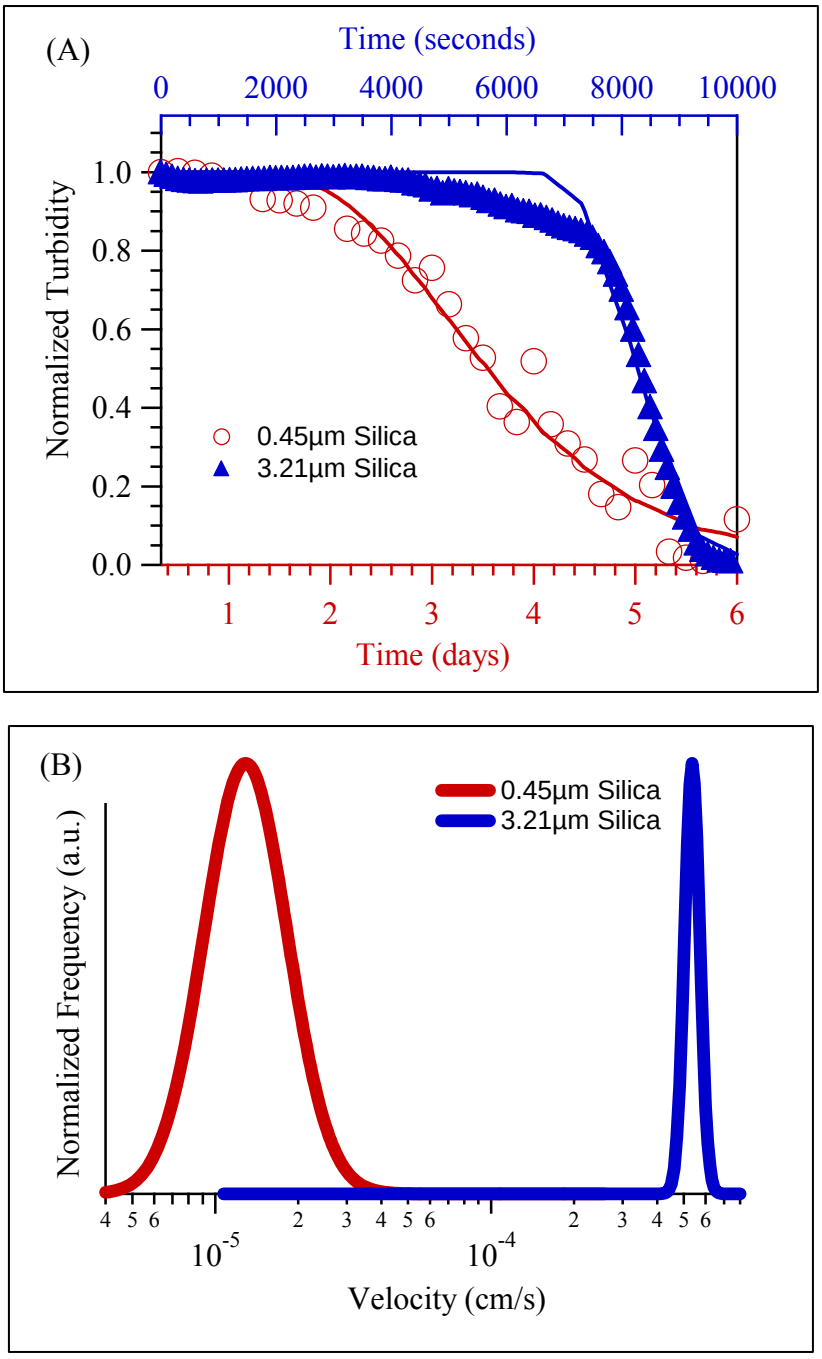

Figure 4.4: From turbidity: (A) Evolution in the normalized turbidity signal during sedimentation of both large silica spheres (D=3.21µm) and small silica spheres (D=420nm) and (B) distribution of settling velocities corresponding to the fit shown in (A). The symbols are the experimental data and the solid line is the fitted curve.

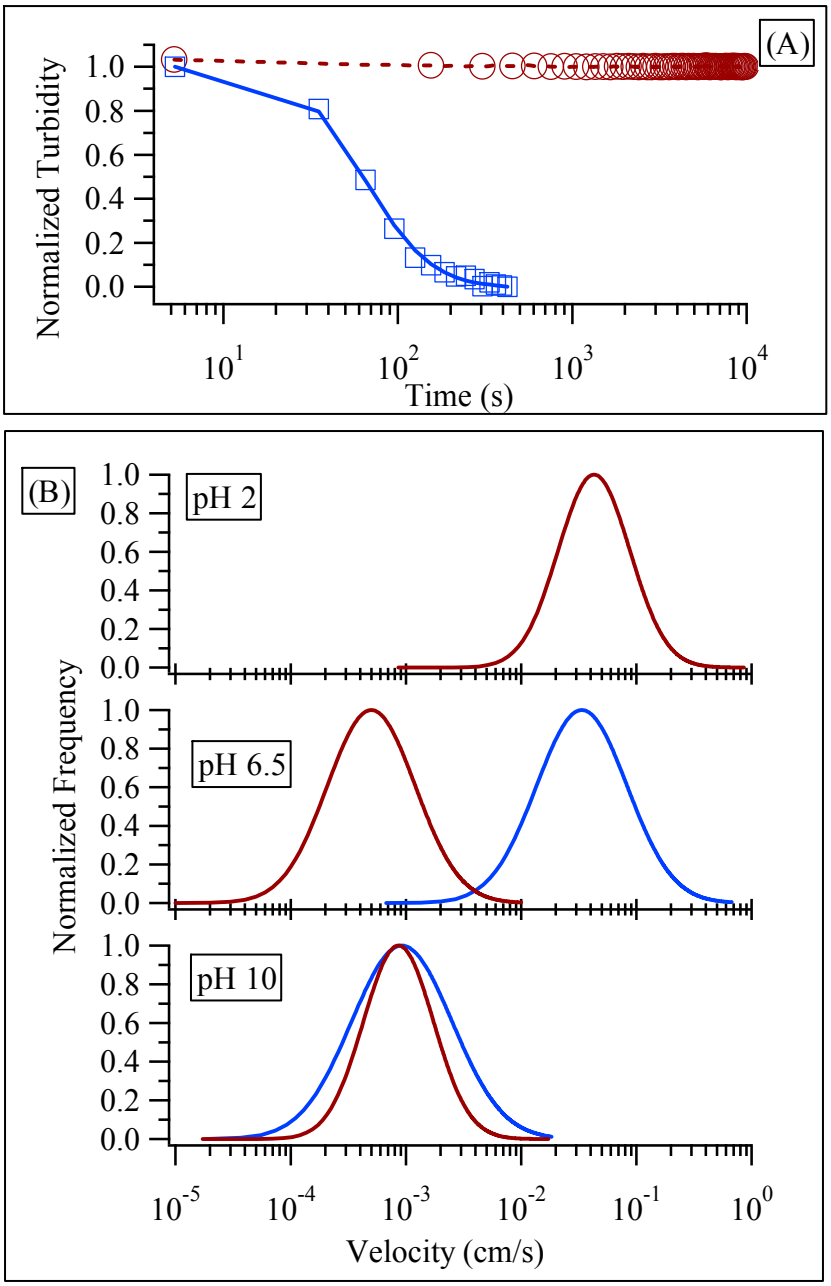

Figure 4.5: (A) Changes in turbidity due to sedimentation of the microcomposites (blue) and TiO_2 nanoparticles (red) at a pH of 2 (squares) and (B) distribution of settling velocity of freely suspended titania and the microcomposites at three different pH values. The solid line is the fit to a mathematical model.

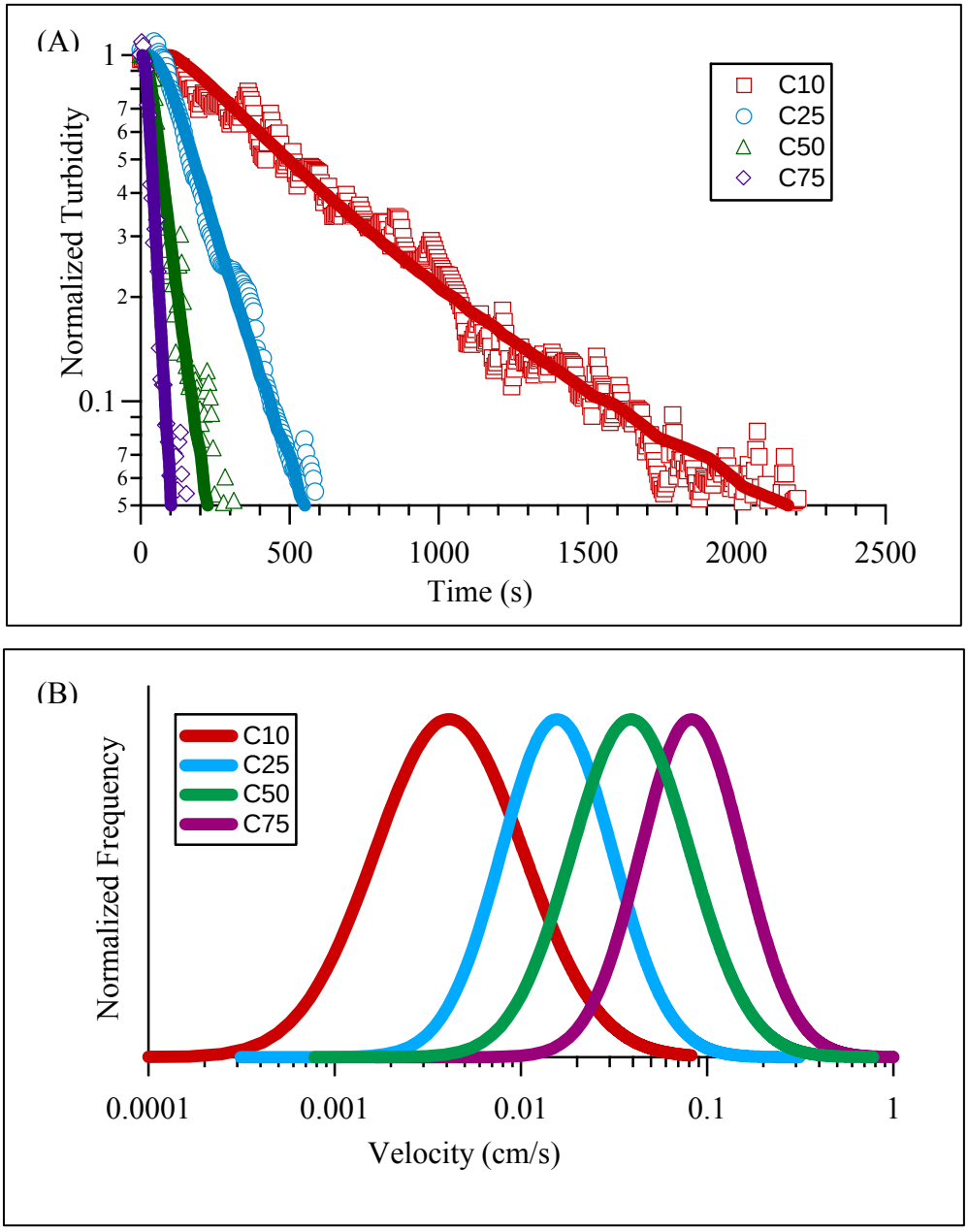

Figure 4.6: (A) Settling behavior of microcomposites with different TiO_2 loading measured using a turbidometer at 25ºC and (B) distribution of settling velocities corresponding to the fits in (A). The lines are the results of the fitting procedure and sparse markers have been used for clarity with one marker for every 10 points.

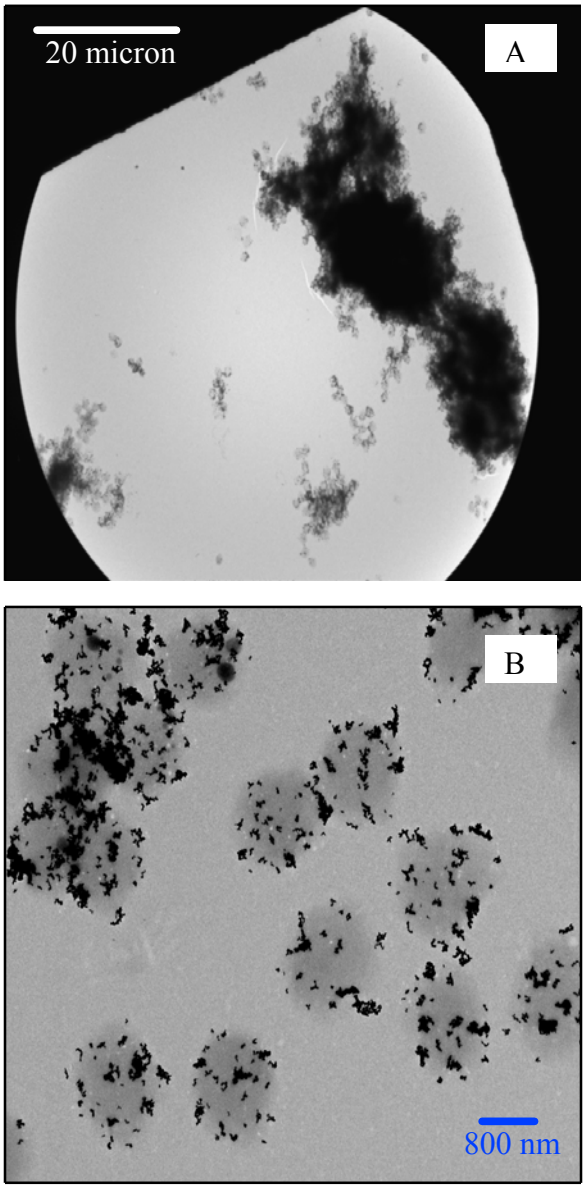

Figure 4.7: TEM images of the C50 sample showing (A) a large floc on the TEM grid and (B) several single microcomposite particles with a small aggregate.

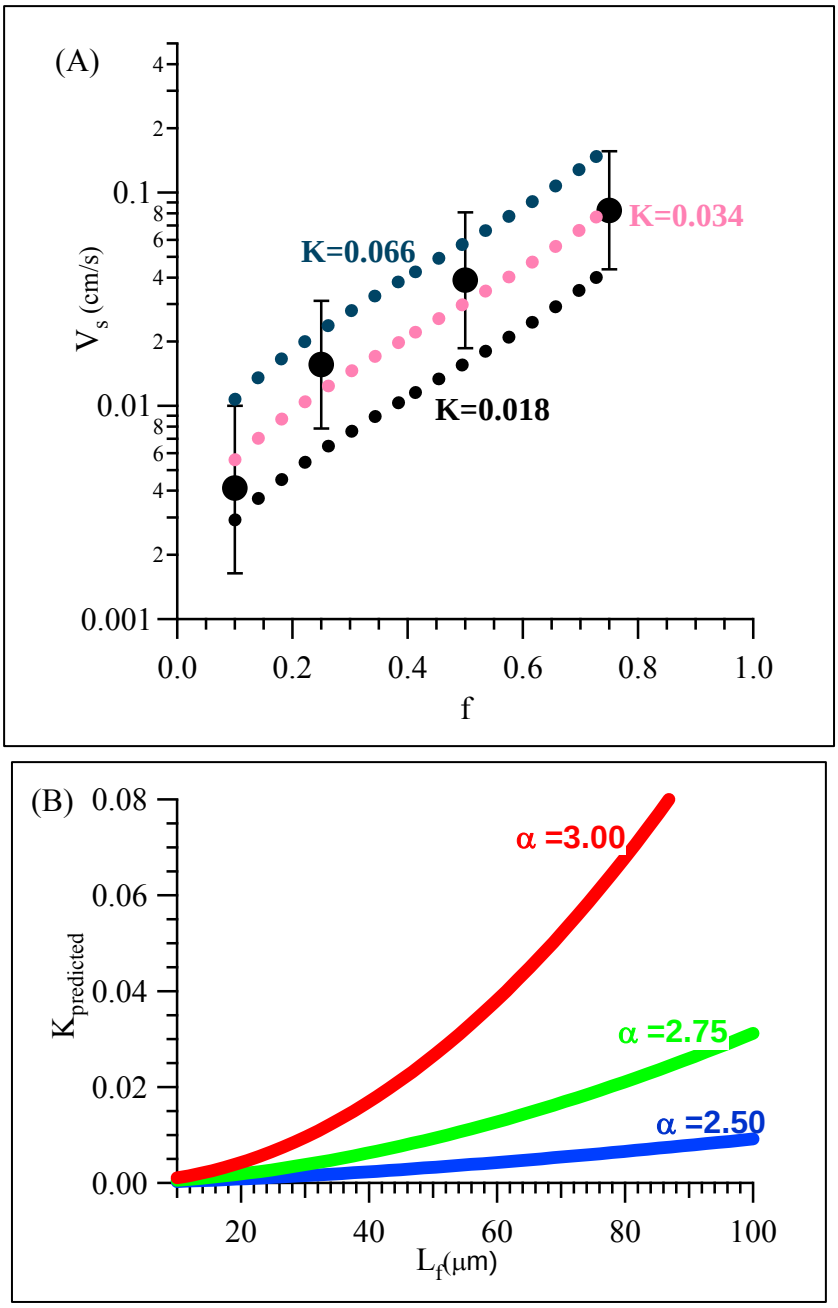

Figure 4.8: (A) Mean settling velocity for each sample from figure 4.6B plotted as a function of the mass fraction of titania. The deviations are obtained from the half-widths of the distributions in figure 4.5B. The pink dotted line is a fit using equation 4.19 in the text with a value of K= 0.034 while the dashed lines represent fits using K= 0.066 (top) and K= 0.018 (bottom). (B) Predicted value of K (equation 4.20) for a range of α and Lf.

CHAPTER 5: PHOTOCATALYTIC DEGRADATION OF METHYL ORANGE USING TITANIA-MICROGELS

5.1. Introduction

The titania-microgel particles synthesized in this research have the potential for use in photocatalytic degradation of organic contaminants in industrial settings for wastewater remediation. Depending on the source (household, agriculture, industry), wastewater can contain a wide variety of both biological and chemical contaminants. Typically, wastewater treatment includes many processes such as solids removal, treatment of biodegradable organics, removal of heavy metals, neutralization, and degradation of organics. Advanced oxidative processes using nanoparticles of titania are best suited for remediation of the organic components and typically considered downstream of steps such as solids removal or heavy metal removal.

Since the results presented within this doctoral research clearly demonstrate the enhancement in separation that occurs when using the titania-microgel composites versus freely suspended nanoparticles of titania, the photocatalytic performance of the microcomposites is of great interest. Therefore, as a first step, this chapter explores the phtodegradation of a simplified system that contains only one model organic contaminant. At this stage, role of other factors such as ionic strength of the solution,

presence of interfering contaminants, and degradation of two or more organics is not studied.

Towards an assessment of the photocatalytic performance of these novel materials, investigation of the photodegradation of a model organic dye, methyl orange (MO) was conducted using both the novel titania-microgels and freely suspended titania. Kinetics of the photodegradation of MO was evaluated using UV-Vis spectroscopy to assay the MO concentration over various intervals of irradiation. The influence of pH was monitored, as this influences the interplay between the poly(acrylic acid) in the polymer microgels, the titania surface and the methyl orange adsorbate. Degradation of methyl orange using freely suspended titania was also conducted for comparison with the titania-microgel particles. Lastly, the impact of prolonged irradiation on the degradation of the polymeric component of the microcomposites is studied using UV-Vis spectroscopy and the resultant release of titania is characterized by sedimentation studies. The results reported here are critical and necessary inputs for the development of processes that can use the novel titania-microgels in photodegradation of organic contaminants in aqueous streams.

5.2. Experimental Details

Methyl orange was used as a model contaminant to examine the photocatalytic behavior of the synthesized titania-microgels. Aqueous solutions with a concentration of 5ppm MO were evaluated for degradation. Titania-microgels or free TiO_2 nanoparticles were added such that the titania content in the solution was 50, 100, 150 or 200ppm. The pH was adjusted using 0.1M HCL or 0.1M NaOH when needed, and degradation kinetics

were evaluated at a pH of 2 (±0.1) and 6.5 (±0.2). Photocatalysis was conducted under illumination using two commercially available 15W Philips F15T8 black-light fluorescent bulbs (model 392233) that have spectral energy distribution centered at 352nm. The intensity of the radiation reaching the solution surface (3.5mJ/cm^2) was detected via a Chromaline UV Minder radiometer (UVM226) connected to a remote probe (UVM226S). The apparatus was kept inside a vacuum hood such that a slight negative air pressure prevented any upsurge of CO_2 or N_2 above the reaction vessel that could occur due to the decomposition of the organics. Other researchers have shown that much of the irradiation occurred within a few centimeters of the liquid surface (even at very low catalyst loadings)[95, 96]. Consequently, the reaction was conducted under vigorous agitation to ensure uniform distribution throughout the reacting medium and prevent sedimentation of the C65 particles. Control experiments were performed by conducting UV irradiation without the addition of any photocatalyst in the MO solution. Negligible decolorization (<1%) was observed confirming that the degradation of MO predominately occurs by photocatalysis using titania rather than photolysis. Dark adsorption was conducted for at least three hours before irradiation to allow for the adsorption of MO onto the TiO_2 surface. Aliquots of 1.5mL of the suspension were collected at regular intervals during the degradation experiments. These samples were then centrifuged (10000g, 30mins) to completely remove any particles, and the peak absorbance was analyzed using a V-530 UV-Vis spectrophotometer (Jasco).

5.3. Chemical Kinetics and Pathways Governing Photocatalytic Degradation

Photocatalysis can be typically divided into three stages: (A) production of electron/hole (e-/h+) pairs by irradiation with light having photonic energy greater or equal to the existing band gap (~3.2eV for titania), (B) migration of the charge carriers from the crystalline interior to the surface, and (C) redox interactions at the particle surface between the contaminant and the free e-/h+ pairs that survived the migration[15].

Titania has shown the best photocatalytic ability, when compared with other available inorganic oxides typically used like ZnO, Al_2O_3 and Fe_2O_3. In particular, mixed phase titania such as Degussa^{TM} P25 (80% anatase and 20% rutile phase) has shown enhanced photocatalytic activity upon illumination compared to single crystalline phases[97, 98]. This enhancement is attributed to the ideal size of the titania nanoparticle, trace amounts of Fe^{3+} dopant (that acts as a charge separator) and the synergistic combination of the anatase and rutile phases that provides prolonged separation of the photogenerated electrons[99]. Equation 5.1 shows the e^-_{CB}-h^+_{VB} pair separation within the conduction and valence bands upon irradiation. It is broadly accepted that hydroxy radicals (OH•) are produced from the direct oxidation of H_2O, OH- ions (bulk solution) or terminal hydroxyl groups (catalyst surface) by photogenerated holes (h^+_{VB}) as shown in equations 5.2 and 5.3[100, 101]. Superoxide radicals often result from the interplay between the photogenerated electrons (e^-_{CB}) and molecular oxygen. The addition of peroxides increase the occurrence of reaction 5.4 and the presence of hydroxyl radicals, thereby increasing the degradation kinetics as widely reported[102-104].

$$TiO_2 + h\upsilon \rightarrow TiO_2 + e^-_{CB} + h^+_{VB} \qquad \text{Equation 5.1}$$

$$h^{+}_{VB} + OH^{-} \rightarrow OH^{\bullet}$$ Equation 5.2

$$h^{+}_{VB} + H_2O \rightarrow OH^{\bullet} + H^{+}$$ Equation 5.3

$$e^{-}_{CB} + O_2 \rightarrow O^{-}_{2}$$ Equation 5.4

Examining the adsorption characteristics of MO onto the TiO_2 surface as a function of pH variations are pertinent to fully understanding the mechanism surrounding the degradation of organic contaminants. Generally the observed pH dependence of the reaction rates of MO decomposition can be understood in terms of the adsorption of both the substrate molecule and hydroxyl ions onto the charged TiO_2 surface as much of the degradation occurs on or near the titania surface rather than in the bulk medium[105, 106]. It is well known, that in the presence of water, the surfaces of the metal or semi-conductor oxides are hydroxylated[107-109]. Depending on the pH, these surface groups may add or abstract protons. The corresponding acid-base equilibria for titania can be written as follows:

$$TiOH + H^{+} \leftrightarrow TiOH^{+}_{2}$$ Equation 5.5

$$TiO^{-} + H^{+} \leftrightarrow TiOH$$ Equation 5.6

Degradation of the MO can be explained in terms of the elementary mechanisms shown in equations 5.7-5.9. It can involve the direct reaction of the dye with photogenerated holes in a process similar to the photo-Kolbe reaction or oxidation through successive attacks by hydroxyl radicals or superoxide species[110]. The hydroxy radical in particular is an extremely strong nonselective oxidant that has shown to lead to the partial or complete oxidation of many organic chemicals[111].

$$OH^{\bullet} + MO \rightarrow \text{colorless product} \qquad \text{Equation 5.7}$$

$$h^{+}_{VB} + MO \rightarrow \text{colorless product} \qquad \text{Equation 5.8}$$

$$O^{-}_{2} + MO \rightarrow \text{colorless product} \qquad \text{Equation 5.9}$$

Termination of active species can also occur by the mechanisms detailed below. Very small particle sizes (~10nm) tend to lead to higher electron-hole recombination (equation 5.10) reducing the photocatalytic activity. However, the optimum size of Degussa™ P25 titania and its efficient electron transfer from the rutile to anatase phase, leads to increased charge separation that causes efficient photocatalytic reaction at the particle surface[98].

$$e^{-}_{CB} + h^{+}_{VB} \rightarrow \text{heat} \qquad \text{Equation 5.10}$$

$$HO_2^{\bullet} + OH^{\bullet} \rightarrow H_2O + O_2$$ Equation 5.11

In this study, both the freely suspended titania and titania-microgels consist of only Degussa™ P25 titania. The degradation products of methyl orange using Degussa™ P25 titania has been studied extensively[112-114] with many of the intermediates during the MO degradation process already identified[115]. Thus, the focus of this research was on the photocatalytic performance of the titania-microgels that could serve as a prototype for the potential optimization of existing advanced oxidative processes.

5.4. Results and Discussion

The TEM images of the titania-microgel (C65) and freely suspended Degussa™ P25® nanoparticles are shown in figure 5.1. The contrast between the freely suspended titania and titania-microgels is evident. The freely suspended titania is randomly displaced throughout the medium with no well defined arrangements, while the C65 particles contain titania that is well localized onto the largely spherical IP-microgels. As described in chapter 4, the titania-microgels showed rapid sedimentation on the time-scale of minutes, which can be useful for gravity separation of these particles.

5.4.1. Photocatalytic Performance of the Titania-Microgel Composites

For photodegradation experiments, the two different pH conditions (2 and 6.5) were chosen because sedimentation studies described in chapter 4 revealed that the titania-microgels released titania nanoparticles under basic conditions due to the

electrostatic repulsion between the negatively charged titania and de-protonated carboxylic acid groups.

As a first step, it was imperative to understand the effect of pH of the MO solution. The initial spectra (at 0min) in figures 5.2 show the UV-Vis absorbance of MO above and below its pKa (~3.8). A significant peak shift is seen from 506nm (pH2) in figure 5.2A to 464nm (pH6.5) in figure 5.2B. The change in structure of MO was induced by the transition from a high to low pH and vice versa. This change in structure arises due to the increased delocalization of lone pair electrons on the azo group[116]. The inset in figure 5.2 best describes this delocalization in the form of canonical structures of MO at acidic pH values. In addition to the peak shift seen in figure 5.2, there is also a 45% increase in the peak height of the MO absorbance when the pH is lowered from 6.5 to 2. It is well known that the absorbance or irradiation by a solution is readily described by the Beer-Lambert law. Since the concentration and absorbance path length are same, it can be deduced that the canonical structures of MO, under acidic conditions, result in a larger molar extinction co-efficient when compared to the negatively charged MO molecule at near neutral conditions.

Figures 5.2A and B also show that the peak absorbance of MO decreases as a function of time. The rate of change of absorbance of MO caused by photodegradation with either the titania-microgels or the freely suspended titania is well described by a mono-exponential curve. This construes that a pseudo-first-order reaction model can be used for describing the kinetic behavior of the photocatalysis. In this study, the MO concentration was held constant at 5ppm. Using a modified Langmuir-Hinshelwood model, the rate of decolorization can be expressed:

$$-\frac{dC}{dt} = r = \frac{kKC}{1+KC}$$ Equation 5.12

Here 'k' refers to the rate constant for the reaction, while 'K' refers to the equilibrium adsorption co-efficient. Due to the initial low concentration of MO (KC<<1), the 'KC' term in the denominator is typically neglected[117, 118]. Integration of the above equation with the initial condition $C=C_0$ at initial time, and defining the apparent rate constant as $k_{app}=kK$ leads to the expected first order reaction equation:

$$\ln\left(\frac{C_0}{C}\right) = k_{app}t$$ Equation 5.13

The apparent rate constant (k_{app}) was obtained directly via regression of the experimentally observed decline in the peak height of MO absorbance (as a function of time). This is shown in figure 5.3, where the fits to the normalized absorbance at regular time intervals using equation 5.13, yields the apparent rate constants for the reaction. In figure 5.3A the apparent rate constants for MO degradation using the titania-microgels over a range of concentrations is depicted at pH2. At a more neutral pH of 6.5, the rate of MO degradation is retarded as seen in figure 5.3B. The control experiment, where MO in solution was irradiated in the absence of titania under similar conditions (pH 6.5, UV=3.5mJ/cm^2), yielded a null rate constant and thereby confirmed that MO degradation was achieved via photocatalysis alone.

In figure 5.4, the fitted rate constants are compared for both the freely suspended titania and the C65 particles in experiments performed with different amount of titania

photocatalyst in the solution. First, examining the rate kinetics of the freely suspended titania shows that increasing the concentration of the titania resulted in a faster decolorization of the MO at both pH values tested. This effect is well documented and attributed to the increased active sites on the titania surface available for MO degradation[119, 120]. Regarding the pH variation the results presented here using freely suspended Degussa™ P25 titania correlate well with that of Kansal and co-workers[121], who also reported faster degradation kinetics under basic and neutral conditions. In general, the degradation of MO is faster at a near neutral pH and slower in an acidic medium. This effect can be explained as follows: at a high pH, both the surface of the titania (ISP ~ 6.5) and the MO are negatively charged. However, the presence of large quantities of hydroxyl ions on the particle surface (as well as in the reaction medium) favors the formation of the oxidizing OH• radicals. Near a neutral pH, even though there is a reduction in the concentration of OH- ions in bulk solution, the electrostatic repulsion between the titania surface (now relatively uncharged) and the MO is reduced, thereby favoring adsorption of the dye and its degradation. Lastly, in an acidic medium the significant reduction in the concentration of the OH- ions leads to a decrease in the rate constant as demonstrated experimentally at pH 2.

A number of significant observations can be made when comparing the photocatalytic performance of the freely suspended titania with the titania-microgels. Under acidic conditions, the photodegradation by the titania-microgels and the free titania show nearly identical rate constants over a range of titania concentrations. In contrast, near a neutral pH the photocatalytic degradation of MO using the titania-microgels has a smaller rate constant and this remains largely unaffected even when the concentration of

titania is increased. A closer look at the structure of the titania-microgels can give some insight into these differences. The PAAc chains that interpenetrate the IP-microgel contain carboxylic acid groups that are mostly deprotonated above pH4 and known to functionalize inorganic oxide surfaces[60, 122, 123]. Near a neutral pH, photocatalytic degradation of MO using the titania-microgels is minimal since the modification of the oxide surface by deprotonated negatively charged carboxyl groups can result in the disruption of the adsorption of negatively charged hydroxyl species onto the titania surface due to electrostatic repulsion. With the number of oxidative species generated by the titania diminished, the photocatalytic oxidation reaction can be expected to be retarded and this is experimentally manifested as a lower reaction rate constant. However, at pH2 the PAAc is protonated and the titania surface within the titania-microgels remains primarily unhindered and available for the photocatalysis. As a result, the photocatalytic performance of both the titania-microgels and the freely suspended titania were comparable. Hence a trade-off exists when using the titania-microgels, in that the photodegradation is slower at near neutral conditions but the settling is nearly a hundred times faster than the free titania particles. Additionally, by a simple change in pH, the rate constant of the titania-microgels can be easily manipulated, with the degradation rate ramped up or down when desired.

Increasing the photocatalyst concentration from 50 to 200 ppm requires increasing the concentration of titania-microgels. At acidic conditions, the concomitant increase in polymer fraction has little influence and the effect from increased titania surface sites dominates, which leads to faster photodegradation. At neutral pH conditions, the increase in the PAAc fraction balances the increase in titania and little change in the reaction rate

constant can be observed. Because the reaction rate constant at neutral pH conditions is already small (~0.005 min^{-1}) when using the microcomposites containing 65wt% content of titania, experiments with titania-microgels possessing less than 65% loading of titania were not pursued as it would further reduce the rate of photodegradation, and the sedimentation of sparsely loaded titania-microgel composites is not as quick.

5.4.2. Impact of Irradiation on the Stability of Polymeric Microgels

Since the photocatalysis with titania gives rise to oxidative species that can degrade the polymer chains, it is to be expected that the titania-microgels will also degrade (via photocatalysis) over time. Consequently, the degradation of the titania-microgels was studied using two separate approaches (in both cases with no MO present in the solution). First, the sedimentation behavior of the C65 titania-microgels after pre-determined periods of UV irradiation was analyzed using turbidometry at the two pH conditions. Since the settling velocity of the microcomposites is a function of the titania loading in the microgels, any release of the titania nanoparticles from the polymer mesh should be expected to lead to reduced settling velocities. The second technique used involved analyzing the scission of the polymer chains via photocatalysis. As the oligomeric segments present in the solution increased, it was measured via UV-Vis spectroscopy. By performing a thorough analysis of these results, useful insights were gained into the process of degradation of the microcomposites.

Figure 5.5A shows the voltage signal during sedimentation of the titania-microgels after various irradiation times at pH 6.5 using the turbidometer. It is evident that little change is observed in the sedimentation behavior even after 4.5 hours of UV

illumination and as expected, most of the particles settled rapidly within 1000 seconds. This suggests that the titania loading within the microgels is largely constant with no significant loss of the nanoparticles occurring during the irradiation window. However, after 6 hours of irradiation, even though settling can be observed by the decrease in turbidity of the solution, the steady upward shift in the residual signal after 1000s indicates that the solution contains a suspended particulate concentration. This is a contribution from the slowly settling titania nanoparticles that have been released and their fraction in the solution is growing with time of irradiation. Figure 5.5B shows that at pH 2, a similar trend is observed with the release of titania being manifested in the sedimentation behavior of the titania-microgels after only 4.5 hours of irradiation. It should be noted that the supernatant liquid remaining after 3 hours of UV irradiation of solutions at both pH 2 and 6.5 was also analyzed for titania using the quantitative spectroscopic technique[81] and no measurable amounts were detected. This supports the interpretation of the results from sedimentation, and the hypothesis that photocatalysis was conducted by the titania localized onto the polymer microgels, rather than released titania nanoparticles. Figure 5.5B shows that after approximately 6-7.5 hours of continuous irradiation at pH 2, most of the titania has been released and no settling is observed since the positively charged titania nanoparticles do not settle.

Figure 5.6 reflects the increase in the oligomeric segments present in the supernatant that is obtained after centrifugation of samples drawn at regular time intervals during UV irradiation of a solution of the titania-microgels alone. Absorption in the UVC region (190-400 nm) is typical of organic moieties of the fragmented polymeric segments that result from the cleavage of the IP-microgels during the photodegradation. Figure 5.6

shows that integrated area of the absorption peak increases with time and becomes fairly constant after several hours of irradiation. The data is again consistent with a physical picture of slow microcomposite degradation that is also governed by the pH conditions of the testing. At a pH 6.5, the measured absorbance reaches a plateau at ~13hrs and at pH 2, the plateau value is reached ~8hrs. Both of these degradation times are consistent with the turbidity results in figures 5.5 that show few changes in settling after 10-12 hours (pH6.5) and 6 hours (pH2). Comparison of the results in figures 5.5 with figure 5.6 also indicates that significant changes in settling only occur at times that correspond to a substantial percentage (~50-60%) of oligomeric absorption.

The integrated areas for oligomeric absorption are shown in figure 5.7. and also support the conclusions drawn form the photodegradation of MO. At a pH 2, the degradation kinetics were much faster for MO and the same is true when the titania-microgels are being degraded as shown by the comparison of sedimentation or the comparison of oligomers in solutions after degradation. The results in figure 5.7 also indicate that the time for the degradation of the titania-microgels is significantly longer than the time required for MO degradation (~3 hrs).

One of the advantages of these novel titania-microgels is their ease of formation. Following the long time degradation of the titania-microgels, the titania nanoparticles are released into the aqueous solution. However, addition of fresh IP-microgels under acidic conditions (pH2) quickly reformed the microcomposites particles with a 65wt% titania loading. Furthermore, photodegradation of the organic dye could be repeated using the reformed titania-microgels. When the photodegradation kinetics of MO using the reformed titania-microgels was compared with the original results of the freshly prepared

titania-microgels (before exposure to UV irradiation), the regression analysis yields the same rate constant for both samples as shown in figure 5.8. Thus, the titania-microgels are excellent candidates for remediation processes that can re-use and recycle the titania photocatalyst efficiently. The results reported in this study demonstrate that the UVA irradiation (~350nm) can be used for the photodegradation of chemical contaminants with the titania-microgels without rapid decomposition of the polymeric matrix and that these novel materials enable large scale separations using gravity thickeners and centrifugal clarifiers.

5.5. Summary

The photodegradation of a methyl orange was investigated using both rapidly settling titania-microgel particles and freely suspended titania. Under acidic conditions, the reaction rate constants were found to be identical while the freely suspended titania showed faster rate kinetics near neutral conditions. However, the rapid sedimentation of the titania-microgels (~100X faster than freely suspended titania) makes them promising candidates for applications such as wastewater remediation where the use of nanoparticles of titania is advantageous for photocatalysis but separation of the nanoparticles is difficult. Even though the cross-linked matrix of the colloidal polymeric particles showed degradation over several hours, the titania that was released due to the microcomposite degradation could be easily re-captured via the addition of fresh polymer IP-microgels. These reformed titania-microgels showed similar photocatalytic behavior as the original titania-microgels that indicated that these materials can be easily

regenerated and the photocatalyst can be recycled without significant aggregation within the reformed microcomposites.

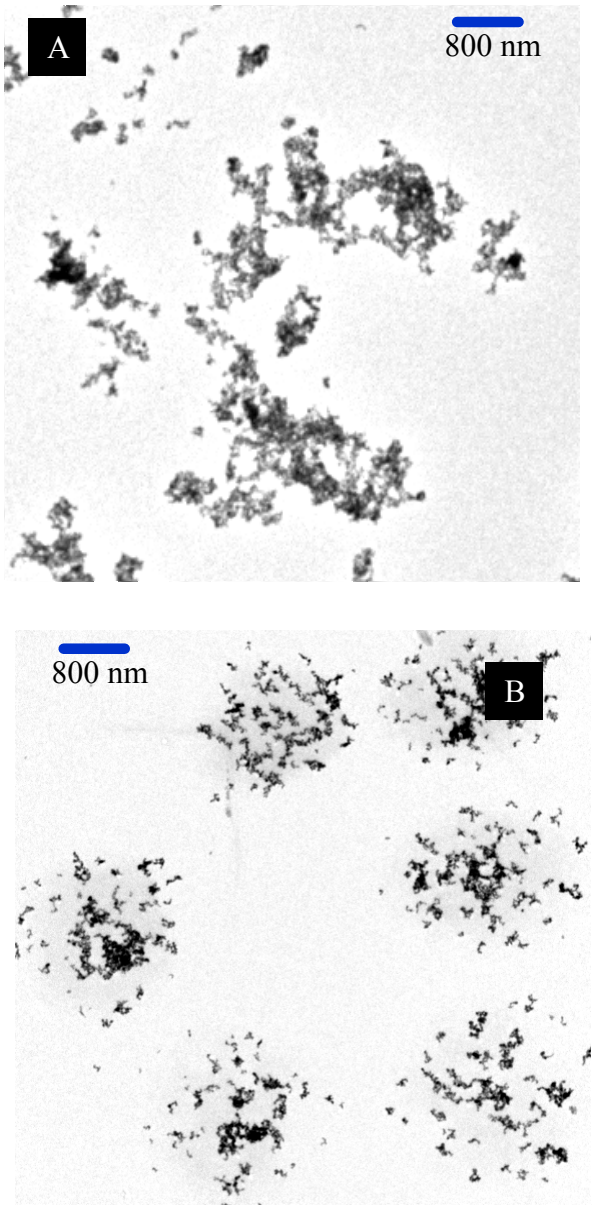

Figure 5.1: TEM images of (A) freely suspended TiO_2 nanoparticles in aqueous media and (B) titania-microgel particles.

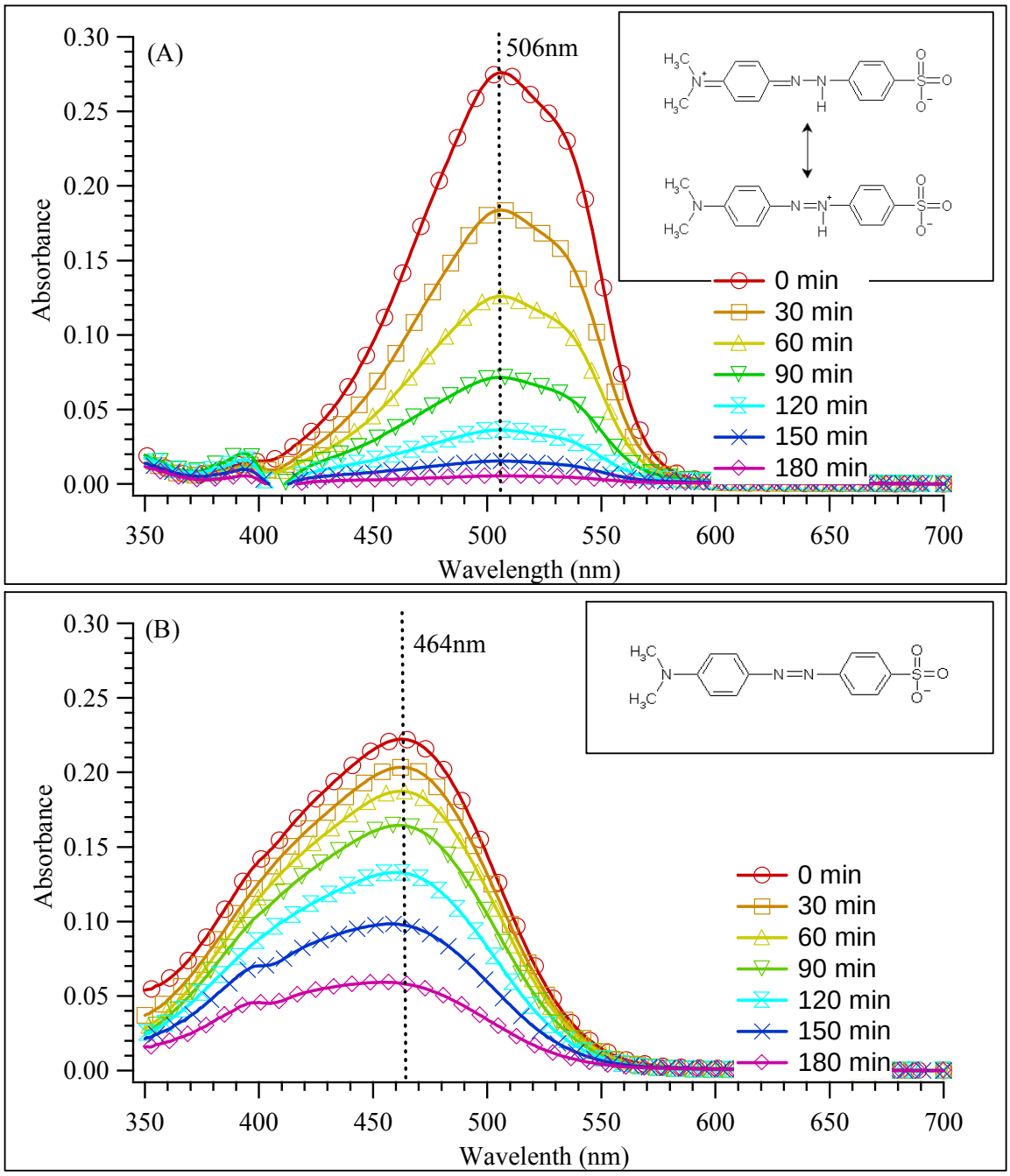

Figure 5.2: (A) Absorbance spectra of MO degradation in solutions containing titania-microgels (200ppm TiO_2) at a pH of 2 and (B) absorbance spectra of MO degradation in solutions containing titania-microgels (200ppm TiO_2) at a pH of 6.5. Insets: canonical structures of MO at the corresponding pH.

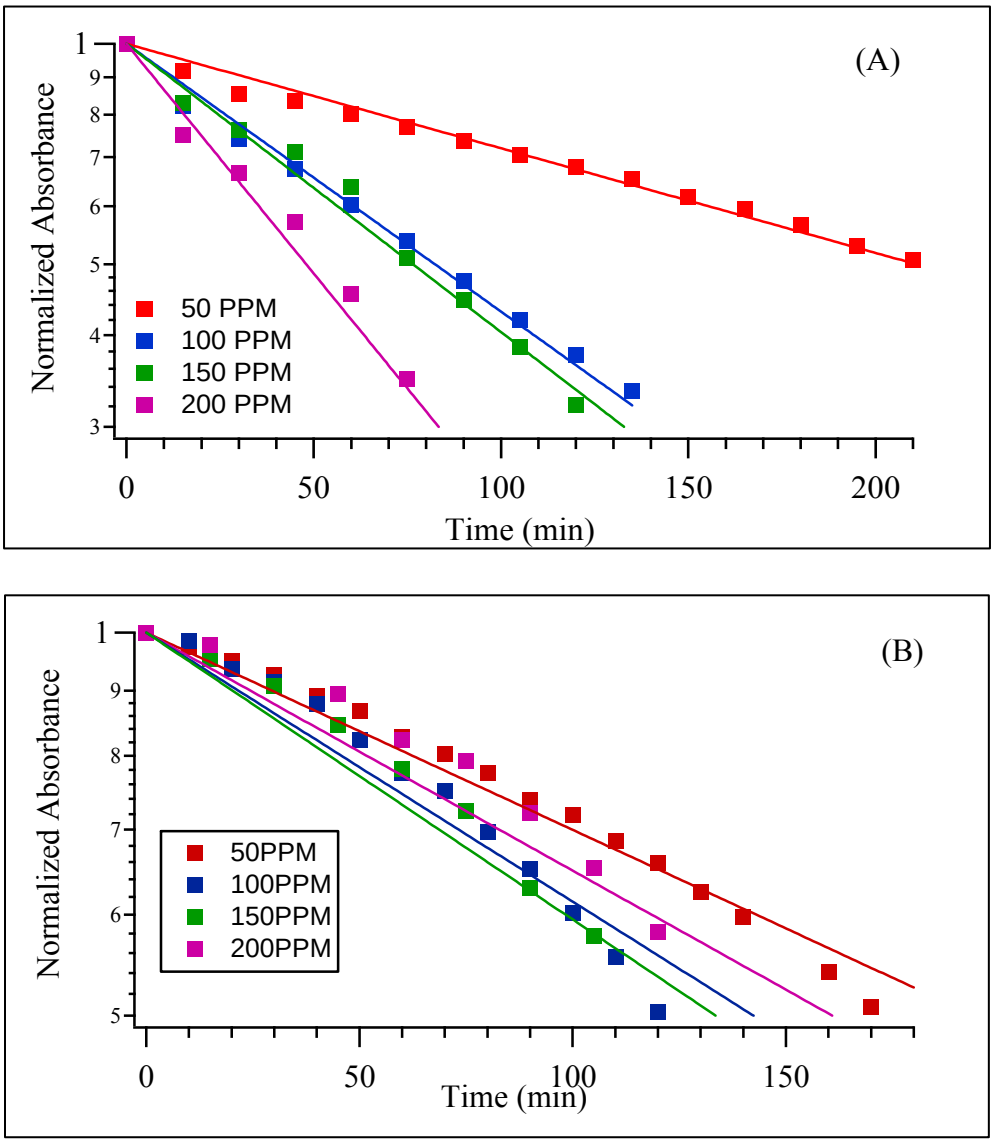

Figure 5.3: Normalized absorbance using UV-Vis spectroscopy for the photocatalytic degradation of MO using titania-microgels as the photocatalyst source at (A) pH of 2 and (B) pH of 6.5. Symbols represent the normalized absorbance at pre-determined time intervals and the lines are drawn as fits using equation 5.13.

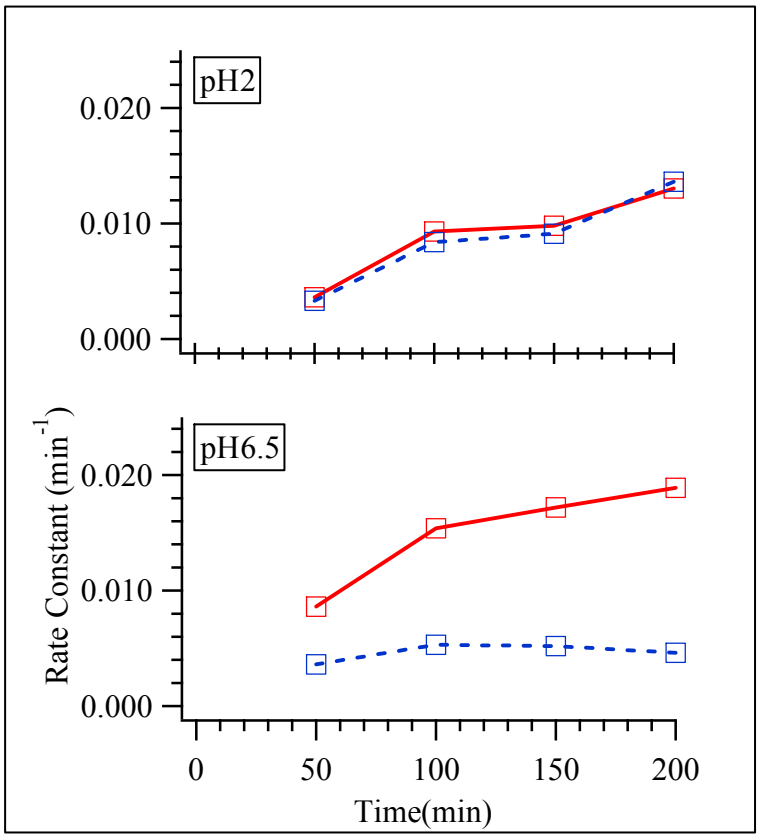

Figure 5.4: Rate constants for the photocatalytic degradation of MO using freely suspended titania (squares) titania-microgels (circles) at a pH of 2 (A) and a pH of 6.5 (B). Lines are drawn as a guide to the eye.

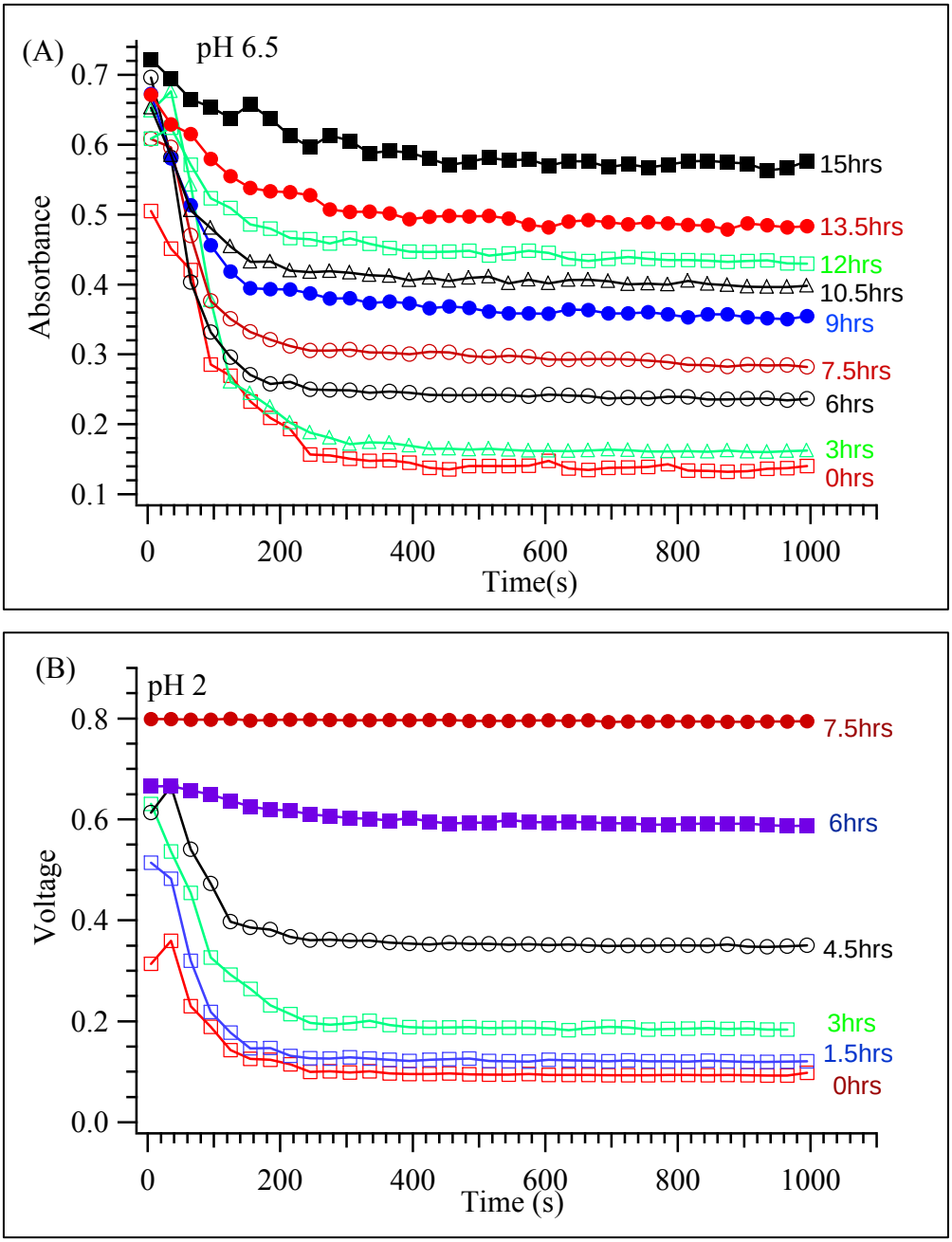

Figure 5.5: Turbidity measurement as a function of time reflecting sedimentation in a solution of the titania-microgels at (A) pH 6.5 and (B) pH 2.

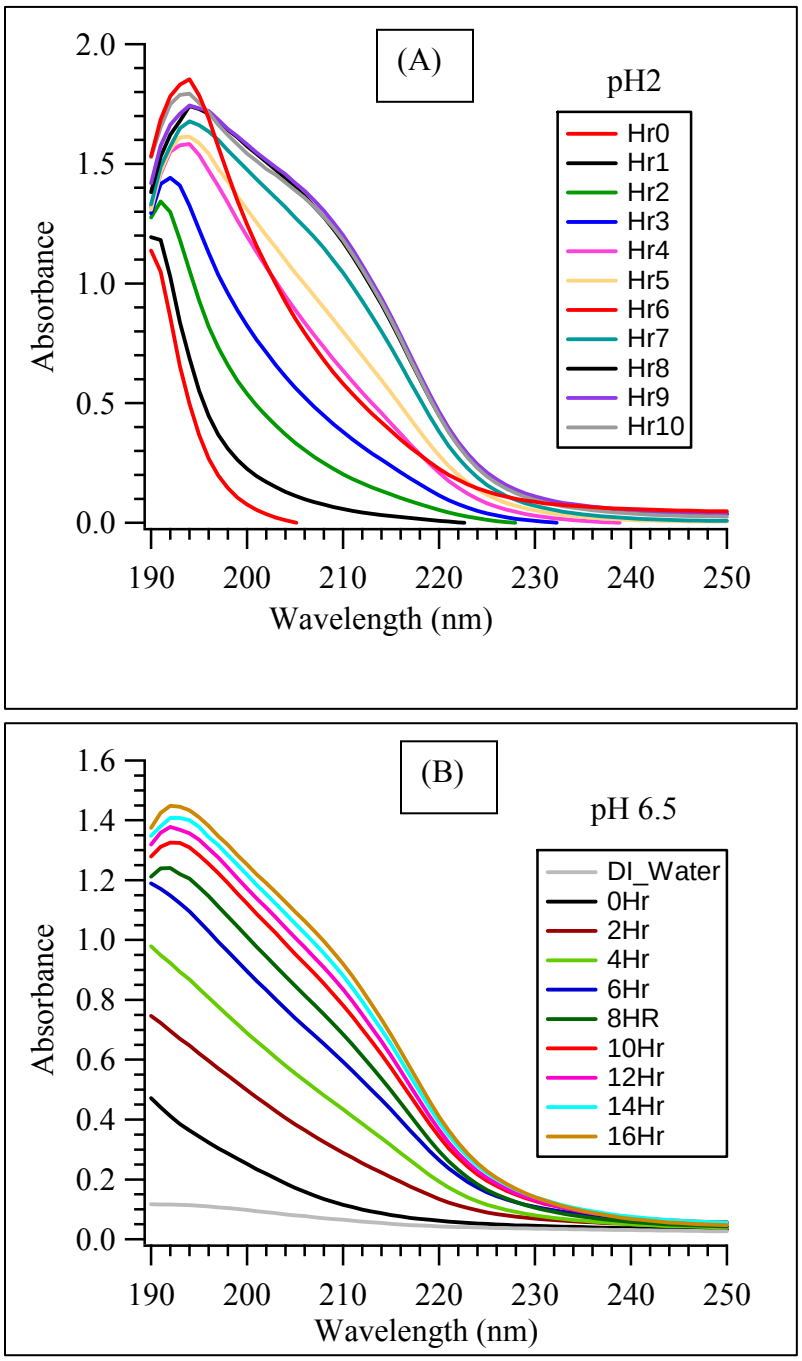

Figure 5.6: Optical absorption from the oligomeric species present in the supernatant solution after titania-microgels have been irradiated for different durations. The curves correspond to (A) pH2 and (B) pH6.5.

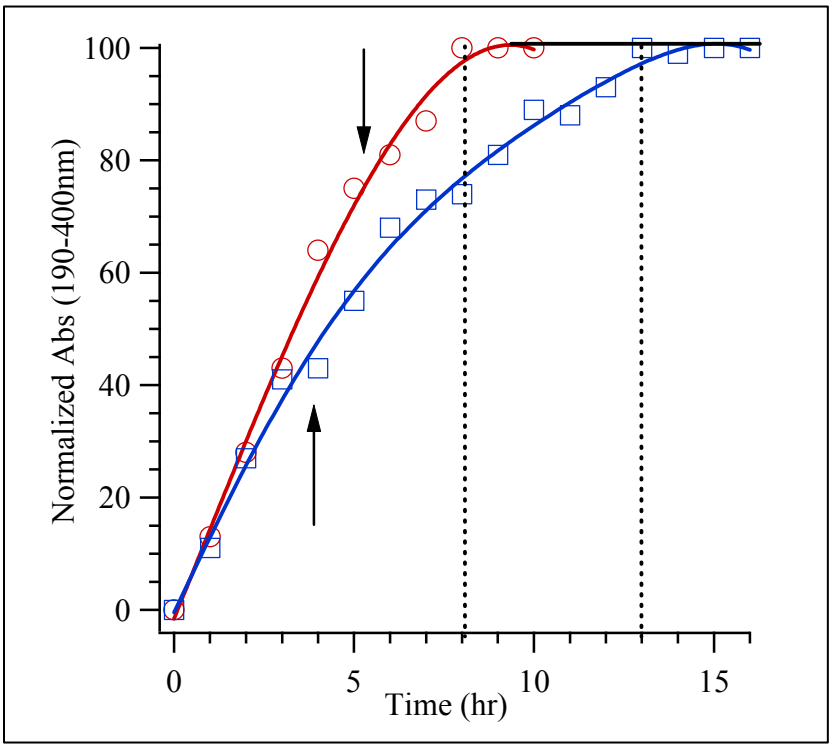

Figure 5.7: The optical signal is shown as a percentage of the plateau value (dashed lines) obtained at long times. The solid lines are drawn as a guide to the eye. Arrow indicates the typical times at which significant changes in settling were observed in figure 5.4 (A) and (B).

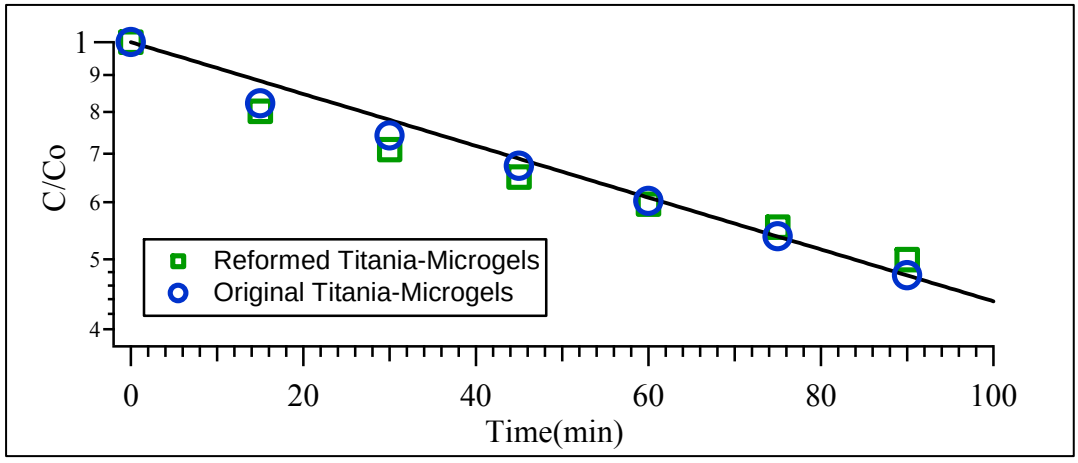

Figure 5.8: Rate constants of the reformed and original microgel-titania particles at pH2.

CHAPTER 6: CHEMICAL MECHANICAL POLISHING USING MICROCOMPOSITE AND HYBRID PARTICLES

6.1. Introduction to CMP

CMP has become a critical processing step in the fabrication of next generation electronic devices as the semiconductor industry advances to sub-45nm technology nodes[124-126]. The reduction in device dimensions has led to stringent requirements for the post-chemical mechanical polishing surface quality. In addition to global planarization and high polish rate, the CMP process also needs to achieve high material selectivity and a superior surface finish.

For silicon oxide CMP, achieving a superior surface quality includes fewer scratches with minimal oxide dishing and nitride erosion. This is important for shallow trench isolation (STI) CMP, which is used extensively for logic device fabrication. However, the advantages of using CMP as a global planarization technique can be quickly nullified by contamination from slurry chemicals, particle contamination (residue) and scratches during polishing due to agglomerated particles. Also, other pattern-related defects like dishing and erosion, delamination, and dielectric crushing hamper the device yield and quickly negate the advantages of using CMP[29, 127]. Therefore, making improvements in the polishing process to reduce the surface defects is an important engineering challenge.

The quality of the post-CMP wafer surface depends on a wide variety of factors such as the characteristics of the abrasive particles, process conditions, particle concentration in the slurry, hardness of the pad, and chemistry of the slurry[128-132]. Controlling the characteristics of the abrasive particles is particularly significant for improvements in the CMP process. For example, controlling the particle agglomeration in the slurry can greatly aid in reducing surface scratches and the need of post-processing techniques to remove defects[28, 133-135]. Commonly used ceramic abrasive particles are much harder than the low dielectric constant materials like copper and silica that are used to blanket the wafers during lithography. This abrasion often results in permanent scratch defects and can lead to problems such as delamination or formation of puddles in subsequent layers of metallization that cause electrical short circuits[136, 137]. Therefore, tailoring the particle hardness or softness is important. Particle characteristics that result in low friction at the interface are beneficial to the CMP process since lower friction helps reduce surface damage during CMP[138]. Similarly, particles that leave minimal residue on the wafer surface after CMP also improve the yield and effectiveness of the polish while enhancing further lithography on nanometer dimensions.

The research in this dissertation has focused on both hybrid and microcomposite abrasive particles as a route to addressing the challenges in the CMP process. Recent advances in slurry development have involved mixed or modified abrasive particles that reduce defects during CMP[139-141]. These studies have focused on abrasives of different inorganic oxides, different sizes of inorganic oxides, and the use of micelles of surface-active compounds. The surface scratches and particle residue have not been addressed using these methods since the inherent material characteristics of the abrasive particle

that interacts with wafer surface remain unchanged. Polymer-silica particles prepared by other researchers have shown fewer surface defects as compared with commercial slurries but these particles appear to aggregate at the water-air interphase due to poor dispersion[28, 61]. In this research, a promising approach for reducing surface defects during polishing by using slurries of (A) hybrid abrasive particles and (B) microcomposites of siloxane-ceria-microgels was pursued.

6.2. Experimental Details for Polishing Studies

Slurries were used to polish thermally grown silicon oxide wafers using a bench-top CMP tester (CETR CP-4). Figure 6.1 shows a schematic of this apparatus where the slurry, typically containing abrasive particles flows, onto the polymer polishing pad. Some of these abrasive particles are sandwiched between the polishing pad and the wafer, thereby resulting in the removal of material from the wafer surface. Using this bench-top CMP tester, the programmable forces, speeds, and slurry flow rates can be chosen to simulate CMP processes and to understand the process in greater detail. Figure 6.2 shows a digital image of this bench-top tester that includes a 6-inch polishing pad and can hold up to a 2-inch wafer to be polished. A dual force sensor allows for continuous monitoring of lateral and normal forces in situ at a total sampling rate of 20 kHz. All the slurries were well agitated during experimentation to reduce sedimentation of the abrasive particles. Conditioning of the IC1000 perforated polishing pad and suba500 sub-pads was conducted for 10min using deionized water and a commercial diamond grid conditioner from 3M with a 400 grit size. The planarization of 1.5 in. square oxide wafers was

carried out on the CMP bench-top polisher using slurries of the hybrid and microcomposite particles.

Aqueous slurries of the siloxane-microgel hybrids, core-shell particles and siloxane-nanogel hybrids were prepared with the pH adjusted to ~12 using sodium hydroxide, since basic solutions have been shown to aid in the removal of silica from the wafer surface[142]. No additives were used to ascertain the contribution of particle morphology to the abrasive action that occurs during CMP processes. For the microcomposite particles, slurries consisting of 0.5wt% siloxane-ceria-microgels with approximately 50 wt% ceria were used to maximize silicon oxide removal rates from the wafer surface. For comparison, slurries with commercial ceria particles with two different weight percentages were also used. A slurry that contained 0.25 wt% ceria particles was used to keep the content of ceria the same between the slurries of the microcomposite particles and the commercial ceria particles. Additionally, slurry with 0.5 wt% ceria particles was also used to keep the total weight percent of particles the same between the slurries of the microcomposites and the commercial ceria particles. All slurries were dispersed in deionized water at a pH of 5 to maintain a slight positive charge on the CeO_2 (ISP of CeO_2 occurs at pH~7.5) that helps disperse the ceria more evenly and aids in abrading the negatively charged silica surface (ISP of silica pH~2.3).

Table 6.1: Process conditions for polishing oxide wafers.

Parameter	Value
Pressure	7psi
Pad RMP	200 RPM
Slurry flow rate	75ml/min
Slider velocity	3mm/s
Slider stroke	7mm

The planarization was conducted for 3min at room temperature and all CMP experiments were repeated to ensure reproducibility. The process conditions for the polishing experiments are tabulated in table 6.1. The pad rotation speed is comparable to other reports in the literature[143-145]. To examine the removal rates of the silica from the wafer surface and to test for organic residue on the polished surface, infrared spectroscopy was used.

6.3. Results and Discussion

Although the hybrid and core-shell particles produced a superior surface finish (resulting in very planar surfaces) compared to commercial inorganic slurries, the removal rates of oxide from the wafer surface were low (<15nm/min) with considerable values for the co-efficient of friction (~0.25)[59]. This was a major drawback for any commercial CMP applications. To overcome this removal rate limitation, incorporation of inorganic nanoparticles such as ceria within the microgels was pursued. While

nanoparticles of ceria are well known for their selectivity and removal of oxide from a wafer surface, prior studies have shown that they can also produce major and minor scratches[146-150]. Therefore, microcomposites of ceria nanoparticles and siloxane-microgel hybrids with interpenetrating PAAc were investigated to as a route towards significant improvements in the surface finish while achieving practical rates for oxide removal.

FTIR characterization of the wafer surface before and after CMP using the microcomposites of ceria nanoparticles and siloxane-microgel hybrids revealed that there was no polymer deposition onto the wafer surface. This is evident in figure 6.3 by the lack of amide or carbonyl absorption. The intensity of the absorption peak of Si–O–Si at 1075cm^{-1} decreased after polishing (inset in figure 6.3), which indicates substantial removal of the oxide layer by the ceria and ceria-microgel microcomposite slurries). Qualitatively, the reduction in absorption at 1075cm^{-1} in figure 6.3 shows that the 0.25wt% ceria slurry and 0.5wt% microcomposite slurry achieves nearly identical removal of the oxide while the slurry containing 0.5 wt% ceria removes nearly twice the amount of oxide.

Table 6.2: COF and removal rate for slurry polishing with different particles.

Slurry	**COF**	**Removal rate (nm/min)**
0.5wt% ceria-polymer composites	0.155 ± 0.013	98 ± 0.25
0.5wt% CeO_2	0.215 ± 0.011	236 ± 2.54
0.25wt% CeO_2	0.108 ± 0.010	111 ± 1.34

Quantitative thickness measurements of the oxide film on the wafer were performed using ellipsometry at multiple angles. The ellipsometry results in table 6.2 are consistent with the qualitative conclusions from the FTIR results in figure 6.3. Figure 6.4, shows the ellipsometric analysis that was conducted to quantitatively determine the amount of oxide on the wafer surface. Scans were done at four different angles (60º, 65º, 70º and 75º) on the blank wafer and wafers polished with the ceria (0.25wt% and 0.5wt%) and the ceria-microgels (0.5wt%). Each wafer was polished for three minutes using the slurry. In figure 6.4, the solid lines indicate the fits to the experimental data (symbols).

The removal rates that are shown in table 6.2 for slurries containing ceria alone are comparable to other literature reports. Kim and co-workers[151] have reported a removal rate of ~250 nm/min using slurries containing 0.5 wt% of ceria and an anionic acrylic polymer dispersant while Manivannan and Ramanathan[152] have reported removal rates of ~75 nm/min using 0.25 wt.% ceria dispersed in an aqueous solution at pH 5. The increase in removal rate using the microcomposites over that when using the hybrid microgel without any ceria makes it feasible to use these microcomposite particles for polishing in the final stages of CMP process where only moderate amounts of material needs to be removed but superior surface quality is required. Since the slurries used here contain no additives or accelerants and also have a low weight fraction of particles, further optimization of the removal rates using chemicals and changing the particle concentration remains an option.

Table 6.2 also lists the co-efficient of friction (COF) data measured during polishing. The COF was obtained from the ratio of lateral and normal forces measured in situ using a dual force sensor installed to the upper carriage of the machine carrying the

wafer carrier. The average co-efficient of friction after the process has reached the steady state is shown. As shown in figure 6.5A, the COF reaches an average value from 100-150s. The distribution of these COF values for both the ceria and microcomposite slurry is plotted in figure 6.5B. This can be best described using a normal Gaussian plot, which gives the mean values for the COF (Table 6.2) along with the standard deviations. Average values of COF reveal that the slurry containing 0.25 wt% ceria particles resulted in lower co-efficient of friction compared to the slurry containing 0.5 wt% of ceria particles. This is plausibly due to the lower concentration of the ceria nanoparticles. Interestingly, the siloxane-ceria-microgels lead to reduced friction at the polishing interface even though 0.5 wt% slurry of these particles should contain a higher number concentration given the lower mass density of the organic polymer. Thus, the lower COF supports the expectation that the microcomposite particles result in a milder abrasive interaction with the surface.

It is crucial to study the post-CMP surface characteristics to draw any conclusions regarding the performance of microcomposites. Optical microscopy images of the post-CMP oxide surface are shown in figure 6.6. It is evident that slurries with commercial ceria particles resulted in severe scratches and pitting on the wafer surface. In contrast the surfaces polished with slurries consisting of the microcomposites resulted in few surface defects and other related surface defects. The reduction in surface scratches and damage can be attributed to reduced abrasive action due to the deformable polymeric component of particles. AFM images in figure 6.7 shows that particle contamination occurs on wafer surfaces polished with only ceria nanoparticles. The wafer surface polished with the microcomposite particles is devoid of pitting and minor scratches. The generation of

defects in surfaces polished with ceria alone is consistent with results reported in past studies that use slurries containing inorganic particles as abrasives[146-150].

Quantitative assessment of the roughness of surfaces from data obtained using atomic force microscopy has been studied in the past and several statistical parameters have emerged[153]. One common measure of the roughness is the root-mean-square (R_{rms}) that details the deviation of the heights of the various features imaged by AFM. However, it is well known that R_{rms} is scale-dependent and a single value can be misleading as it provides little information on the width or spacing of surface features that correspond to R_{rms}. Bonnell and co-workers[153] have evaluated the merits of several statistical parameters and have shown that it is more appropriate to determine the variational roughness at different lateral length-scales. Beyond a characteristic length of the surface, the value of roughness becomes scale-independent and can be specified as a characteristic of the surface. Implementing a surface roughness analysis algorithm described by Bonnell and co-workers[153] using the AFM images for the polished surfaces gives the variational roughness plotted in figure 6.8. For the surfaces polished with the commercial ceria nanoparticles, the surface roughness begins to become somewhat independent beyond a spatial scale of 10μm while this occurs at approximately 2μm for the surfaces polished with the siloxane-ceria-microgels. This helps add weight to the argument that the surfaces polished with the microcomposites have better planarization than those polished with just the ceria nanoparticles. It is also evident that the macroscopic roughness beyond the 10μm is much larger for the polishing with commercial ceria and that there is greater variability in the roughness results. The results presented above clearly indicate that the microcomposite particles with controlled softness/hardness can

be beneficial and can be successfully implemented for polishing in the final stage of CMP process where only moderate amounts of material need to be removed but superior surface quality is required. Fewer surface defects and particle residue will aid in the elimination of rigorous post-CMP cleaning stages and, consequently, will help in achieving environmentally-benign CMP processes.

6.4. Summary

A variety of abrasive particles such as core-shell particles, siloxane-ceria-microgels microcomposites, and hybrid microgel/nanogels were studied for the CMP of silicon oxide wafers. However, the siloxane-ceria-microgels were the most efficient and can form the basis of novel slurries for CMP. These siloxane-ceria-microgels contained an average mass fraction of approximately 50wt% ceria. Planarization of silicon dioxide wafers in bench-top CMP tester and subsequent characterization of the polished wafers revealed that slurries formed from the siloxane-ceria-microgels lead to removal rates of the oxide from the surface at ~100nm/min. More importantly, the polished surfaces showed lower topographical variations and surface roughness than when polished by slurries of only ceria nanoparticles. Polishing with these novel siloxane-ceria-microgels yielded surfaces devoid of scratches and particle deposition, which makes these particles suitable for next generation slurries in CMP.

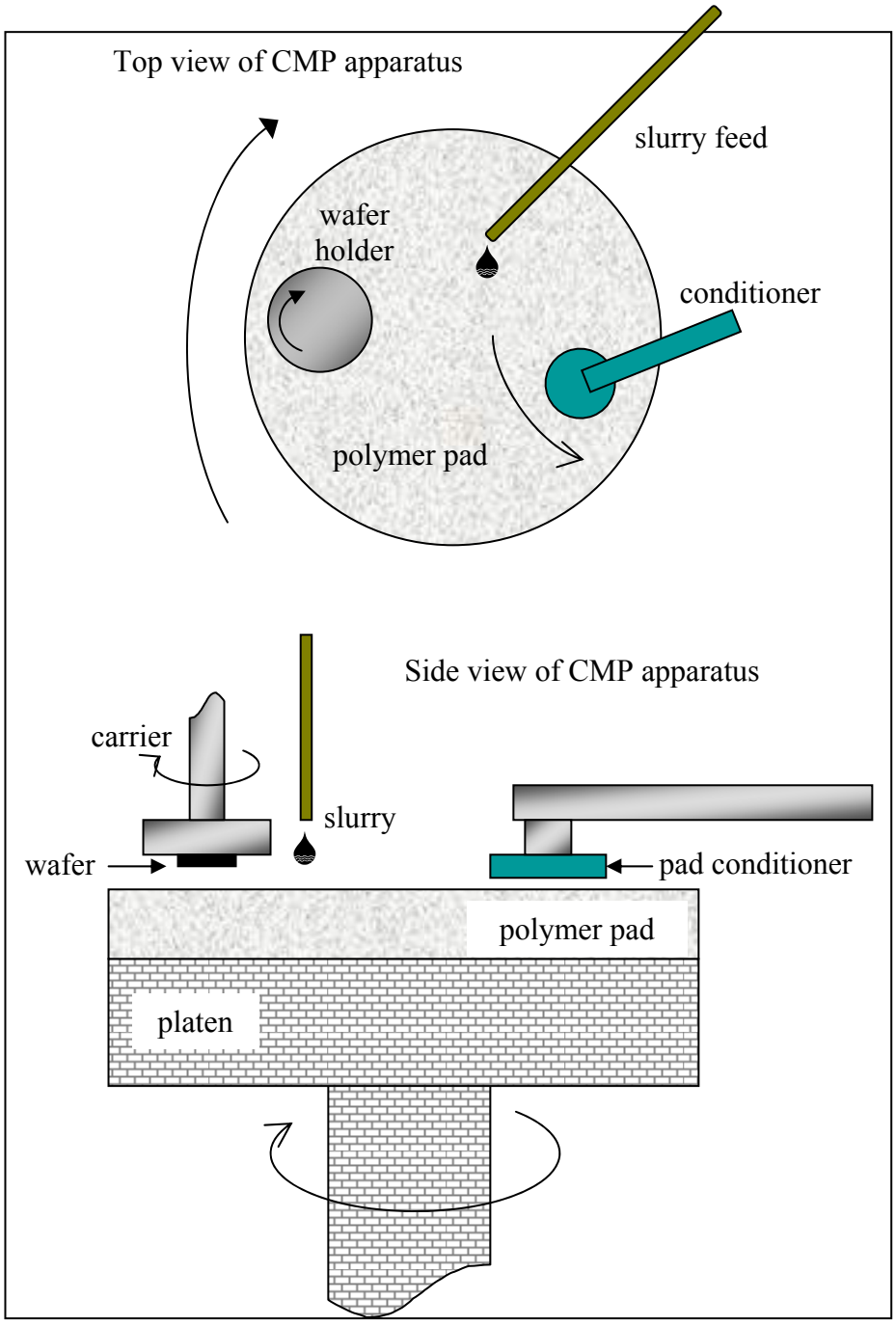

Figure 6.1: Schematic of the CMP apparatus.

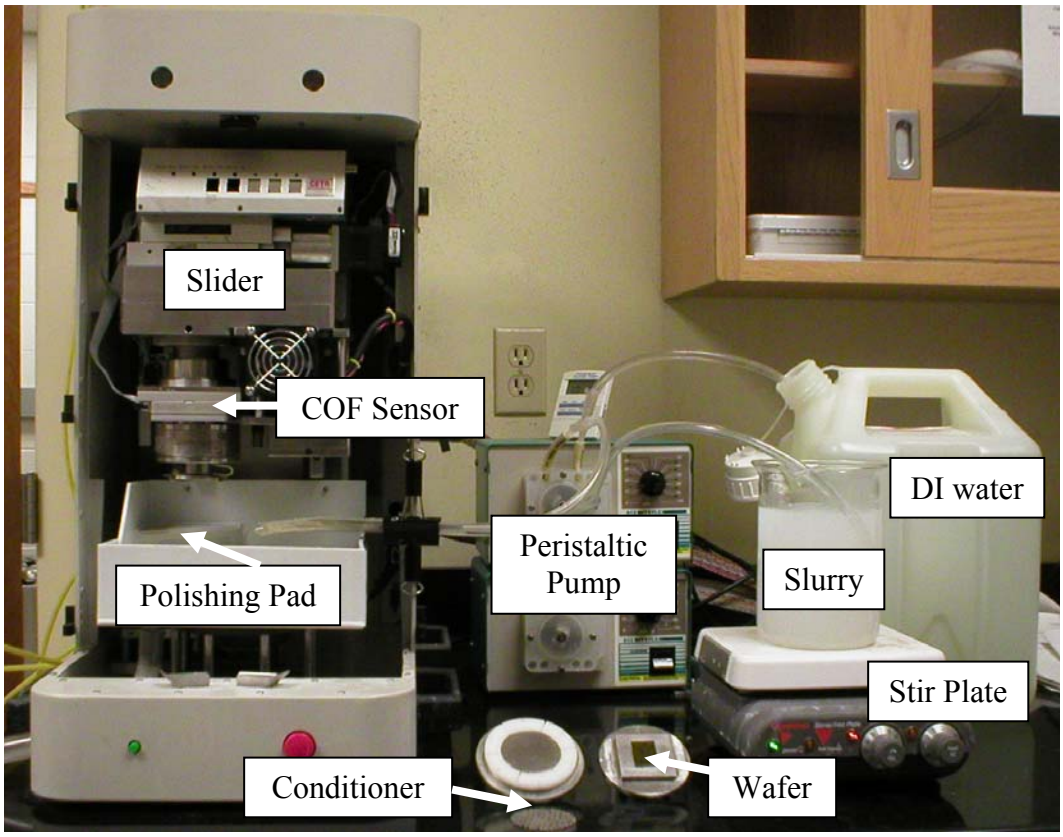

Figure 6.2: Digital image of the bench-top CMP tester and other necessary inputs.

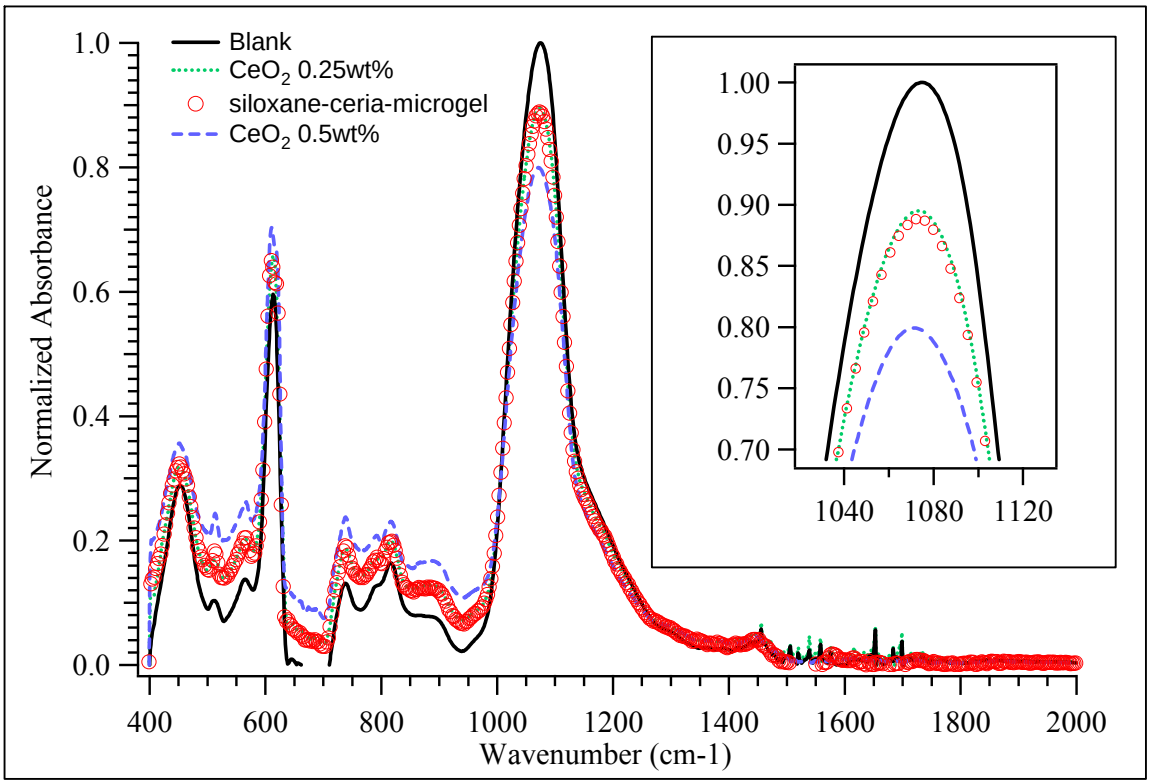

Figure 6.3: FTIR characterization of silica removal from the wafer surface.

Inset: peak of Si-O-Si absorbance centered at 1075cm^{-1}.

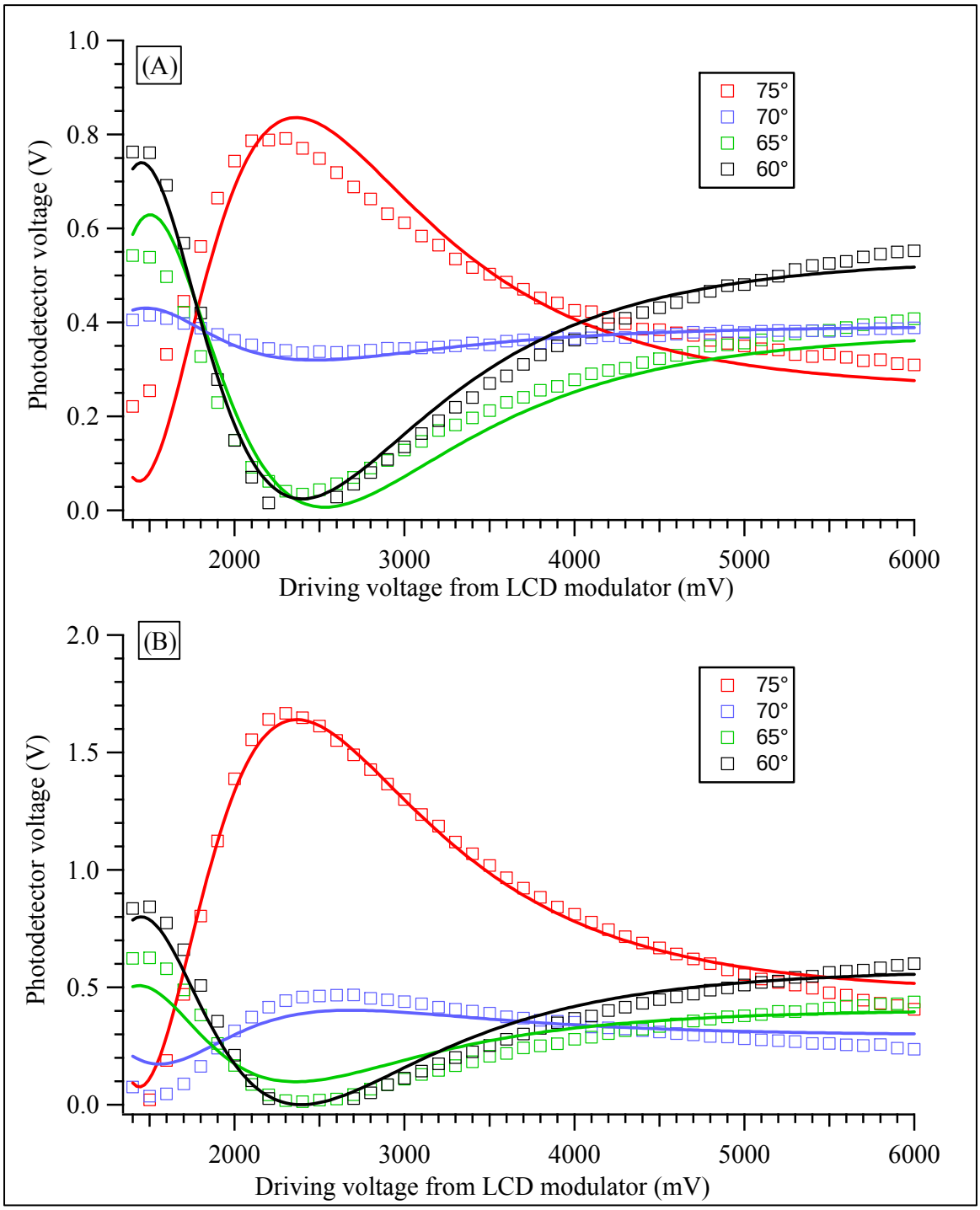

Figure 6.4: Quantitative ellipsometric characterization of silica removal from the wafer surface where (A) wafer polished using the ceria-microgel particles (B) blank wafer.

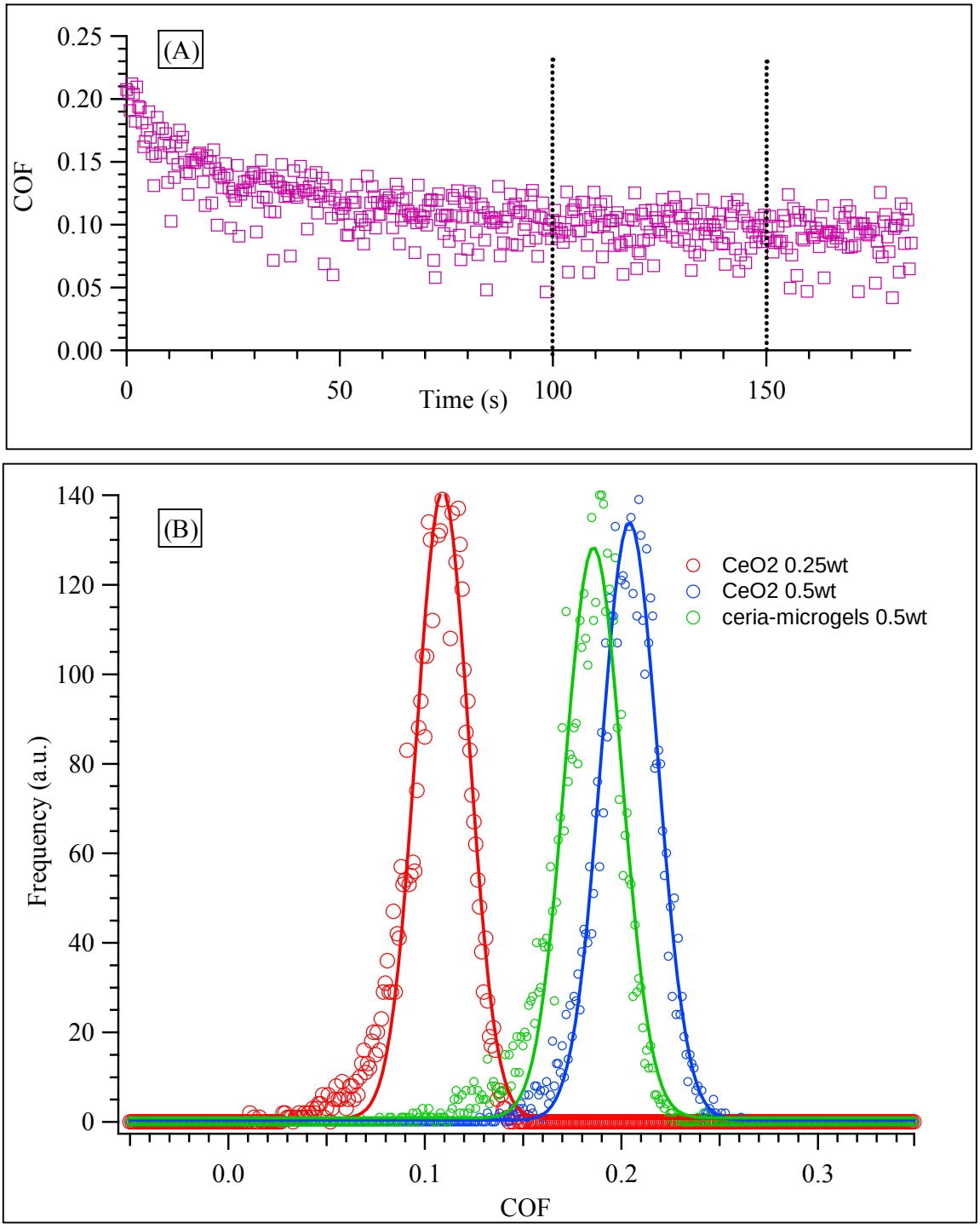

Figure 6.5: (A) COF variation with time and (B) distribution of the COF between 100-150s such that the solid line indicates the Gaussian fit to the actual COF values (circles).

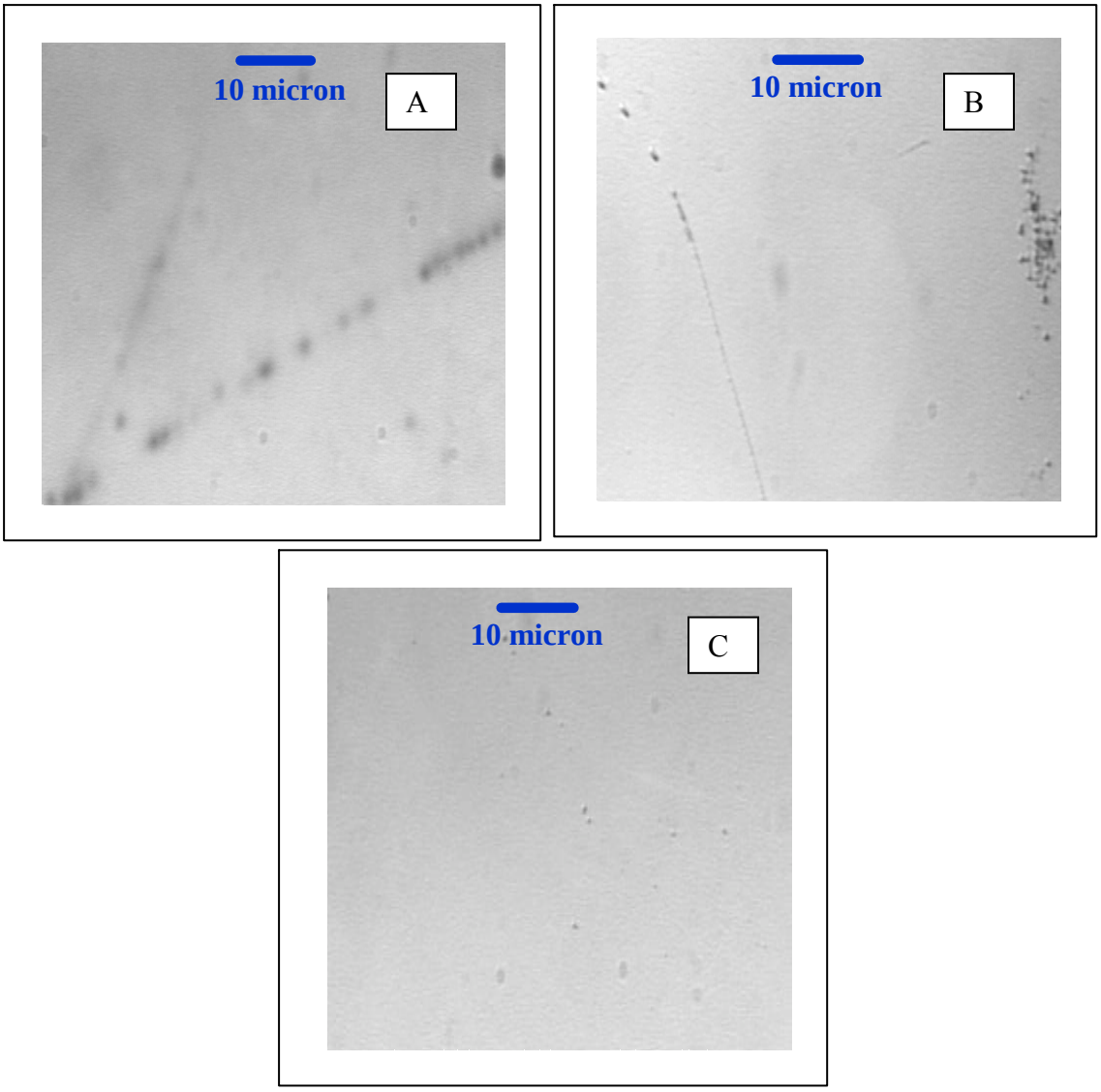

Figure 6.6: Optical microscopy images of wafers polished with slurries containing (A) 0.5wt% ceria nanoparticles (B) 0.25wt% ceria nanoparticles (C) 0.5wt% siloxane-ceria-microgel (50wt% CeO_2).

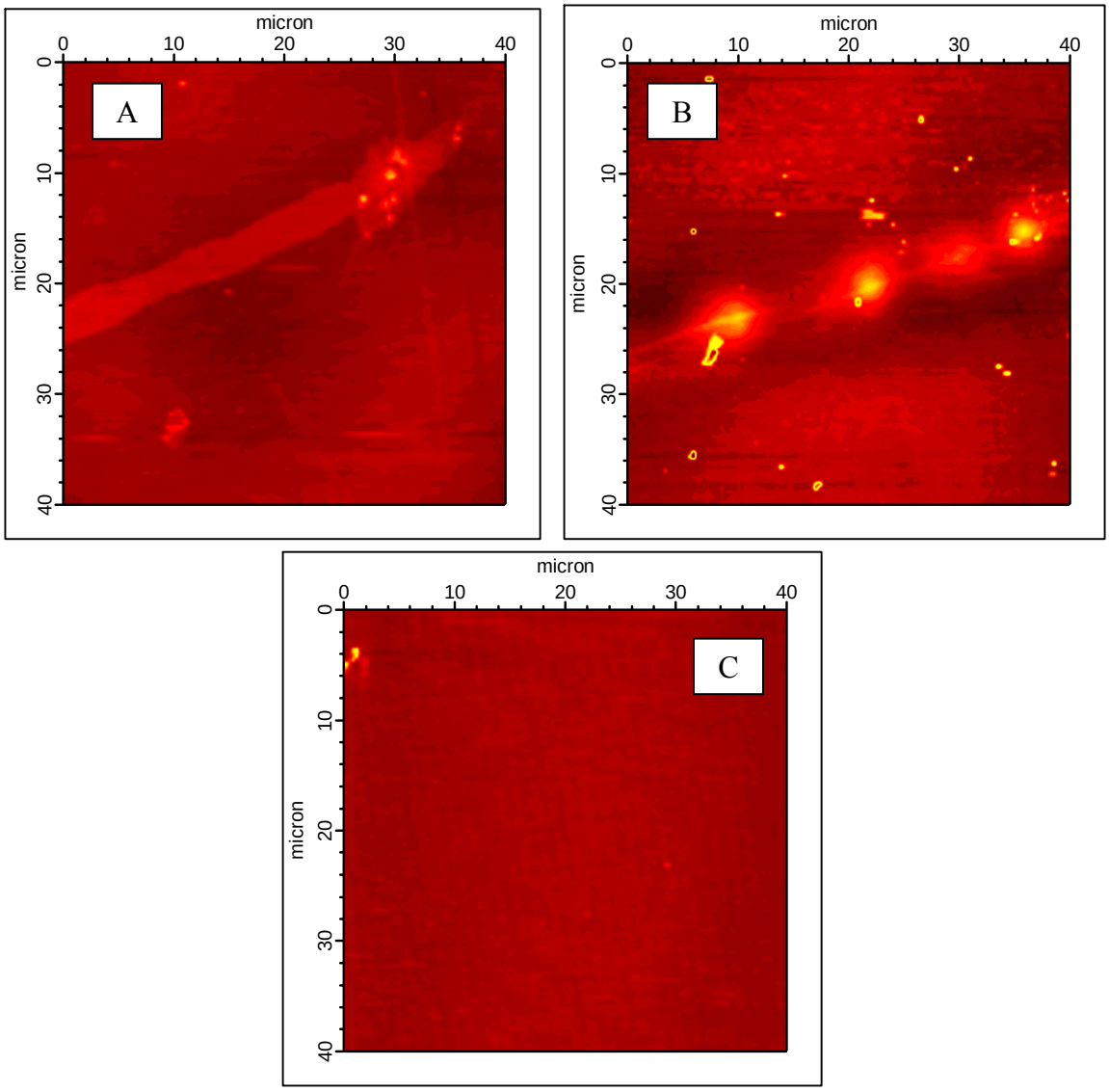

Figure 6.7: AFM images of wafers polished with slurries containing (A) 0.5wt% ceria nanoparticles (B) 0.25wt% ceria nanoparticles (C) 0.5wt% siloxane-ceria-microgels.

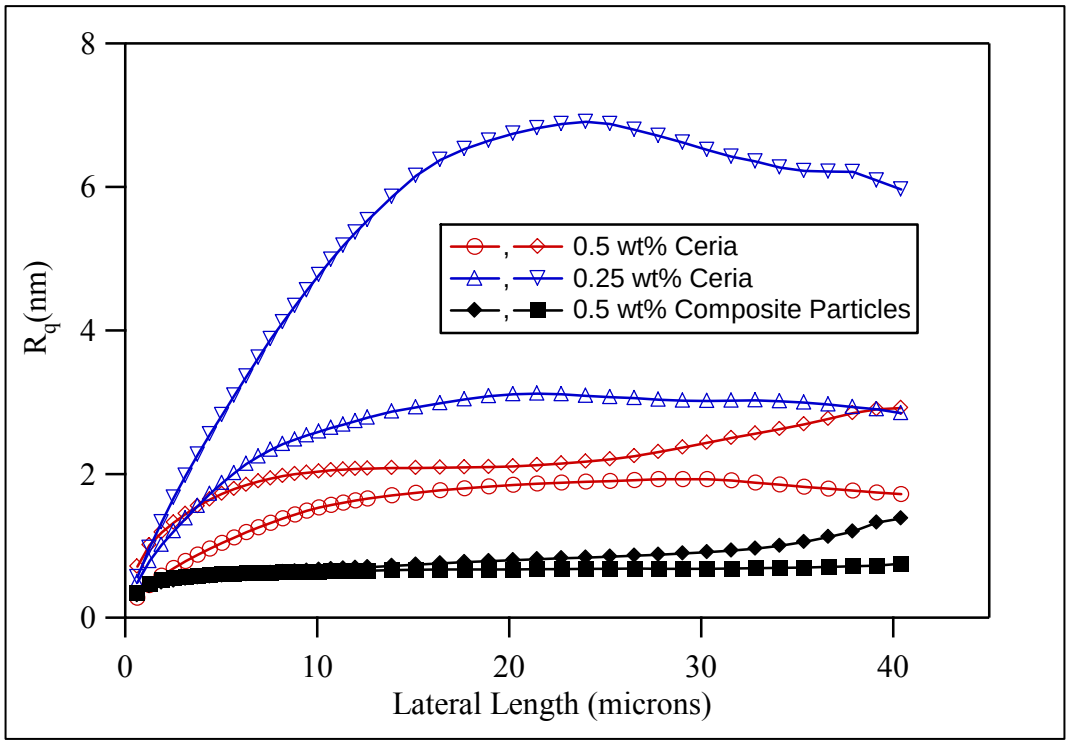

Figure 6.8: Variational surface roughness of the polished wafers.

CHAPTER 7: SUMMARY AND CONCLUSIONS

In this doctoral research, novel hybrid and microcomposite particles were synthesized. In particular, the approach of making microcomposites using interpenetrating microgels of PAAc and PNIPAM with CeO_2 or TiO_2 nanoparticles was demonstrated experimentally. Extensive characterization was conducted using light scattering, spectroscopy, microscopy and thermal gravimetric analysis to understand the morphology, responsive behavior and structure of the microcomposites. Additionally, the sedimentation behavior of the titania-microgels was examined and the results presented within this dissertation demonstrate the general usefulness of settling as a simple characterization of complex composite particles. The sedimentation rate could also be used as a technique to estimate the loading of inorganic nanoparticles within the polymeric framework. The photodegradation of a model organic compound, methyl orange, was investigated using both the rapidly settling titania-microgel particles and freely suspended titania as a control. Under acidic conditions, the reaction rate constants were found to be identical while the freely suspended titania showed faster rate kinetics near neutral conditions. However, the nearly hundred times faster sedimentation of the titania-microgels makes them promising candidates for applications such as wastewater remediation. Additionally, the rate kinetics of the process could be easily tuned with a simple change in the acidity of the wastewater when using the titania-microgels. The interplay between the titania, PAAc and adsorbate has been detailed within this

dissertation. Lastly, siloxane-ceria-microgels that contained an average mass fraction of 50wt% ceria were found to be useful for the CMP of oxide wafers. Planarization studies using a bench-top CMP tester and subsequent characterization of the polished wafers revealed that slurries formed from the siloxane-ceria-microgels led to practical removal rates of oxide from the surface that makes these particles commercially viable. More importantly, the polished surfaces showed lower topographical variations and surface roughness than when polished by slurries containing only ceria nanoparticles.

7.1. Future Prospects and Recommendations

There are several aspects of this research that can be extended to enhance the commercial viability of microcomposites and to provide additional insights for engineering microcomposite particles in the future. In this context, two areas of interest are outlined below. Since only about 7% of sunlight contains UV radiation, one of the areas described below focuses on shrinking the fairly large band gap of titania into visible regions for economically attractive remediation processes[154]. This can also be extended from simple remediation process to self-cleaning sprays or paints that already have been seen commercially but to a limited extent. One of the drawbacks is that even though other researchers have shown that the band gap of titania can be easily shifted via doping, the resulting photocatalysts are not very active, with a decrease in the rate constants[155-157]. The second area of discussion focuses on CMP. Even though the novel microcomposites prepared and tested here provided good removal rates with excellent surface characteristics, ceria based slurries can be quite expensive due to the large slurry

consumption during CMP. Therefore, the synthesis of abrasive polishing pads that contain ceria nanoparticles is discussed.

7.2. Doping of Titania to Shift the Band-Gap

Although nanoparticles of titania have proven to be extremely photocatalytically active, its band gap (3.2eV) can be limiting for wastewater remediation and other applications. Since ultraviolet radiation only accounts for only a small fraction of the sun's energy as compared to visible light (45%), any shift in the optical response of titania from the UV to the visible spectral range will have a profound effect on the photocatalytic efficiency and marketability of titania as a next generation 'green' technology. Recent research has shown that this band gap can be shifted via doping with nitrogen, chromium and other heavy metal ions. The shifting of the optical response of TiO_2 from the UV to the visible spectral range has been first investigated by doping TiO_2 with transition metal elements[158-160]. However, it has been shown that metal doping has several drawbacks; namely, the doped photocatalyst suffers from thermal instability, and the metal centers act as electron traps, thereby reducing the photocatalytic efficiency. To circumvent these difficulties, considerable efforts have been undertaken to dope TiO_2 powders with nitrogen, due to the closer proximity of nitrogen to oxygen in the periodic table [161, 162]. There are a number of techniques that have been used to incorporate nitrogen within the titania lattice structure. These include ball-milling, sol-gel synthesis, sputtering, ion implantation, sintering of titania in an ammonia atmosphere and plasma processes[156, 163-166]. Among these, the sol−gel process is the most adopted method for the synthesis N-doped TiO_2 nanoparticles because doping levels as well as the size of

nanoparticles can be easily controlled depending on the reaction conditions such as the solvents used, pH, temperature, and hydrolysis rate.

7.3. Abrasive Pads for CMP

The microcomposite particles pursued in this doctoral research represented an interesting system for CMP since soft polymeric segments were coupled with harder inorganic nanoparticles. This concept has the potential for the synthesis of organic-inorganic abrasive pads. In literature reports, interactions between a soft pad, hard abrasive particles, and the wafer surface have been considered using a variety of approaches that extend from modeling[167, 168] to experiments[169]. In an experimental study, Castillo-Mejia and coworkers found that reducing the elastic modulus of an IC 1000 pad surface led to lower polishing rates. In an earlier study by Stavreva et al[131], the use of stacked pads with a hard top (IC 1000) and a compressible bottom layer (SUBA IV) was found to give better uniformity during polishing with an alumina-based slurry. More recently, Yongguang Wang et al.[21] developed a nonlinear relationship between the indentation depth and the particle/soft-pad microcontact force for the CMP process in case of a single particle. Based on this model, they suggest that as the numbers of particles embedded in a soft pad increase, a higher material removal rate and global planarization should be achieved. Based on all these past studies, the development of composite films for abrasive CMP polishing pads coupled with abrasive free slurries can be an attractive pursuit. This also helps eliminate problems such as particle sedimentation and agglomeration that frequently cause non-uniform planarization. Additionally, the use of responsive polymers to fabricate the polishing pads has the potential to tune the

polishing from harder to softer abrasion when desired during the manufacturing process by simply changing external stimuli like temperature or pH of the slurry solution.

REFERENCES

1. Peters, S., *Handbook of Composites*. 1997.
2. Bjorkman, A., Studies on solid wood. I. Comprehension of the natural composite wood. *Cellulose Chemistry and Technology* 1988, 22, (2), 245-54.
3. Chekhov, A. P.; Sergeev, A. M.; Dibrov, G. D., *Handbook of Concretes and Mortars*. 1983.
4. Gouda, M., The first man-made composite material. *Journal of Environmental Research* 2001, 3, 277-286.
5. Taton, T. A.; Lu, G.; Mirkin, C. A., Two-color labeling of oligonucleotide arrays via size-selective scattering of nanoparticle probes. *Journal of the American Chemical Society* 2001, 123, (21), 5164-5.
6. Nagale, M.; Kim, B. Y.; Bruening, M. L., Ultrathin, Hyperbranched Poly(acrylic acid) Membranes on Porous Alumina Supports. *Journal of the American Chemical Society* 2000, 122, (47), 11670-11678.
7. Hafez, H. S.; El-Hag Ali, A.; Abdel-Mottaleb, M. S. A., Photocatalytic efficiency of titanium dioxide immobilized on PVP/AAc hydrogel membranes: a comparative study for safe disposal of wastewater of Remazol Red RB-133 textile dye. *International Journal of Photoenergy* 2005, 7, (4), 181-185.
8. Earle, M. D., The electrical conductivity of titanium dioxide. *Physical Review* 1942, 61, 56-62.

9. Fujishima, A.; Rao, T. N.; Tryk, D. A., Titanium dioxide photocatalysis. *Journal of Photochemistry and Photobiology, C: Photochemistry Reviews* 2000, 1, (1), 1-21.

10. Serpone, N.; Khairutdinov, R. F., Application of nanoparticles in the photocatalytic degradation of water pollutants. *Studies in Surface Science and Catalysis* 1997, 103, 417-444.

11. Frank, S. N.; Bard, A. J., Heterogeneous photocatalytic oxidation of cyanide and sulfite in aqueous solutions at semiconductor powders. *Journal of Physical Chemistry* 1977, 81, (15), 1484-8.

12. Ardizzone, S.; Bianchi, C. L.; Cappelletti, G.; Gialanella, S.; Pirola, C.; Ragaini, V., Tailored anatase/brookite nanocrystalline TiO_2. The optimal particle features for liquid- and gas-phase photocatalytic reactions. *Journal of Physical Chemistry C* 2007, 111, (35), 13222-13231.

13. Liu, S. X.; Chen, X. Y.; Chen, X., A TiO_2/AC composite photocatalyst with high activity and easy separation prepared by a hydrothermal method. *Journal of Hazardous Materials* 2007, 143, (1-2), 257-263.

14. Qiu, W.; Zheng, Y.; Haralampides, K. A., Study on a novel POM-based magnetic photocatalyst: Photocatalytic degradation and magnetic separation. *Chemical Engineering Journal* 2007, 125, (3), 165-176.

15. Hoffmann, M. R.; Martin, S. T.; Choi, W.; Bahnemann, D. W., Environmental Applications of Semiconductor Photocatalysis. *Chemical Reviews* 1995, 95, (1), 69-96.

16. Asahi, R.; Morikawa, T.; Ohwaki, T.; Aoki, K.; Taga, Y., Visible-light photocatalysis in nitrogen-doped titanium oxides. *Science* 2001, 293, (5528), 269-71.

17. Teoh, W. Y.; Amal, R.; Maedler, L.; Pratsinis, S. E., Flame sprayed visible light-active Fe-TiO_2 for photomineralization of oxalic acid. *Catalysis Today* 2007, 120, (2), 203-213.

18. Chun, H.; Yizhong, W.; Hongxiao, T., : Preparation and characterization of surface bond-conjugated TiO_2/SiO_2 and photocatalysis for azo dyes. *Applied Catalysis, B: Environmental* 2001, 30, (3,4), 277-285.

19. Lee, S. A.; Choo, K. H.; Lee, C. H.; Lee, H. I.; Hyeon, T.; Choi, W.; Kwon, H. H., Use of Ultrafiltration Membranes for the Separation of TiO_2 Photocatalysts in Drinking Water Treatment. *Industrial & Engineering Chemistry Research* 2001, 40, (7), 1712-1719.

20. Pozzo, R. L.; Giombi, J. L.; Baltanas, M. A.; Cassano, A. E., The performance in a fluidized bed reactor of photocatalysts immobilized onto inert supports. *Catalysis Today* 2000, 62, (2-3), 175-187.

21. Yue, B.; Wang, Y.; Huang, C. Y.; Pfeffer, R.; Iqbal, Z., Polymeric nanocomposites of functionalized carbon nanotubes synthesized in supercritical CO2. *Journal of Nanoscience and Nanotechnology* 2007, 7, (3), 994-1000.

22. Wang, C.-y.; Liu, C.-y.; Zheng, X.; Chen, J.; Shen, T., The surface chemistry of hybrid nanometer-sized particles. I. Photochemical deposition of gold on ultrafine TiO_2 particles. *Colloids and Surfaces, A: Physicochemical and Engineering Aspects* 1998, 131, (1-3), 271-280.

23. Matsuyama, K.; Mishima, K.; Hayashi, K. I.; Matsuyama, H., Microencapsulation of TiO_2 nanoparticles with polymer by rapid expansion of supercritical solution. *Journal of Nanoparticle Research* 2003, 5, (1-2), 87-95.

24. Bae, H. S.; Lee, M. K.; Kim, W. W.; Rhee, C. K., Dispersion properties of TiO_2 nano-powder synthesized by homogeneous precipitation process at low temperatures. *Colloids and Surfaces, A: Physicochemical and Engineering Aspects* 2003, 220, (1-3), 169-177.

25. Martyanov, I. N.; Savinov, E. N.; Klabunde, K. J., Influence of solution composition and ultrasonic treatment on optical spectra of TiO_2 aqueous suspensions. *Journal of Colloid and Interface Science* 2003, 267, (1), 111-116.

26. Kaufman, F. B.; Thompson, D. B.; Broadie, R. E.; Jaso, M. A.; Guthrie, W. L.; Pearson, D. J.; Small, M. B., Chemical-mechanical polishing for fabricating patterned tungsten metal features as chip interconnects. *Journal of the Electrochemical Society* 1991, 138, (11), 3460-5.

27. Palla, B. J.; Shah, D. O., Correlation of observed stability and polishing performance to abrasive particle size for CMP. *IEEE* 1999.

28. Basim, G. B.; Moudgil, B. M., Effect of Soft Agglomerates on CMP Slurry Performance. *Journal of Colloid and Interface Science* 2002, 256, (1), 137-142.

29. Zhang, L.; Raghavan, S.; Weling, M., Minimization of chemical-mechanical planarization (CMP) defects and post-CMP cleaning. *Journal of Vacuum Science & Technology* 1999, 17, (5), 2248-2255.

30. Huang, G.; Gao, J.; Hu, Z.; St. John, J. V.; Ponder, B. C.; Moro, D., Controlled drug release from hydrogel nanoparticle networks. *Journal of Controlled Release* 2004, 94, (2-3), 303-311.

31. Jones, C. D.; Lyon, L. A., Dependence of Shell Thickness on Core Compression in Acrylic Acid Modified Poly(N-isopropylacrylamide) Core/Shell Microgels. *Langmuir* 2003, 19, (11), 4544-4547.

32. Takata, S.; Shibayama, M.; Sasabe, R.; Kawaguchi, H., Preparation and structure characterization of hairy nanoparticles consisting of hydrophobic core and thermosensitive hairs. *Polymer* 2002, 44, (2), 495-501.

33. Wu, K.; Shi, L.; Zhang, W.; An, Y.; Zhu, X.-X., Adjustable temperature sensor with double thermoresponsiveness based on the aggregation property of binary diblock copolymers. *Journal of Applied Polymer Science* 2006, 102, (4), 3144-3148.

34. Benita, S., *Microencapsulation: Methods and Industrial Applications*. 1996.

35. Das, M.; Sanson, N.; Fava, D.; Kumacheva, E., Microgels Loaded with Gold Nanorods: Photothermally Triggered Volume Transitions under Physiological Conditions. *Langmuir* 2007, 23, (1), 196-201.

36. Gupta, V. K.; Kumar, A.; Coutinho Cecil, A.; Subrahmanya, R. M. Novel Ceria-Polymer Microcomposites for Chemical Mechanical Polishing. 2007. WO 2008052216.

37. Malinverno, G.; Pantini, G.; Bootman, J., Safety evaluation of perfluoropolyethers, liquid polymers used in barrier creams and other skin-care products. *Food and Chemical Toxicology* 1996, 34, (7), 639-650.

38. Nakada, Y. Polymers for chemical mechanical polishing (CMP) compositions. 2004. JP Patent 2004311967.

39. Ma, X.; Xi, J.; Huang, X.; Zhao, X.; Tang, X., Novel hydrophobically modified temperature-sensitive microgels with tunable volume-phase transition temperature. *Materials Letters* 2004, 58, (27-28), 3400-3404.

40. Pelton, R. H.; Chibante, P., Preparation of aqueous latexes with N-isopropylacrylamide. *Colloids and Surfaces* 1986, 20, (3), 247-56.

41. Gao, J.; Frisken, B. J., Cross-Linker-Free N-Isopropylacrylamide Gel Nanospheres. *Langmuir* 2003, 19, (13), 5212-5216.

42. Gao, J.; Frisken, B. J., Influence of Reaction Conditions on the Synthesis of Self-Cross-Linked N-Isopropylacrylamide Microgels. *Langmuir* 2003, 19, (13), 5217-5222.

43. Varga, I.; Gilanyi, T.; Meszaros, R.; Filipcsei, G.; Zrinyi, M., Effect of Cross-Link Density on the Internal Structure of Poly(N-isopropylacrylamide) Microgels. *Journal of Physical Chemistry B* 2001, 105, (38), 9071-9076.

44. Kang, M.-S.; Gupta, V. K., Photochromic Cross-Links in Thermoresponsive Hydrogels of Poly(N-isopropylacrylamide): Enthalpic and Entropic Consequences on Swelling Behavior. *Journal of Physical Chemistry B* 2002, 106, (16), 4127-4132.

45. Vidyasagar, A.; Toomey, R., Temperature induced volume-phase transitions in surface-tethered poly(N-isopropylacrylamide) networks. *Macromolecules* 2008, 41, (3), 919-924.

46. Matsuo, E. S.; Tanaka, T., Kinetics of discontinuous volume-phase transition of gels. *Journal of Chemical Physics* 1988, 89, (3), 1695-703.

47. Ishizu, K.; Khan, R. A.; Furukawa, T.; Furo, M., Controlled radical polymerization of N-isopropylacrylamide initiated by photofunctional 2-(N,N-diethyldithiocarbamyl)isobutyric acid sodium salt in aqueous medium. *Journal of Applied Polymer Science* 2004, 91, (5), 3233-3238.

48. Andersson, M.; Maunu, S. L., Structural studies of poly(N-isopropylacrylamide) microgels: effect of SDS surfactant concentration in the microgel synthesis. *Journal of Polymer Science, Part B: Polymer Physics* 2006, 44, (23), 3305-3314.

49. Xia, X.; Hu, Z., Synthesis and Light Scattering Study of Microgels with Interpenetrating Polymer Networks. *Langmuir* 2004, 20, (6), 2094-2098.

50. Odian, G., *Principles of Polymerization, 4th Edition*. 2004.

51. Bourgeat-Lami, E.; Tissot, I.; Lefebvre, F., Synthesis and Characterization of SiOH-Functionalized Polymer Latexes Using Methacryloxy Propyl Trimethoxysilane in Emulsion Polymerization. *Macromolecules* 2002, 35, (16), 6185-6191.

52. Tissot, I.; Reymond, J. P.; Lefebvre, F.; Bourgeat-Lami, E., SiOH-Functionalized Polystyrene Latexes. A Step toward the Synthesis of Hollow Silica Nanoparticles. *Chemistry of Materials* 2002, 14, (3), 1325-1331.

53. Shin, H.; Collins, R. J.; De Guire, M. R.; Heuer, A. H.; Sukenik, C. N., Synthesis and characterization of TiO_2 thin films on organic self-assembled monolayers: Part I. Film formation from aqueous solutions. *Journal of Materials Research* 1995, 10, (3), 692-8.

54. Debord, J. D.; Lyon, L. A., Synthesis and Characterization of pH-Responsive Copolymer Microgels with Tunable Volume Phase Transition Temperatures. *Langmuir* 2003, 19, (18), 7662-7664.

55. Jones, C. D.; Lyon, L. A., Synthesis and Characterization of Multiresponsive Core-Shell Microgels. *Macromolecules* 2000, 33, (22), 8301-8306.

56. Shin, B. C.; Jhon, M. S.; Lee, H. B.; Yuk, S. H., pH/temperature dependent phase transition of an interpenetrating polymer network: anomalous swelling behavior above lower critical solution temperature. *European Polymer Journal* 1998, 34, (11), 1675-1681.

57. Li, X.; Zuo, J.; Guo, Y.; Yuan, X., Preparation and Characterization of Narrowly Distributed Nanogels with Temperature-Responsive Core and pH-Responsive Shell. *Macromolecules* 2004, 37, (26), 10042-10046.

58. Nayak, S.; Debord, S. B.; Lyon, L. A., Investigations into the Deswelling Dynamics and Thermodynamics of Thermoresponsive Microgel Composite Films. *Langmuir* 2003, 19, (18), 7374-7379.

59. Mudhivarthi, S.; Coutinho, C.; Kumar, A.; Gupta, V., Novel Hybrid Abrasive Particles for Oxide CMP Applications. *ECS Transactions* 2007, 3, (41), 9-19.

60. Coutinho, C. A.; Subrahmanya, M. R.; Gupta, V. K.; Kumar, A., Novel Ceria-Polymer Microcomposites for Chemical Mechanical Polishing. *Applied Surface Science* 2008, 255, (5, Pt. 2), 3090-3096.

61. Ding, X.; Jiang, Y.; Yu, K.; Hari, B.; Tao, N.; Zhao, J.; Wang, Z., Silicon dioxide as coating on polystyrene nanoparticles in situ emulsion polymerization. *Materials Letters* 2004, 58, (11), 1722-1725.

62. Imhof, A., Preparation and Characterization of Titania-Coated Polystyrene Spheres and Hollow Titania Shells. *Langmuir* 2001, 17, (12), 3579-3585.

63. Liu, J.; Pelton, R.; Hrymak, A. N., Properties of Poly(N-isopropylacrylamide)-Grafted Colloidal Silica. *Journal of Colloid and Interface Science* 2000, 227, (2), 408-411.

64. Brach-Papa, C.; Boyer, P.; Ternat, F.; Amielh, M.; Anselmet, F., Settling classes for fine suspended particles. *Comptes Rendus Mecanique* 2006, 334, (8-9), 560-567.

65. Buah-Bassuah, P. K.; Euzzor, S.; Francini, F.; Quansah, G. W.; Sansoni, P., Soil textural classification by a photosedimentation method. *Applied Optics* 1998, 37, (3), 586-593.

66. Dai, X.; Boll, J., Settling velocity of Cryptosporidium parvum and Giardia lamblia. *Water Research* 2006, 40, (6), 1321-1325.

67. Kulkarni, P.; Dutari, G.; Biswas, P.; Haught, R., Gravity settling characteristics of Cryptosporidium parvum oocysts in aqueous suspension using in situ static light scattering. *Colloids and Surfaces, A: Physicochemical and Engineering Aspects* 2004, 233, (1-3), 1-10.

68. van Hamersveld, E. H.; van der Lans, R. G. J. M.; Luyben, K. C. A. M., Quantification of brewers' yeast flocculation in a stirred tank: effect of physical parameters on flocculation. *Biotechnology and Bioengineering* 1997, 56, (2), 190-200.

69. Brinkman, H. C., A calculation of the viscous force exerted by a flowing fluid on a dense swarm of particles. *Applied Scientific Research, Section A: Mechanics, Heat, Chemical Engineering, Mathematical Methods* 1947, A1, 27-34.

70. Happel, J., Viscous flow in multiparticle systems: slow motion of fluids relative to beds of spherical particles. *AIChE Journal* 1958, 4, 197-201.

71. Johnson, C. P.; Li, X.; Logan, B. E., Settling Velocities of Fractal Aggregates. *Environmental Science and Technology* 1996, 30, (6), 1911-18.

72. Kim, A. S.; Stolzenbach, K. D., The permeability of synthetic fractal aggregates with realistic three-dimensional structure. *Journal of Colloid and Interface Science* 2002, 253, (2), 315-328.

73. Tang, P.; Raper, J. A., Modelling the settling behaviour of fractal aggregates - a review. *Powder Technology* 2002, 123, (2-3), 114-125.

74. Veerapaneni, S.; Wiesner, M. R., Hydrodynamics of fractal aggregates with radially varying permeability. *Journal of Colloid and Interface Science* 1996, 177, (1), 45-57.

75. Dickson, J. L.; Shah, P. S.; Binks, B. P.; Johnston, K. P., Steric Stabilization of Core-Shell Nanoparticles in Liquid Carbon Dioxide at the Vapor Pressure. *Langmuir* 2004, 20, (21), 9380-9387.

76. Yang, C.-C., Synthesis and characterization of the cross-linked PVA/TiO_2 composite polymer membrane for alkaline DMFC. *Journal of Membrane Science* 2007, 288, 51-60.

77. Caron, P.; Faucompre, B.; Membrey, F.; Foissy, A., A new white light photosedimentometer for solid-liquid dispersion study: device description, stability and settling behavior. *Powder Technology* 1996, 89, (2), 91-100.

78. Davis, R. H.; Birdsell, K. H., Hindered settling of semidilute monodisperse and polydisperse suspensions. *AIChE Journal* 1988, 34, (1), 123-9.

79. Richardson, E. G., Turbidity measurements by optical means. *Proceedings of the Physical Society, London* 1943, 55, 48-63.

80. Chiklis, C. K.; Grasshoff, J. M., Swelling of thin films. I. Acrylamide-N-isopropylacrylamide copolymers in water. *Journal of Polymer Science, Polymer Physics Edition* 1970, 8, (9), 1617-26.

81. Coutinho, C. A.; Gupta, V. K., Formation and properties of composites based on microgels of a responsive polymer and TiO_2 nanoparticles. *Journal of colloid and interface science* 2007, 315, (1), 116-22.

82. Saunders, B. R., On the Structure of Poly(N-isopropylacrylamide) Microgel Particles. *Langmuir* 2004, 20, (10), 3925-3932.

83. Batchelor, G. K.; Wen, C. S., Sedimentation in a dilute polydisperse system of interacting spheres. Part 2. Numerical results. *Journal of Fluid Mechanics* 1982, 124, 495-528.

84. Matsumoto, K.; Suganuma, A., Settling velocity of a permeable model floc. *Chemical Engineering Science* 1977, 32, (4), 445-7.

85. Neale, G.; Epstein, N.; Nader, W., Creeping flow relative to permeable spheres. *Chemical Engineering Science* 1973, 28, (10), 1865-74.

86. Neale, G. H.; Nader, W. K., Prediction of transport processes within porous media. Creeping flow relative to a fixed swarm of spherical particles. *AIChE Journal* 1974, 20, (3), 530-8.

87. Ooms, G.; Mijnlieff, P. F.; Beckers, H. L., Frictional force exerted by a flowing fluid on a permeable particle, with particular reference to polymer coils. *Journal of Chemical Physics* 1970, 53, (11), 4123-30.

88. Sutherland, D. N.; Tan, C. T., Sedimentation of a porous sphere. *Chemical Engineering Science* 1970, 25, (12), 1948-50.

89. Tambo, N.; Watanabe, Y., Physical characteristics of flocs. I. The floc density function and aluminum floc. *Water Research* 1979, 13, (5), 409-19.

90. Jang, S.-m.; Chen, Y.-h.; Yu, C.-h. Formation and planarization of shallow trench isolation in an integrated circuit. 1997. US Patent: 97810390.

91. Wu, R. M.; Lee, D. J., Hydrodynamic drag force exerted on a moving floc and its implication to free-settling tests. *Water Research* 1998, 32, (3), 760-768.

92. Wu, R. M.; Lee, D. J., Hydrodynamic drag on non-spherical floc and free-settling test. *Water Research* 2001, 35, (13), 3226-3234.

93. Gmachowski, L., Comment on "Hydrodynamic drag force exerted on a moving floc and its implication to free-settling tests" by R. M. Wu and D. J. Lee, Wat. Res., 32(3), 760-768 (1998). *Water Research* 1999, 33, (4), 1114-1115.

94. Coutinho, C. A.; Harrinauth, R. K.; Gupta, V. K., Settling characteristics of composites of PNIPAM microgels and TiO_2 nanoparticles. *Colloids and Surfaces, A: Physicochemical and Engineering Aspects* 2008, 318, (1-3), 111-121.

95. Pareek, V. K.; Cox, S. J.; Brungs, M. P.; Young, B.; Adesina, A. A., Computational fluid dynamic (CFD) simulation of a pilot-scale annular bubble column photocatalytic reactor. *Chemical Engineering Science* 2003, 58, (3-6), 859-865.

96. Tatsuma, T.; Tachibana, S. I.; Miwa, T.; Tryk, D. A.; Fujishima, A., Remote bleaching of methylene blue by UV-irradiated TiO_2 in the gas phase. *Journal of Physical Chemistry B* 1999, 103, (38), 8033-8035.

97. Sun, B.; Smirniotis, P. G., Interaction of anatase and rutile TiO_2 particles in aqueous photooxidation. *Catalysis Today* 2003, 88, (1-2), 49-59.

98. Wahi, R. K.; Yu, W. W.; Liu, Y.; Mejia, M. L.; Falkner, J. C.; Nolte, W.; Colvin, V. L., Photodegradation of Congo Red catalyzed by nanosized TiO_2. *Journal of Molecular Catalysis A: Chemical* 2005, 242, (1-2), 48-56.

99. Zhang, Z.; Wang, C. C.; Zakaria, R.; Ying, J. Y., Role of Particle Size in Nanocrystalline TiO_2-Based Photocatalysts. *Journal of Physical Chemistry B* 1998, 102, (52), 10871-10878.

100. Chen, L. C.; Chou, T. C., Kinetics of photodecolorization of methyl orange using titanium dioxide as catalyst. *Industrial & Engineering Chemistry Research* 1993, 32, (7), 1520-7.

101. Ishibashi, K. I.; Fujishima, A.; Watanabe, T.; Hashimoto, K., Detection of active oxidative species in TiO_2 photocatalysis using the fluorescence technique. *Electrochemistry Communications* 2000, 2, (3), 207-210.

102. Parida, K. M.; Sahu, N.; Biswal, N. R.; Naik, B.; Pradhan, A. C., Preparation, characterization, and photocatalytic activity of sulfate-modified titania for degradation of methyl orange under visible light. *Journal of colloid and interface science* 2008, 318, (2), 231-7.

103. Singh, H. K.; Saquib, M.; Haque, M. M.; Muneer, M., Heterogeneous photocatalyzed degradation of uracil and 5-bromouracil in aqueous suspensions of titanium dioxide. *Journal of Hazardous Materials* 2007, 142, (1-2), 425-430.

104. Yang, H.; Zhang, K.; Shi, R.; Li, X.; Dong, X.; Yu, Y., Sol-gel synthesis of TiO_2 nanoparticles and photocatalytic degradation of methyl orange in aqueous TiO_2 suspensions. *Journal of Alloys and Compounds* 2006, 413, 302-306.

105. Augugliaro, V.; Baiocchi, C.; Bianco Prevot, A.; Garcia-Lopez, E.; Loddo, V.; Malato, S.; Marci, G.; Palmisano, L.; Pazzi, M.; Pramauro, E., Azo-dyes photocatalytic degradation in aqueous suspension of TiO_2 under solar irradiation. *Chemosphere* 2002, 49, (10), 1223-1230.

106. Wang, Y., Solar photocatalytic degradation of eight commercial dyes in TiO_2 suspension. *Water Research* 2000, 34, (3), 990-994.

107. Bahnemann, D.; Bockelmann, D.; Goslich, R., Mechanistic studies of water detoxification in illuminated titania suspensions. *Solar Energy Materials* 1991, 24, (1-4), 564-83.

108. Janczyk, A.; Krakowska, E.; Stochel, G.; Macyk, W., Singlet Oxygen Photogeneration at Surface Modified Titanium Dioxide. *Journal of the American Chemical Society* 2006, 128, (49), 15574-15575.

109. Lu, M. C.; Roam, G. D.; Chen, J. N.; Huang, C. P., Adsorption characteristics of dichlorvos onto hydrous titanium dioxide surface. *Water Research* 1996, 30, (7), 1670-1676.

110. Yang, D.; Ni, X.; Chen, W.; Weng, Z., The observation of photo-Kolbe reaction as a novel pathway to initiate photocatalytic polymerization over oxide semiconductor nanoparticles. *Journal of Photochemistry and Photobiology, A: Chemistry* 2008, 195, 323-329.

111. Sarathy, S. R.; Mohseni, M., The Impact of UV/H2O2 Advanced Oxidation on Molecular Size Distribution of Chromophoric Natural Organic Matter. *Environmental Science & Technology* 2007, 41, (24), 8315-8320.

112. Comparelli, R.; Fanizza, E.; Curri, M. L.; Cozzoli, P. D.; Mascolo, G.; Passino, R.; Agostiano, A., Photocatalytic degradation of azo dyes by organic-capped anatase TiO_2 nanocrystals immobilized onto substrates. *Applied Catalysis, B: Environmental* 2005, 55, (2), 81-91.

113. Li, Y.; Li, X.; Li, J.; Yin, J., Photocatalytic degradation of methyl orange by TiO_2-coated activated carbon and kinetic study. *Water Research* 2006, 40, (6), 1119-1126.

114. Ruan, S.; Wu, F.; Zhang, T.; Gao, W.; Xu, B.; Zhao, M., Surface-state studies of TiO_2 nanoparticles and photocatalytic degradation of methyl orange in aqueous TiO_2 dispersions. *Materials Chemistry and Physics* 2001, 69, (1-3), 7-9.

115. Bianco Prevot, A.; Basso, A.; Baiocchi, C.; Pazzi, M.; Marci, G.; Augugliaro, V.; Palmisano, L.; Pramauro, E., Analytical control of photocatalytic treatments: degradation of a sulfonated azo dye. *Analytical and Bioanalytical Chemistry* 2004, 378, (1), 214-220.

116. Lee, H.; Machida, K.; Kuwae, A.; Harada, I., UV-excited resonance Raman spectra of methyl orange and its complex with cetyltrimethylammonium bromide. *Journal of Raman Spectroscopy* 1983, 14, (2), 126-9.

117. Wang, H.; Niu, J.; Long, X.; He, Y., Sonophotocatalytic degradation of methyl orange by nano-sized Ag/TiO_2 particles in aqueous solutions. *Ultrasonics Sonochemistry* 2008, 15, (4), 386-392.

118. Wang, K. H.; Hsieh, Y. H.; Chou, M. Y.; Chang, C. Y., Photocatalytic degradation of 2-chloro- and 2-nitrophenol by titanium dioxide suspensions in aqueous solution. *Applied Catalysis, B: Environmental* 1999, 21, (1), 1-8.

119. Bacsa, R. R.; Kiwi, J., Effect of rutile phase on the photocatalytic properties of nanocrystalline titania during the degradation of p-coumaric acid. *Applied Catalysis, B: Environmental* 1998, 16, (1), 19-29.

120. Gupta, V. K.; Jain, R.; Mittal, A.; Mathur, M.; Sikarwar, S., Photochemical degradation of the hazardous dye Safranin-T using TiO_2 catalyst. *Journal of colloid and interface science* 2007, 309, (2), 464-9.

121. Kansal, S. K.; Singh, M.; Sud, D., Studies on photodegradation of two commercial dyes in aqueous phase using different photocatalysts. *Journal of hazardous materials* 2007, 141, (3), 581-590.

122. Kurihara, M.; Matsuyama, H. Organic polymer-modified colloidal silica and its transparent antisoiling aqueous emulsion coatings. 2004. JP Patent 2004067740.

123. Zhu, F.; Zhang, J.; Yang, Z.; Guo, Y.; Li, H.; Zhang, Y., The dispersion study of TiO_2 nanoparticles surface modified through plasma polymerization. *Physica E: Low-Dimensional Systems & Nanostructures* 2005, 27, (4), 457-461.

124. Oliver, M. R., *Chemical Mechanical Planarization of Semiconductor Materials*. 2004.

125. Parker, J., Next-generation abrasive particles for CMP. *Solid State Technology* 2004, 47, (12), 30-32.

126. Steigerwald, J. M.; Murarka, S. P.; Gutmann, R. J., *Chemical Mechanical Planarization of Microelectronic Materials*. 1996.

127. Teo, T. Y.; Goh, W. L.; Lim, V. S. K.; Leong, L. S.; Tse, T. Y.; Chan, L., Characterization of scratches generated by a multiplaten copper chemical-mechanical polishing process. *Journal of Vacuum Science & Technology* 2004, 22, (1), 65-69.

128. Basim, G. B.; Brown, S. C.; Vakarelski, I. U.; Moudgil, B. M., Strategies for optimal chemical mechanical polishing (CMP) slurry design. *Journal of Dispersion Science and Technology* 2003, 24, (3 & 4), 499-515.

129. Chen, J.-C.; Lin, S.-R.; Tsai, W.-T., Effects of oxidizing agent and hydrodynamic condition on copper dissolution in chemical mechanical polishing electrolytes. *Applied Surface Science* 2004, 233, (1-4), 80-90.

130. Liang, H.; Kaufman, F.; Sevilla, R.; Anjur, S., Wear phenomena in chemical mechanical polishing. *Wear* 1997, 211, (2), 271-279.

131. Stavreva, Z.; Zeidler, D.; Ploetner, M.; Drescher, K., Characteristics in chemical-mechanical polishing of copper: comparison of polishing pads. *Applied Surface Science* 1997, 108, (1), 39-44.

132. Tsai, T.-H.; Yen, S.-C., Localized corrosion effects and modifications of acidic and alkaline slurries on copper chemical mechanical polishing. *Applied Surface Science* 2003, 210, (3-4), 190-205.

133. Kim, S. H.; Kwak, S.-Y.; Suzuki, T., Photocatalytic degradation of flexible PVC/TiO_2 nanohybrid as an eco-friendly alternative to the current waste landfill and dioxin-emitting incineration of post-use PVC. *Polymer* 2006, 47, (9), 3005-3016.

134. Liu, C.-W.; Dai, B.-T.; Yeh, C.-F., Post cleaning of chemical mechanical polishing process. *Applied Surface Science* 1996, 92, 176-9.

135. Tamboli, D.; Banerjee, G.; Waddell, M., Novel Interpretations of CMP Removal Rate Dependencies on Slurry Particle Size and Concentration. *Electrochemical and Solid-State Letters* 2004, 7, (10), F62-F65.

136. Balakumar, S.; Chen, X. T.; Chen, Y. W.; Selvaraj, T.; Lin, B. F.; Kumar, R.; Hara, T.; Fujimoto, M.; Shimura, Y., Peeling and delamination in Cu/SiLK process during Cu-CMP. *Thin Solid Films* 2004, 462-463, 161-167.

137. Borst, C. L.; Thakurta, D. G.; Gill, W. N.; Gutmann, R. J., Chemical mechanical polishing mechanisms of low-dielectric-constant polymers in copper slurries. *Journal of the Electrochemical Society* 1999, 146, (11), 4309-4315.

138. Convertine, A. J.; Ayres, N.; Scales, C. W.; Lowe, A. B.; McCormick, C. L., Facile, Controlled, Room-Temperature RAFT Polymerization of N-Isopropylacrylamide. *Biomacromolecules* 2004, 5, (4), 1177-1180.

139. Cheemalapati, K.; Chowdhury, A.; Duvvuru, V.; Lin, Y.; Tang, K.; Bian, G.; Yao, L.; Li, Y., Novel pure organic particles for copper CMP at low down force. *Materials Research Society Symposium Proceedings* 2004, 816, (Advances in Chemical-Mechanical Polishing), 41-47.

140. Jindal, A.; Hegde, S.; Babu, S. V., Chemical Mechanical Polishing Using Mixed Abrasive Slurries. *Electrochemical and Solid-State Letters* 2002, 5, (7), G48-G50.

141. Wrschka, P.; Hernandez, J.; Oehrlein, G. S.; Negrych, J. A.; Haag, G.; Rau, P.; Currie, J. E., Development of a slurry employing a unique silica abrasive for the CMP of Cu damascene structures. *Journal of the Electrochemical Society* 2001, 148, (6), G321-G325.

142. Choi, W.; Abiade, J.; Lee, S.-M.; Singh, R. K., Effects of Slurry Particles on Silicon Dioxide CMP. *Journal of the Electrochemical Society* 2004, 151, (8), G512-G522.

143. Park, Y. B.; Yoon, I. Y.; Ryu, H. H.; Lee, W. G., Pattern density and deposition profile effects on oxide chemical-mechanical polishing and chip-level modeling. *Journal of Electronic Materials* 2001, 30, (12), 1560-1568.

144. Towery, D.; Fury, M. A., Chemical mechanical polishing of polymer films. *Journal of Electronic Materials* 1998, 27, (10), 1088-1094.

145. Zantye, P. B.; Kumar, A.; Dallas, W.; Ostapenko, S.; Sikder, A. K., Investigation of the nonuniformities in polyurethane chemical mechanical planarization pads. *Journal of Vacuum Science & Technology, B: Microelectronics and Nanometer Structures--Processing, Measurement, and Phenomena* 2006, 24, (1), 25-33.

146. Katoh, T.; Kang, H.-G.; Paik, U.; Park, J.-G., Effects of abrasive morphology and surfactant concentration on polishing rate of ceria slurry. *Japanese Journal of Applied Physics, Part 1: Regular Papers, Short Notes & Review Papers* 2003, 42, (3), 1150-1153.

147. Lee, J. W.; Yoon, B. U.; Hah, S.; Moon, J. T., A planarization model in chemical mechanical polishing of silicon oxide using high selective CeO_2 slurry. *Materials Research Society Symposium Proceedings* 2001, 671.

148. Lee, S.-I.; Hwang, J.; Kim, H.; Jeong, H., Investigation of polishing characteristics of shallow trench isolation chemical mechanical planarization with different types of slurries. *Microelectronic Engineering* 2007, 84, (4), 626-630.

149. Park, J.-H.; Kanemoto, M.; Paik, U.; Park, J.-G., Nanotopography impact of surfactant concentration and molecular weight of nano-ceria slurry on remaining oxide thickness variation after shallow trench isolation chemical mechanical polishing. *Japanese Journal of Applied Physics, Part 1: Regular Papers, Brief Communications & Review Papers* 2007, 46, (8A), 5076-5079.

150. Tateyama, Y.; Hirano, T.; Ono, T.; Miyashita, N.; Yoda, T., Study on ceria-based slurry for STI planarization. *Proceedings - Electrochemical Society* 2001, 26, 297-305.

151. Kim, D.-H.; Kim, S.-K.; Kang, H.-G.; Park, J.-G.; Paik, U., The effect of cerium precursor agglomeration on the synthesis of ceria particles and its influence on shallow trench isolation chemical mechanical polishing performance. *Japanese Journal of Applied Physics, Part 1: Regular Papers, Brief Communications & Review Papers* 2005, 44, (12), 8422-8426.

152. Manivannan, R.; Ramanathan, S., Role of abrasives in high selectivity STI CMP slurries. *Microelectronic Engineering* 2008, 85, (8), 1748-1753.

153. Kiely, J. D.; Bonnell, D. A., Quantification of topographic structure by scanning probe microscopy. *Journal of Vacuum Science & Technology, B: Microelectronics and Nanometer Structures* 1997, 15, (4), 1483-1493.

154. Asahi, R.; Morikawa, T.; Ohwaki, T.; Aoki, K.; Taga, Y., Visible-light photocatalysis in nitrogen-doped titanium oxides. *Science* 2001, 293, (5528), 269-271.

155. Nambu, A.; Graciani, J.; Rodriguez, J. A.; Wu, Q.; Fujita, E.; Fdez Sanz, J., N doping of TiO_2(110): photoemission and density-functional studies. *Journal of Chemical Physics* 2006, 125, (9).

156. Batzill, M.; Morales, E. H.; Diebold, U., Influence of Nitrogen Doping on the Defect Formation and Surface Properties of TiO_2 Rutile and Anatase. *Physical Review Letters* 2006, 96, (2), 026103/1-026103/4.

157. Wu, P. G.; Ma, C. H.; Shang, J. K., Effects of nitrogen doping on optical properties of TiO_2 thin films. *Applied Physics A: Materials Science & Processing* 2005, 81, (7), 1411-1417.

158. Umebayashi, T.; Yamaki, T.; Itoh, H.; Asai, K., Analysis of electronic structures of 3d transition metal-doped TiO_2 based on band calculations. *Journal of Physics and Chemistry of Solids* 2002, 63, (10), 1909-1920.

159. Altynnikov, A. A.; Zenkovets, G. A.; Anufrienko, V. F., ESR study of reduced vanadium-titanium oxide catalysts. *Reaction Kinetics and Catalysis Letters* 1999, 67, (2), 273-279.

160. Coloma, F.; Marquez, F.; Rochester, C. H.; Anderson, J. A., Determination of the nature and reactivity of copper sites in Cu-TiO_2 catalysts. *Physical Chemistry Chemical Physics* 2000, 2, (22), 5320-5327.

161. Jagadale, T. C.; Takale, S. P.; Sonawane, R. S.; Joshi, H. M.; Patil, S. I.; Kale, B. B.; Ogale, S. B., N-Doped TiO_2 Nanoparticle Based Visible Light Photocatalyst by Modified Peroxide Sol-Gel Method. *Journal of Physical Chemistry C* 2008, 112, (37), 14595-14602.

162. Burda, C.; Lou, Y.; Chen, X.; Samia, A. C. S.; Stout, J.; Gole, J. L., Enhanced Nitrogen Doping in TiO_2 Nanoparticles. *Nano Letters* 2003, 3, (8), 1049-1051.

163. Gartner, M.; Osiceanu, P.; Anastasescu, M.; Stoica, T.; Stoica, T. F.; Trapalis, C.; Giannakopoulou, T.; Todorova, N.; Lagoyannis, A., Investigation on the nitrogen doping of multilayered, porous TiO_2 thin films. *Thin Solid Films* 2008, 516, (22), 8184-8189.

164. Wang, Z.; Li, Y.; Jiang, X.; Zhu, M.; Liao, R., Preparation and photocatalytic activity of nitrogen-doped titania with hexamethylenetetramine as nitrogen source. *Zhongguo Taoci* 2007, 43, (12), 59-61, 64.

165. Wu, J.-q.; Ding, B.-q.; Fang, D.-y., Nitrogen doping of nano-TiO_2 in fluidized bed. *Huadong Ligong Daxue Xuebao, Ziran Kexueban* 2005, 31, (5), 575-579.

166. Silveyra, R.; De La Torre Saenz, L.; Flores, W. A.; Martinez, V. C.; Elguezabal, A. A., Doping of TiO_2 with nitrogen to modify the interval of photocatalytic activation towards visible radiation. *Catalysis Today* 2005, 107-108, 602-605.

167. Shi, F. G.; Zhao, B., Modeling of chemical-mechanical polishing (CMP) with soft pads. *Applied Physics A: Materials Science & Processing* 1998, 67, (2), 249-252.

168. Wang, Y.; Zhao, Y.-W.; Gu, J., A new nonlinear-micro-contact model for single particle in the chemical-mechanical polishing with soft pad. *Journal of Materials Processing Technology* 2007, 183, (2-3), 374-379.

169. Castillo-Mejia, D.; Gold, S.; Burrows, V.; Beaudoin, S., The Effect of Interactions Between Water and Polishing Pads on Chemical Mechanical Polishing Removal Rates. *Journal of the Electrochemical Society* 2003, 150, (2), G76-G82.

ABOUT THE AUTHOR

Cecil Coutinho was born in Mumbai, India. He obtained his Bachelor's degree in Chemical Engineering at the University of Nebraska - Lincoln in May 2005. He began pursuing his Ph.D. degree in the Chemical Engineering Department at University of South Florida in August 2005. During the course of his study at USF, he presented his work in many conferences and published several papers. He was awarded the outstanding researcher award (2007-2008), and the outstanding teaching assistant award (2005-2006 and 2007-2008) by the Chemical & Biomedical Engineering department at USF. He was also presented with the outstanding graduate student achievement award in 2008 for excellence in research and teaching.